Tunable bandpass filters based on resonant optical tunneling

by

Timothy Ross Harrison

A thesis submitted in partial fulfillment of the requirements for the degree of

Master of Science

in

Photonics and Plasmas

Department of Electrical and Computer Engineering
University of Alberta

Abstract

This thesis describes the design, fabrication and characterization of tunable bandpass filter devices based on optical tunneling. The filters were manufactured from the hybrid assembly of first hemi-cylindrical and later hemi-spherical lenses, with a multi-layer thin-film stack deposited on the flat surface of each lens. The two lenses were then clamped in intimate contact and piezo stack actuators were fixed in place to drive a small air gap between the two coated faces. Manipulation of the angle of incident light and the width of the µm-scale air gap between the two thin film stacks serves to tune the center wavelength and shape of the optical passband transmitted through the device. The theory of operation for these devices was developed previously, but that theory is expanded upon in this thesis.

Depending on the desired operational range of the filter, different materials were used, with a NIR filter (range ~1000—1800 nm) fabricated using a-Si/SiO_2 multilayer stacks, and a VIS filter (range ~400—700 nm) fabricated with Ta_2O_5/SiO_2 films. Both filters were designed to produce flat-top passbands for TE-polarized light, with an approximately fixed fractional bandwidth ($\Delta\lambda/\lambda$ ~ 1 %). They also exhibit excellent orthogonal (TM) polarization and out-of-band rejection over the tuning range. For applications requiring a collimated tunable source, or in hyperspectral imaging, these filters could be an attractive alternative to current systems utilizing liquid crystal, acousto-optic, or grating based tunable filters.

Preface

Chapter 3 of this thesis was published as T.R. Harrison, G.J. Hornig, C. Huang, T. Haluza-DeLay, K. Scheuer, and R.G. DeCorby, “A widely tunable bandpass filter based on resonant optical tunneling,” Opt. Express **27**, 23633-23644 (2019). I was responsible for design of custom fabrication tools, device fabrication, experimental characterization, and manuscript preparation. I was assisted with fabrication, and manuscript revisions by G.J. Hornig. C. Huang was responsible for optical testing system design around the prototype filter and assisted in experimental characterization. L. Bu, and T. Haluza-DeLay were responsible for design of the tuning electronics and software of a prototype filter and K. Scheuer assisted in experimental characterization. R.G. DeCorby as the supervisory author, was responsible for concept and theoretical formation, device design, and assisted with manuscript composition.

Chapter 4 of this thesis has been submitted for publication in Applied Optics as, T.R. Harrison, K.G. Scheuer, and R.G. DeCorby, “Tunable bandpass imaging filter based on resonant tunneling through a ball lens assembly,” I was responsible for the design of all custom fabrication tools and non-optical assembly parts, as well as device fabrication, assembly, experimental characterization, ray tracing simulations, and manuscript preparation. I was assisted with experimental characterization and manuscript preparation by K. G. Scheuer. R. G. DeCorby was the supervisory author and was responsible for concept and theoretical formation, device design, and manuscript preparation.

Acknowledgements

First order acknowledgements and heartfelt thanks go out to my supervising professor, Dr. Ray DeCorby. Without whose advice and support, I would have had a much more difficult time completing this degree. You never failed to put things in perspective while reminding me that research can and often should be fun.

To the rest of the Integrated Optics lab, thank you for providing an engaging workplace filled with lively discussions. Special thanks to Graham Hornig for providing a sounding board whenever I was stuck on a problem and to Kyle Scheuer for his endless patience when I requested that he re-align the setup to take “just one more” set of filter passbands. I would also like to thank James Maldaner, Danny Pulikkaseril, Dr. Seyed Azmayesh-Fard, and Sanaa al-Sumaidae for helping me with my endless searches through the lab for the perfect part to fit my experiment and for providing additional knowledge in microfabrication techniques.

As much of my time was spent “downstairs” in the nanoFAB, I would like to thank all the nanoFAB staff for fostering a knowledgeable and approachable atmosphere. My endless questions may stop. Eventually. Specific thanks go to Dr. Aaron Hryciw for always being willing to entertain my process questions, and to Glenn Elaschuk for being my first point of contact whenever something on Doug went wrong.

Additionally, I would like to thank Dr. Trevor Allen at Stream Technologies Inc. for lending me spectrometers and the expertise of being one of the few others to work on a tunneling based filter.

To my family and friends, thank you for your constant encouragement, patience, and interest while I labored on this project. Particularly for building places where I could take my mind off my work and enjoy the company.

This research was funded by the Natural Sciences and Engineering Research Council (NSERC), Alberta Innovates Technology Futures (AITF), and the University of Alberta.

Table of Contents

List of Figures

List of Tables

List of Symbols and Abbreviations

Abbreviations

CW	Center wavelength
BW	Bandwidth
LC	Liquid-crystal
AO	Acousto-optic
VBG	Volume-Bragg grating
FP	Fabry-Perot
WDM	Wavelength division multiplexing
OD	Optical density
LVTF	Linear variable tunable filter
LCTF	Liquid crystal tunable filter
AOTF	Acousto-optic tunable filter
RF	Radio frequency
FWHM	Full-width half-maximum
DBR	Distributed Bragg reflector
QWS	Quarter-wave stack
PT	Potential transmittance
IT	Induced transmission
DMD	Dielectric-metal-dielectric
TIR	Total internal reflection
FTIR	Frustrated total internal reflection
NIR	Near infrared
BPF	Band pass filter
FOV	Field of view
SMF	Single mode fiber

Symbols

λ	Wavelength
θ_{IN}	Angle of incidence
n_{eff}	Effective index
T	Transmittance
d	Layer thickness
n	Refractive index

Δn	Refractive index contrast
Λ	Period of a periodic structure
$\vec{N}$	Surface normal vector
ω	Optical frequency
$\overrightarrow{K_g}$	Bragg grating vector
λ_B	Bragg wavelength
L	Length of a Fabry-Perot cavity
m	Mode order number
PT_{MAX}	Maximum potential transmittance
Y	Admittance
N	Complex refractive index
θ_C	Critical angle for total internal reflection
R	Reflectance
$\mathbf{k}$	Wavevector
k	Propagation wavenumber
β	Propagation wavenumber parallel to the boundary
c	Speed of light
t	Amplitude reflection coefficient
K	Bloch wavenumber
PT	Potential transmittance
κ	Extinction coefficient
δ	Phase thickness
η	Admittance
η_{eff}	Effective admittance
Z	Number of periods in a quarter-wave stack

Chapter 1 Introduction

1.1 Tunable optical bandpass filters

Tunable bandpass filters are a relatively recent branch of optical technology, but have recently seen adoption in a variety of fields including fiber communication [1], hyperspectral imaging [2], fluorescence microscopy [3], and radiometry/photometry [4]. In most cases, the choice of tunable filters over traditional fixed bandwidth filters is primarily driven by the desire to rapidly change the center wavelength of the passband of the filter. In the case of fixed filters, such functionality would require several filters to be used and then rotated in and out of the beam path, making for a complicated system. The use of a tunable filter can enable similar or better performance over the range of interest, while also allowing the system to be made more compact and economical. The advent of new tunable filter technologies has allowed the development of novel techniques in many of the fields listed above and should spur the adoption of such techniques in new fields. However, due to the multitude of applications with differing requirements, no filter technology has proven to be ideal in all cases.

This thesis builds upon previous work by the DeCorby group in the development of a thin-film optical filter based on resonant optical tunneling [5]. The purpose of this work was to produce a tunable version of that filter, which simulations had suggested might outperform many current technologies in terms of key specifications such as tuning range, out-of-band rejection, and polarization selectivity. To that end, the theory previously developed for the design of the static filter was expanded upon and used to design a tunable device, where tuning is afforded by simultaneous adjustments in the incident angle and the thickness of an air gap tunneling layer. Such a tunable tunneling filter was then fabricated through the deposition of thin film layers directly onto glass prisms and subsequent manual assembly. The angular tuning range of the device was then explored experimentally, and the tuning behavior and bandpass characteristics were shown to match very closely to simulation.

1.2 Tunable bandpass filter landscape

Tunable bandpass filters are devices which can, for application of a given input (applied voltage, acoustic signal, etc.), change their spectral transmission characteristics. For these filters, a variety of desirable specifications exist, with the importance of each varying by application. These can include: high out-of-band rejection, large blocking range, polarization insensitivity, insertion loss, selectable center wavelength (CW) and bandwidth (BW), input angle insensitivity (large field of view), large tunable range, “top-hat” (flat-top) bandpass shape, and rapid tuning time, amongst others [2]. The current landscape of tunable filters includes length-tuned fiber- or MEMS-based Fabry Perot filters [1], conventional angle-tuned thin-film filters [3,6–8], liquid-crystal (LC) [9] and acousto-optic (AO) [2] filters, as well as the angle-tuned volume-Bragg-grating (VBG) filter [4]. Most of these filters operate based on similar physics which will be discussed in Section 1.3, while the following will provide a summary of the relevant performance and typical applications of these various filters.

1.2.1 Length-tuned fiber and MEMS Fabry Perot filters

The operating principles of a basic Fabry-Perot (FP) are explained in Section 1.3.1. Essentially, two highly reflecting surfaces are held parallel to each other, forming a resonant cavity with some dielectric medium (often air) between the two reflectors. Only narrow bands of wavelength, depending on the length of the cavity and the cavity medium, are supported as cavity modes and thus subject to high transmission through the cavity. For length tuned filters (either fiber- or MEMS-based), tuning of the CW of the filter is accomplished through changing the physical spacing between the reflectors [1]. The materials and structure of tunable FP filters can include many of the static filter types discussed later in section 1.3, however those used in fiber communication are typically based on dielectric mirror coatings with an air gap between them, such as the fiber coupled filter shown in Figure 1.1(a) [10]. All FP filters produce a frequency-comb transmission spectrum. In wavelength division multiplexing (WDM) applications, the number of possible channels that can be selected for by a single filter is limited by the spacing between adjacent peaks in the comb (i.e. the free spectral range) and by the width of the transmission peak. This linewidth is determined by the finesse of the FP cavity, which itself is most often limited by the degree of mirror flatness, co-planarity between the mirrors, and material losses within the cavity [1].

With reflectance-limited cavities and dielectric reflectors that can be made to provide almost arbitrarily high reflectance, the potential for narrow bandwidth FP filters is quite high. Finesses > 100 allow fiber Fabry-Perot filters to be produced with bandwidths < 0.01 nm, and tuning ranges ~ 10-50 nm [1,11]. Insertion loss in these filters is often ~ 5 dB, while tuning speed is in the ms range. Unfortunately, the Lorentzian lineshape and high loss of these filters limits their application primarily to wavelength division multiplexing in fiber communications. MEMS-based Fabry-Perot filters have been widely studied [12–15]. A recent example is shown in Figure 1.1(c). Compared to the fiber-based devices mentioned above, this filter has much larger free spectral range (> 105 nm), a larger tuning range (> 94 nm), and transmission loss of ~ 5 dB [12].

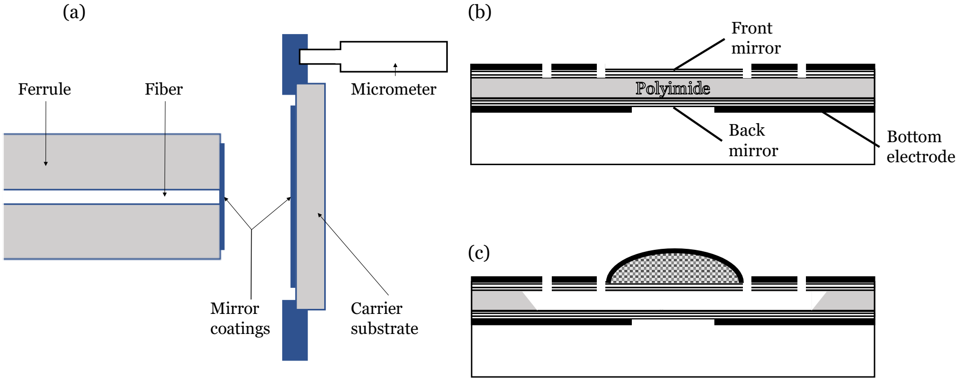

Figure 1.1. Examples of length-tuned Fabry Perot tunable filters. (a) Fiber facet FP for wavelength division multiplexing applications. Cavity actuation is done using a micrometer. Adapted from [10]. (b) Side view of a MEMS FP filter utilizing a sacrificial etch of polyimide to create an air-core cavity prior to etching and release. (c) The filter from part (b) after release. The cavity length is changed by an electrostatic voltage applied across the cavity. Adapted from [12].

1.2.2 Angle-tuned thin film filters

Angle tuned filters build upon the same FP cavity (or multiple-cavity) structure that is the basis for length-tuned filters. However, the adjustment of the phase length of the cavity is achieved by rotation rather than changing the mirror spacing. Fabrication is simplified, since the physical cavity length is fixed; both reflectors can be deposited as thin film stacks on opposite sides of a dielectric cavity medium or on the single side of a substrate with a cavity (or spacer) layer. The materials of the reflectors depend on the application, with metallic mirrors being suitable in certain wavelength ranges and dielectric reflectors used when metallic mirrors are too absorbing or when very high reflectances are required. Simple angle tuned filters exhibit shifts to shorter passband center wavelength when the angle of incidence is increased from 0° to larger angles (as measured from normal incidence) [16] as can be described by the equation:

$$\lambda(\theta_{IN}) = \lambda(0)\sqrt{1-\frac{\sin^2(\theta_{IN})}{n_{eff}^2}} \quad , \tag{1.1}$$

where θ_{IN} is the angle of incident light, λ is the transmission center wavelength, and n_{eff} is the effective index of the filter, which depends upon the filter structure and the polarization state of input light [17]. This polarization dependence results in polarization splitting of the passband with angle tuning and often limits the tuning ranges of these filters to about 2-2.5% of the designed center wavelength.

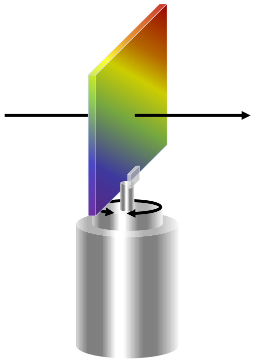

Figure 1.2. An angle tuned thin film filter such as the Semrock VersaChrome series filters. Adapted from [6].

Semrock has developed a proprietary angle-tuned thin film filter design that overcomes this polarization splitting and allows tuning ranges on the order of 12% of the normal incidence design wavelength [6]. Independent work has also produced a similar filter achieving 90 nm of tuning range from a design wavelength of 970 nm [8]. Such angle-tuned thin film filters rely upon making the change in center wavelength large for a small shift in input angle (i.e. small n_{eff} in Eq. 1.1), such that the available tuning range is maximized and so that tuning can be made as quickly as possible (~ 2.5 ms), overcoming the rotational inertia of the filter shown in Figure 1.2 [6,18]. Peak transmission of these filters is typically > 90% over the entire tuning range, and they exhibit a desirable "flat-top" passband shape, out of band rejection of optical density (OD) ~6, and very steep band edges (> OD6 at ± 10-30 nm). The application space for these angle-tuned thin film filters is fairly large, and includes fluorescence microscopy, imaging spectroscopy, and telecommunications [3,6].

1.2.3 Linear variable filters

Linear variable tunable filters (LVTFs) are an alternative design to angle-tuned filters in that they rely upon linear translation of the filter for wavelength tuning rather than angle tuning. These filters are still based upon Fabry-Perot or Fizeau interferometers [19] and are usually designed in a similar manner to the tunable FP filters mentioned above. For the case of a large area incident light beam, these behave as Fizeau interferometers. However, for a small area incident beam, these filters are effectively Fabry-Perot filters with a graded cavity thickness profile. In this regime, beam divergence requirements for these filters are dependent on the designed slope of the filter as well as on the spot size of the incident beam. A smaller beam waist results in less passband broadening as the cavity length seen by the beam varies less across the beam for a smaller spot size. However, the beam divergence is inversely proportional to the beam waist for a

Gaussian beam, resulting in additional broadening from a less-collimated input beam. Hence, the design of a complete filter system is necessarily a compromise between these two effects [20].

Wavelength tuning of linear filters is done translationally and is made possible by the graded cavity thickness profile mentioned above. However, such a graded profile is difficult to produce in thin films with standard semiconductor fabrication techniques. Through recent development of deposition masking [21], resist reflow [19,22,23], lateral deposition source offset [24], glancing angle deposition [25], and other techniques, linearly graded index profiles have been fabricated to such a degree that commercial LVTFs, such as those from Santec [26] and Delta Optical Thin Film [27] are readily available. Each of these techniques serves to produce a cavity where the mirrors are not plane parallel, but rather one mirror is set at an oblique angle relative to the other as shown in Figure 1.3.

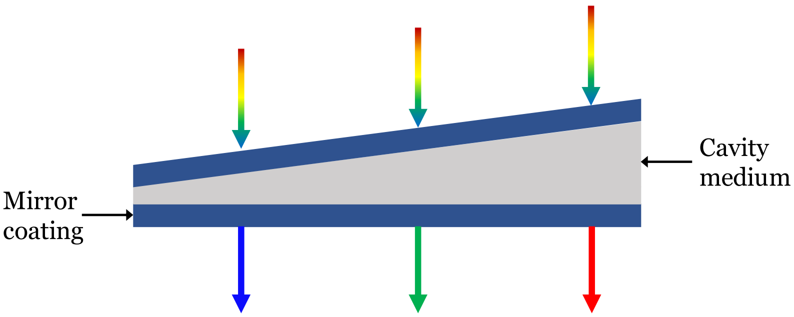

Figure 1.3. Schematic of a linear variable filter. Mirror layers can be either metal or dielectric, while the cavity medium may be air or a dielectric spacer layer. Scanning incident “white” light across the surface causes a variation in the wavelength of light passed through the filter. Adapted from [24].

In the case of a solid dielectric cavity layer, the cavity layer must be a graded film fabricated by a technique such as those mentioned above. However, through the use of wafer bonding, air cavity layers can be produced where one of the wafer halves has a film with a graded thickness profile that serves to provide an angled substrate for film deposition [19]. The cavity construction of these filters can be of the metal-dielectric type, an all-dielectric cavity, or even with the complex dielectric film stacks typical of angle-tuned filters. Any of these films can, in principle, be deposited to follow the graded profile of the cavity layer. Thus, similarly to the standard Fabry-Perot style filters, LVTFs with a variety of bandwidth, tuning range, center wavelength resolution, band shapes and insertion loss specifications can be designed depending on the application and complexity of the design. For example, for WDM applications in the telecom C- and L-bands, Santec offers an LVTF with a bandwidth as low as 0.25 nm (3 dB), tuning range from 1530-1610 nm, resolution of 0.01 nm, and insertion loss of 7.5 dB (type 03, structure S3) [26]. Alternatively, Delta Optical thin film offers an LVTF marketed for hyperspectral imaging with a bandwidth

(3dB) of ~2 % of the center wavelength (~10-20 nm), tuning range from 550-950 nm, user-dependent resolution, and insertion loss ~ 1 dB (LVNIRBP, LF102604 datasheet) [27]. Both filters offer very low polarization dependent losses (< 0.2 dB, Santec), and the Delta filter offers OD4 out of band rejection with a blocking range from 200-1200 nm. Of note, the Delta filter is sold only as the optical part, without any controlling electronics, whose details would determine minimum wavelength resolution and tuning speed.

As an estimate of the tuning rate for such a LVTF, consider a linear translational stage (Thorlabs PD1) with a maximum translational speed of 3 mm/s, and the 1.04 nm/mm positional rate of spectral shift for the filter fabricated in [25]. It follows that a reasonable tuning velocity for such a filter would be ~3 nm/s (i.e. tuning rate in the tens to hundreds of ms range for shifts of 1-2 nm). Alternatively, using the filter designed in [23], with a positional rate of spectral shift of ~30 nm/mm, a tuning velocity of 90 nm/s is reasonable. Both tuning rates are significantly slower than most other tunable filter technologies. Additionally, wavelength resolution and accuracy would be similarly determined by the choice of linear translation stage. Such slow tuning would appear to disqualify such linear filters from imaging spectroscopy applications, however LVTFs offer a unique technique to hyperspectral imaging since the whole filter can be simultaneously illuminated. This produces a linearly graded spectral profile on the face of the image sensor corresponding to the gradation of the cavity length of the filter. As a result, hyperspectral imaging can still be performed with LVTFs, especially on moving targets such as in microfluidics for fluorescence microscopy [28], or in line scanning applications [29].

1.2.4 Liquid-crystal filters

Several different liquid-crystal tunable filter (LCTF) designs exist including Šolc, and Fabry-Perot based designs. However, arguably the simplest and most commonly used are the Lyot-Öhman (birefringent) filters [2]. Such Lyot filters consist of an alternating stack of linear polarizers and tunable birefringent retarders based on liquid crystals as shown in Figure 1.4(a) and (b). The spectral transmission of each retarder stage (j) is a sinusoid in frequency space ($T_j = \cos^2(2^{j-2}\Gamma)$, with $\Gamma = 2\pi d\Delta n/\lambda$) [30] as shown in Figure 1.4(c), due to birefringent dispersion. Then, the net transmission of the filter is the product of the transmission of each retarder stage. Thus, when the filter is designed such that the thickness of each retarder stage are multiples of the first stage, the transmission lines are narrowed with each additional retarder, forming a more suitable passband for a tunable filter.

The ability to tune the filter comes from the change in retardation that occurs when voltage is applied to the liquid crystals. This applied voltage modifies the difference in refractive index between ordinary and extraordinary rays (Δn), which shifts the frequency of the sinusoid in each retarder and correspondingly shifts the location of the passband. The addition of subsequent elimination retarders between crossed polarizers as in [30], or the use of absorbing long-pass glass filters, allows the elimination of higher order peaks within the filter pass spectrum and can be used to increase the free-spectral range (blocking range) of the filter as shown in Figure 1.4(d).

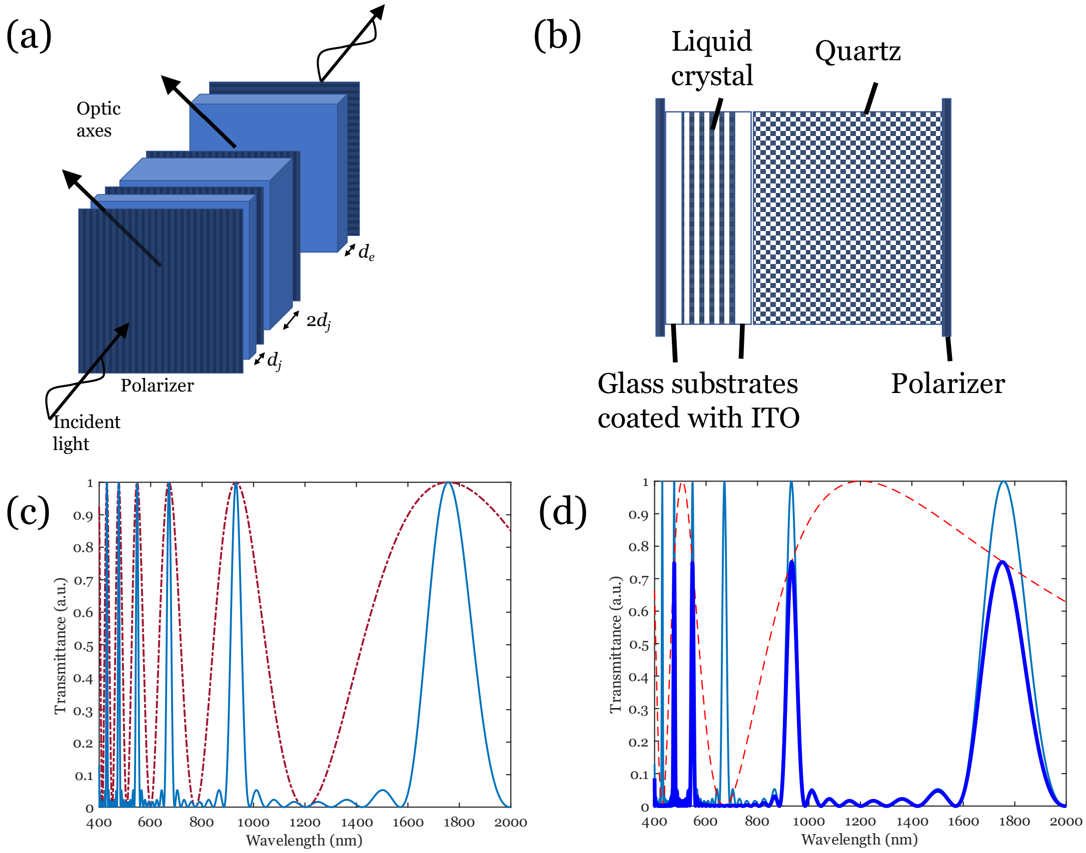

Figure 1.4. Characteristics of a liquid crystal Lyot filter, utilizing wavelength dependent birefringent retardation. (a) Basic schematic of the Lyot filter. Each birefringent retarder is some multiple of the thickness of the first retarder stage (d_j) and is placed between parallel linear polarizers. A final elimination retarder (d_e), with a polarizer oriented orthogonally, is used to eliminate sidebands of a designed order. (b) Side view of a typical retarder stage in a Lyot filter. (c) Spectral transmittance of a Lyot filter for one (dot-dashed line) or three (solid line) retarder stages. (d) Elimination of the third order peak with a retarder as in (a). The net transmission (bold line) is the product of the three retarder filter (solid line) and the elimination retarder (dashed) After [2,30].

LCTFs have become one of the mainstays within the tunable filter landscape due to their ease of fabrication, low drive power, compactness, and relatively high switching speed [30]. Such switching speed is determined by the type of LC used; nematic LCs allow filters to achieve tuning speeds in the tens of ms, while ferroelectric LCs can be switched in the tens of μs range [30–32]. Additional advantages inherent to LCTFs include a wide and continuous tuning range (several hundred nanometers), a large usable aperture, and a wide angular field of view (several degrees) [9]. However, LCTFs suffer from sub-optimal passband shape due to the passband being built from a discrete number of sinusoids, polarization dependent passbands, low transmission (< 50%) in the passband for polarized light, and poor out-of-band blocking (OD 3-4) [3].

1.2.5 Acousto-optic filters

Acousto-optic tunable filters (AOTFs) are based on radio frequency (RF) modulation of a birefringent crystal such as TeO_2 or Hg_2Cl_2. Depending on the type of crystal used, AOTFs can be designed as either "collinear" or "non-collinear" as shown in Figure 1.5. In these filters, collinearity refers to the propagation angle between the optical input and the RF acoustic wave that drives diffraction. When light is incident on these crystals in a noncollinear configuration, as in Figure 1.5(a), the birefringence splits the incoming beam into a fast and a slow mode, and the RF modulation diffracts both fast and slow modes to different exit angles [33]. Selection of the orthogonally polarized first-order diffracted beams (+ and – beams) is a function of the system design, with the angle between the two beams usually on the order of several degrees. Due to the extended bulk nature of the diffraction medium and the fact that the diffraction pattern is moving with the RF modulation, the acousto-optic medium only diffracts a specific wavelength range (i.e. a passband) at the designed angle [2]. The filter can then be tuned, since the frequency of RF modulation determines the wavelength of light that is diffracted past the beam-stop. Collinear AOTFs are often made using a different acousto-optic crystal than the non-collinear case, using crystals such as quartz, or $LiNbO_3$. In a collinear arrangement, the incident light, diffracted light, and the RF modulation all travel along the same axis as shown in Figure 1.5(b). Hence, as the input beam and the diffracted beam produced are orthogonally polarized, the diffracted beam must be extracted from the input beam by a polarizer [2,34].

The typical tuning range of AOTFs can be several hundred nanometers, while bandwidths can be as narrow as 1 nm full-width half-maximum (FWHM), and transmission efficiencies as high as 98%. However, this transmission is split between the (+) and (-) polarized beams, resulting in < 50 % transmission for unpolarized input light. AOTFs have very fast wavelength switching speeds (6-30 μs), but have additional drawbacks in that they are typically expensive, have small usable apertures and have poor out of band blocking (OD 3-4) [3,35].

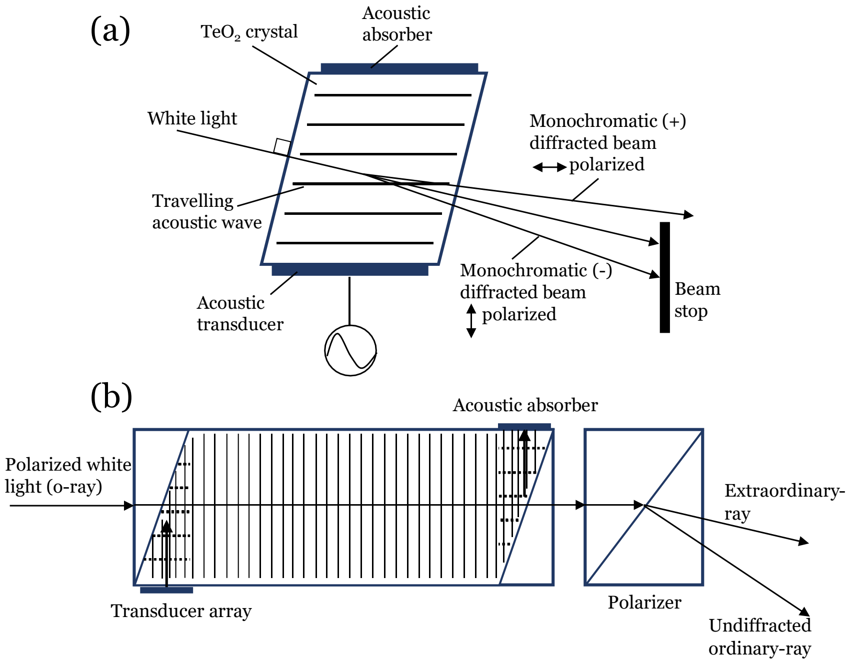

Figure 1.5. Schematics of typical acousto-optic filters. (a) Operation of a noncollinear acousto-optic tunable filter. (b) Collinear acousto-optic tunable filter. Transmitted light must be separated using an analyzing polarizer. Adapted from [2,36].

Acousto-optic and liquid-crystal tunable filters offer very similar performance parameters, for the most part, and have been at the forefront of applications in hyperspectral imaging and imaging spectroscopy. Such adoption has been supported by the ability to construct such filters that operate in almost any wavelength range, are continuously tunable over a wide range, have large acceptance angles, no moving parts, and tune quickly [2,37]. The choice between AOTFs and LCTFs comes down to concerns about switching speed in the case of LCTFs and the expense of fabrication of AOTFs; particularly in the long-wave infrared, where materials such as Tl_3AsSe_3 must be cryogenically cooled to operate acousto-optically [2]. Nevertheless, both of these technologies have been employed in a number of spectroscopic applications including laser induced breakdown spectroscopy, fluorescence spectroscopy, and Raman spectroscopy [37,38]. Additional application spaces for AOTFs and LCTFs have included WDM [11,31,39,40], tunable semiconductor lasers [41], and interrogation of fiber Bragg grating sensors [42,43].

1.2.6 Volume-Bragg-grating filters

Volume Bragg grating tunable filters are a relatively recent addition to the tunable filter landscape. They are based upon thick (several mm) holographic gratings written in a photo-thermo-reactive glass [44–46]. Such glass is imprinted with a periodic refractive index profile, producing a Bragg diffraction grating. The large path length over which this periodic index profile can be written overcomes inherent index contrast limitations, where changes in index are usually only $\Delta n_g \sim 10^{-4}$. VBGs typically follow the schematic shown in Figure 1.6, where Λ is the period of the Bragg grating, $\vec{N}$ is the vector normal to the entrance surface, θ_{in} is the angle between incident light and $\vec{N}$, and φ is the angle between $\vec{N}$ and the grating vector $\overrightarrow{K_g}$. For incoming collimated light at angle θ_{in}, the wavelength of light that is diffracted will meet the Bragg condition of the grating, which is (for the transmission grating shown in Figure 1.6) [46]:

$$\lambda_B = 2n_0\Lambda\sin\theta_{in} \quad . \tag{1.2}$$

Here, n_0 is the refractive index of the grating material. Thus, the wavelength of diffracted light can be tuned by adjustment of the angle of incident light onto the grating. Any beam that enters the grating that does not meet the diffraction condition will pass through undisturbed.

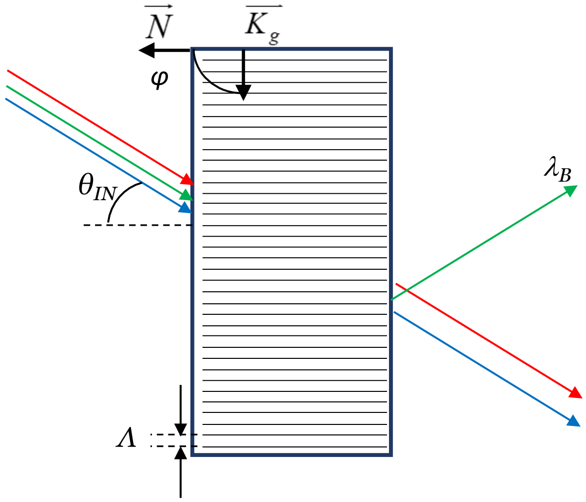

Figure 1.6. Schematic of the operation of a volume Bragg transmission grating. Adapted from [46].

This grating technology forms the basis for a line of tunable filters produced by Photon Etc. Inc., utilizing paired reflection gratings [45]. Quoted performance for these filters includes transmission efficiency ~ 60% (including collimation losses), polarization insensitivity, bandwidths from 0.15-5 nm, tuning ranges as large as from 1000-2300 nm (although requiring multiple VBGs [47]), < OD6 out of band rejection at ± 40 nm for a visible range filter (at ± 80 nm for a SWIR filter), > OD6 for the entire tunable range (i.e. ~1000 nm blocking range), and stabilization times >35 ms for a center wavelength step size of 0.1 nm [46,48]. The major caveat when it comes to VBG filters is that the collimation requirements of input beams are very high (divergence < 1 mrad). This would appear to limit the usefulness of such filters to fiber coupled or highly collimated free-space applications such as WDM [49], laser line filters [48], or as the tunable element in a broadly tunable laser source (when used in conjunction with supercontinuum sources) [4]. However, recent work with software compensation has allowed the expansion of VBG filters into the imaging spectroscopy space [50].

1.2.7 Tunable filter summary

In general, no one filter technology is suitable for all applications. However, for specific applications, through combinations of the figures of merit shown in Table 1.1, certain filter types are more advantageous than others.

Table 1.1 Relative performance metrics of tunable filters

Filter technology	Bandwidth (nm)	Tuning range (nm)	Insertion loss (dB)	Out-of-band rejection	Angular acceptance (mrad)	Flat-top Passband shape	Polarization dependence
Length-tuned [1,11,51]	< 0.01	1530-1610	<5	>OD6	Fiber coupled	No	None
Angle-tuned [6,8,52,53]	10-20	880-970	<0.5	OD6	>45	Yes	Low
LVTF [19,25–27,29]	0.25-20	550-1000	1-7.5	OD4	45-785	Yes	Low
AOTF [6,34,37,54]	2-50	560-1120	4	OD3	>80	No	High
LCTF [6,30,37]	10-100	500-900	>8	OD3-4	>100	No	High
VBG [46,48]	1.0–2.5	400-1000	<2	OD6	<1	Yes	Low

1.3 Bandpass optical filters

Many of the tunable filter technologies above are based upon the bandpass filter principles described below.

1.3.1 Single-cavity filters

Traditional optical bandpass filters are essentially the classical FP etalon shown in Figure 1.7, but manufactured on the thin-film scale and operating at or near normal incidence. Some dielectric spacer layer (cavity) is placed between reflectors M_1 and M_2, which are typically either metal mirrors or dielectric distributed Bragg reflectors (DBRs). DBRs are typically constructed from "quarter-wave stacks" (QWS) of alternating high and low refractive index materials. Assuming 'hard-mirror' boundary conditions (i.e. no penetration of the mode fields into the mirrors, which is never exactly true), the cavity transmission resonances occur at wavelengths which are half-wave multiples of the cavity length, L (i.e. $L = (m\lambda/2)$, for $m = 1, 2, 3, \ldots$). The resulting spectral transmission is governed by an Airy function depending on the mirror reflectances as shown in Figure 1.7(c), producing a "frequency comb". Such transmission spectra can then be easily adopted as the basis for a bandpass filter.

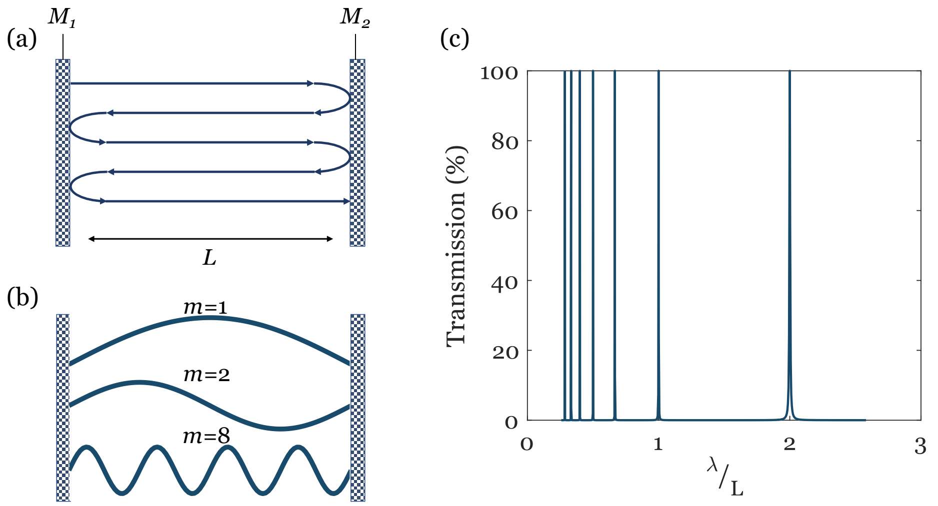

Figure 1.7. Schematic representation of a Fabry-Perot resonator and its properties. (a) Light is trapped between the reflectors M_1 and M_2, causing self-interference. (b) Only frequencies that form standing waves can exist as modes within the cavity. The number of half-wavelengths in the standing wave pattern is denoted by the mode order m. (c) Characteristic transmission peaks that occur when the standing wave condition $L = (m\lambda/2)$, as in part (b), is satisfied. The lowest order ($m = 1$) mode occurs for $(l/L) = 2$. The next 6 lowest mode order transmission resonances are also shown. Adapted from [55].

The use of a cavity made from thin films deposited directly on a polished substrate allows the creation of high-finesse FP resonators that have narrow bandwidths and can be operated in lower mode orders compared to macroscopic FP etalons. This is primarily due to the inherent planarity of thin films deposition methods that follow the contour of the substrate without exhibiting much thickness variation. However, as the surface roughness of thin films generally increases with film thickness, FP filters operating above the 3rd mode order tend to exhibit increased scattering losses, and passband broadening [17]. Additionally, when operated above the 2nd mode order, these filters produce longwave and shortwave sidebands as the result of the lower- and higher-order modes of the FP cavity, and the removal of these sidebands becomes necessary for the operation of the filter. In the case of short wavelength sidebands, this can be done simply using absorbing glass filters. To eliminate longwave sidebands, the filter can either be designed to operate in the first mode order, or in the higher order cavity case, these longwave sidebands can sometimes be neglected entirely. In order to neglect these sidebands, the sensitivity range of the apparatus or detector used must be considered. Otherwise, additional FP filters can be cascaded to eliminate the longwave sidebands.

The design of these filters is well known. Center wavelengths can be chosen based upon the FP resonance condition, while the choice of mode order and mirror reflectance can be used to adjust the finesse and hence the bandwidth of the cavity. Unfortunately, the passbands associated with these FP filters are Lorentzian. Thus, the wider the passband desired, the poorer the out of band blocking near to the passband will be. Fabrication errors can also result in passbands with center wavelengths slightly shifted relative to the design wavelength. Such errors can be ameliorated by slightly tuning the angle of incidence, in order to change the phase length of the cavity and shift the resonant wavelength of the filter. However, this can only be used to shift the center wavelength over a narrow range as large angle shifts broaden the filter passband and reduce peak transmittance.

A variety of different physical cavity geometries exist: MEMS filters with an air-gap cavity [1], thin film stacks with a thin film cavity layer [17], mirrors deposited on the ends of two closely aligned fibers [56,57], and solid etalon filters deposited on polished substrates [58,59]. Filters based on a thin-film cavity medium often have lower finesse due to scattering losses within the cavity layer, a problem that is less apparent in solid-etalon or MEMS air-gap filters [17]. Additionally, in order to accommodate the low free spectral range in high finesse filters, often lower order thin film cavity filters, with larger free spectral range, are placed in series with the designed filter to eliminate sidebands [17].

1.3.2 Multiple-cavity filters

As mentioned previously, the Lorentzian lineshape of the passband of the single-cavity FP filters is an undesirable line shape. This is because near to half of the energy transmitted through the passband lies outside the half-width of the filter. A more rectangular passband (sometimes referred to as “flat-top” or “top-hat”) would be ideal because such a shape has more uniform transmittance across all wavelengths in the passband and steeper out of band rejection. One of the simplest ways to produce a more rectangular passband from a FP filter design is by cascading a series of optical cavities such that they are “coupled” in a manner similar to electronic circuit filters. These coupled multiple cavity filters couple modes between adjacent cavities which serves to reduce the ripple in the passband and increases the out-of-band rejection of the net filter.

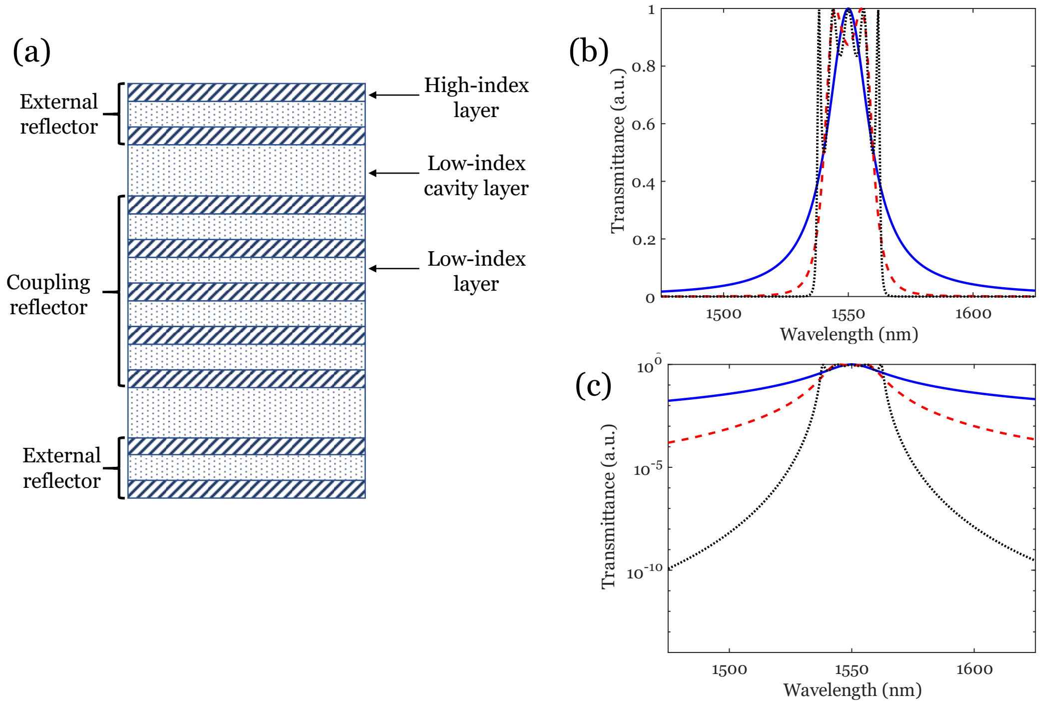

Figure 1.8. (a) Schematic of a two-cavity filter clad by QWS dielectric Bragg reflectors. The central coupling reflector allows the cavity modes to interact. (b), (c) Transmission of multiple cavity dielectric filters made from QWS of a-Si/SiO2 centered at 1550 nm following the structure shown in (a). The blue (solid), red (dashed), and black (dotted) lines correspond to 1, 2, and 5 cavity filter structures respectively.

As shown in Figure 1.8 (a), the basic multiple cavity filter is a series of FP type filters with some coupling reflector (usually a series of dielectric quarter-wave layers) between. This coupling reflector splits the cavity modes, with the degree of splitting inversely proportional to the magnitude of the transmission coefficient of the central reflector (i.e. a higher reflectance produces less splitting) [60]. Thus, the net transmission of the filter can be built from the superposition of the split cavity modes. The addition of further cavities through coupling reflectors can create a passband with steeper edges and a more uniform transmission as shown in Figure 1.8(b),(c). The structure of the coupling and external reflectors hence becomes a complex design problem based on balancing passband ripple with out of band rejection and passband edge steepness. Detailed design procedures for such design have been described elsewhere [17,60,61].

1.3.3 Induced transmission filters

Some standard Fabry-Perot type filters as discussed above essentially use metal layers as high reflectance mirrors. However, the absorbing nature of metallic films limits the region of applicability of such filters and inhibits the practicality of implementing multiple cavity filters [17]. The design of metal-dielectric filters can, however, be simplified using the potential transmittance (PT) concept. In particular, for the case of a series of thin metal layers, by appropriately spacing them with surrounding dielectric films, the maximum transmittance of the assembly can be designed to be significantly greater (within some passband for which the assembly is 'admittance-matched') than would be suggested by the bulk absorption coefficient of the metal [62]. The process of "inducing transmission" [63] is achieved by designing the admittances of the dielectric media surrounding the metallic layers such that, from the perspective of the metallic layer, the reflectance seen at both input and exit interfaces is effectively zero [64]. This is typically achieved using a QWS and a "phase-matching layer" as shown in Figure 1.9(a). This produces a transmittance $T = PT_{MAX}$, where PT_{MAX} is the so-called 'maximum potential transmittance' and is analogous to admittance matching an absorbing film to ambient media. For a single absorbing (e.g. metal) layer, PT_{MAX} is determined entirely by its thickness and its complex refractive index at a given wavelength.

For multilayers containing multiple metal layers (as in Figure 1.9(b)), the total PT is merely the product of the PT of the individual metal layers [65]. Bandpass filters that are based on admittance matching of this type are often termed induced transmission (IT) filters and can be designed from a series of dielectric-metal-dielectric (DMD) periods [66] to produce multiple cavity metal-dielectric filters. With the addition of each subsequent metal layer, the PT decreases as shown in Figure 1.9(c),(d), while the out of band rejection correspondingly increases. As IT filters produce only a single passband, unlike the mode orders of FP filters, IT filters have a wide out-of-band rejection range and are often used as sideband suppression filters for narrowband FP filters [67]. Additionally, the passband shape seen in Figure 1.9(c), with a longwave "hump" is typical of IT filters and is difficult to customize.

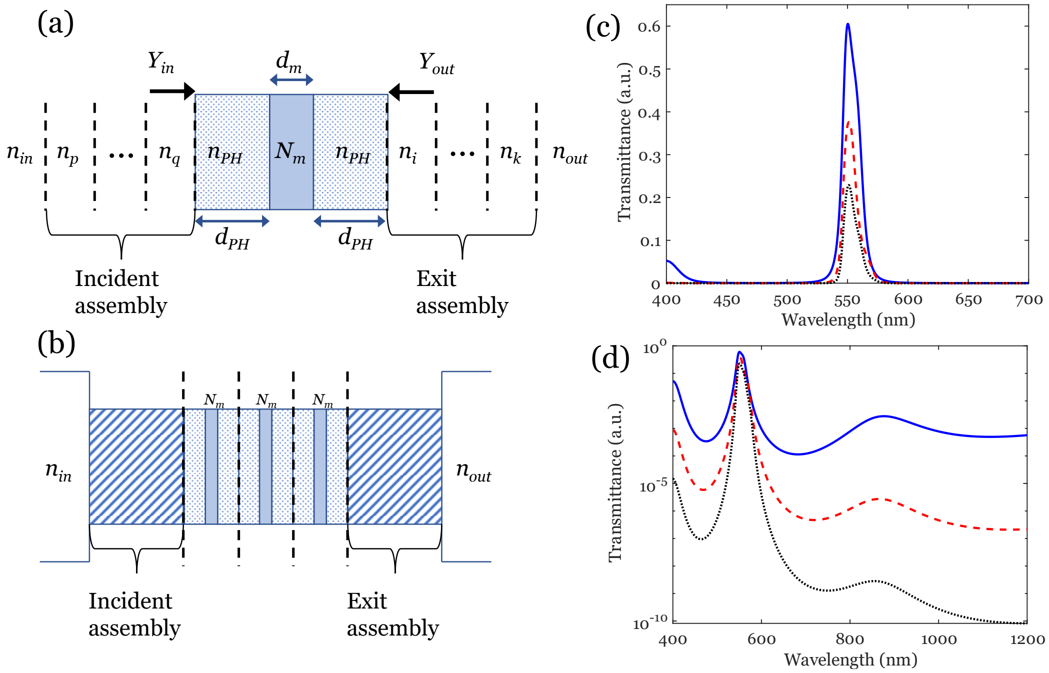

Figure 1.9. (a) Schematic of an induced transmission filter. The admittance seen at the metal layer N_m is transformed to a real value by the "phase-matching" layers (n_{PH}, d_{PH}) on either side. This real admittance is then matched to the entrance and exit media by an assembly of dielectric films (typically a QWS). (b) A multiple metal layer IT filter. The same dielectric-metal-dielectric period used in the single layer IT filter can be cascaded to improve out-of-band rejection at the cost of transmittance. Adapted from [62,66]. (c),(d) Simulated transmission (including dispersion) of the IT filter described in Figures 8.36 and 8.41 of [17], for 1, 2, and 3 DMD periods corresponding to blue (solid), red (dashed), and black (dotted) lines respectively.

1.3.4 Resonant tunneling filters

Particularly relevant for this thesis is the consideration of resonant optical tunneling filters, which have been known for decades, with early results summarized by Baumeister [68] more than 50 years ago. These filters are based on dielectric tunneling layers operating at angles greater than the critical angle ($\theta_{in} > \theta_C$), where total internal reflection (TIR) would typically occur. However, for a sufficiently thin tunneling layer, the evanescent field within the tunneling layer can couple to propagating modes in the surrounding medium. This allows for transmission through the disallowed region, similar to quantum mechanical tunneling. Such transmission only occurs for a narrow range of wavelengths as shown in Figure 1.10(c) and can thus be used as the basis of a bandpass filter. These dielectric tunneling layers act analogously to lossless metal layers and thus any filter structure that can be designed for a metal-dielectric filter can be adapted to a tunneling filter. This includes the Fabry-Perot style tunneling filter shown in Figure 1.10(a) and (b) [68]. In order to achieve TIR at the interfaces with the tunneling layers, the addition of high index coupling prisms, such as shown in Figure 1.10(b), is required.

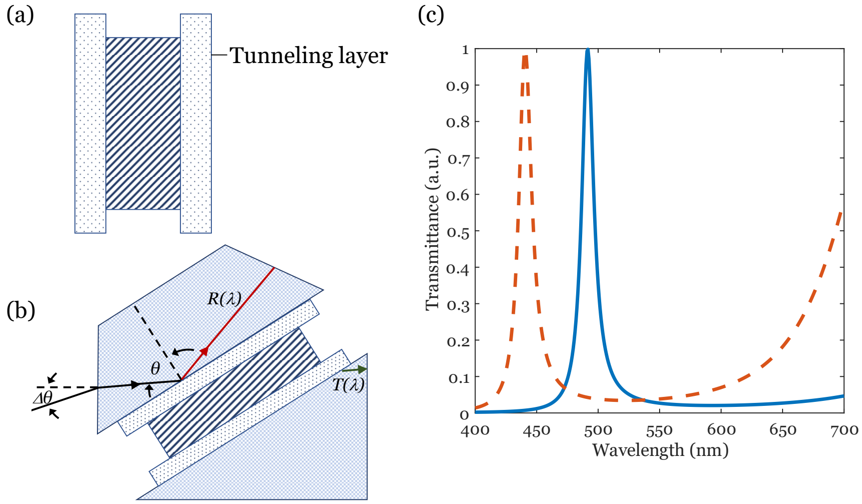

Figure 1.10. Fabry-Perot tunneling filter. (a) Basic layer structure: tunneling layers (dotted) are separated by a higher index dielectric spacer layer (shaded). Each tunneling layer acts as a single FTIR mirror. (b) Schematic of the tunneling filter in operation. The filter structure is bracketed by high-index coupling prisms such that the internal angle of incidence (θ) exceeds the critical angle in the prism. (c) Simulated transmission characteristics of a single-cavity FP tunneling filter in the FTIR regime. The TE- (blue solid line), and TM- (orange dashed line) transmittance are plotted at $\theta = 60°$. Here the tunneling layers are low index dielectrics, with index $n_T = 1.38$ and thickness $d_T = 180$ nm, while the spacer layer is a higher index dielectric with $n_S = 2.3$, and thickness $d_S = 309.5$ nm. Input and exit prisms are dielectrics of index $n_{in} = 1.72$. Adapted from [68].

Original development of the FP type tunneling filter, also known as the frustrated total internal reflection filter (FTIR), promised a narrowband filter with high peak transmittance. Unfortunately, due to scattering losses and residual absorption in multilayer coatings, the early tunneling filters only exhibited peak transmittance on the order of 15% [69]. Additionally, due to different phase changes upon reflection at the TIR interfaces for different polarization states, the phase-length of the cavity in these FP style tunneling filters is polarization dependent. Thus, the passbands for *s*- and *p*-polarizations (TE- and TM- respectively) occur at different wavelengths as shown in Figure 1.10(c). This polarization splitting occurs for almost every tunneling filter type, and, combined with large shifts in passband wavelength for relatively small shifts in input angle, led Baumeister to conclude that, “It is doubtful if the single tunnel layer will ever be produced as a practical bandpass filter” [68]. An additional issue with such conventional tunneling filters comes from the use of solid tunneling layers (particularly in multiple tunnel layer filters), where the relatively high refractive index of tunnel layers such as KBr ($n = 1.463$) or cryolite ($n = 1.33$) necessitates the use of very high index coupling prisms such as CdTe ($n = 2.91$) or Irtran-6 ($n = 2.67$) [68,70,71]. This allows filters to use reasonable coupling angles, or else larger, lower index, substrates are required to accommodate larger θ_C. Such high index prisms are often highly absorbing, further compounding issues of high insertion loss typical of these filters.

1.4 Breakdown of the organization of the thesis

This thesis explains the design, fabrication, and optical testing of several iterations of a tunable optical bandpass filter based on resonant optical tunneling through an air tunneling layer. These devices are an extension of previously published work by the DeCorby group, where admittance-matching principles were used to design a static bandpass filter based on an air gap tunneling layer [5]. In this thesis, the theory behind this admittance-matched optical tunneling was expanded from the prior work. Moreover, a strategy for wide-range tuning of the bandpass filter was studied, where the tuning mechanism is simultaneous adjustment of the incident angle and the air-gap thickness. Initially, this principle was applied to the design and implementation of a device with passband tuning over the ~1000-1700 nm wavelength range. However, this concept is not limited to operation in the near-infrared (NIR) region and can be generalized to operate in any wavelength range provided suitable materials are available. In the final stages of the project, a visible-range filter was produced, and a tunable range ~ 460-750 nm in wavelength was verified.

Chapter 2 details the theory of filters utilizing resonant optical tunneling. Included is a discussion of frustrated total internal reflection, resonant optical tunneling, and the design procedure to produce a resonant tunneling bandpass filter utilizing admittance-matching. These filters are designed with an air gap tunneling layer, such that coupling prisms made from common optical glasses can be used. The discussion in Chapter 2 is limited to static bandpass filters.

The theory, design, and testing of a tunable bandpass filter operating in the NIR is explained in Chapter 3. Air-gap tuning through piezo actuation was used to adjust passband shape, while a rotational stage provided angle tuning of the center wavelength of the passband. This first device was fabricated by depositing the necessary thin film stacks directly onto the face of hemicylindrical coupling prisms to minimize beam deviation with angle tuning. Performance of the assembled device is discussed as well as potential improvements in out-of-band rejection and blocking range through increased layer count in the multilayer film stack.

The next iteration of the tunable filter is described in Chapter 4. The choice was made to use hemispherical coupling prisms to simplify and improve optical coupling, while the design was expanded to include a version of the filter that operates in the visible range. The use of spherical prisms necessitated the design and machining of a jig to hold and actuate the two hemispheres of the filter. The design files for this jig are included in Appendix A. Included in this chapter is the implementation of a relay lens system such that the spherical filter could be used as a hyperspectral imager. Finally, Chapter 5 serves to summarize the thesis and outlines future avenues of related research.

Chapter 2 Theory

2.1 Introduction

This chapter discusses background knowledge and theory relevant to the design of the optical filters discussed in later chapters. First, basic optical tunneling theory is discussed, followed by a summary of a few historical resonant tunneling examples. Finally, theory illustrating the design procedure for an air gap resonant tunneling bandpass filter is described [5].

2.2 Frustrated total internal reflection

In principle, TIR provides the basis for an ideal broadband mirror. Furthermore, the ability to 'frustrate' TIR allows for the design of many functional optical components, including optical modulators, beam splitters, and filters [68]. The typical tunneling scenario is as shown in Figure 2.1, where a plane wave ($\mathbf{k}_i$) is incident from the high index medium **A** onto the interface with medium **B**, which is embedded within the high index material. When light is incident on the interface at angles $\theta_{IN} > \theta_C$ (where $\theta_C = \sin^{-1}(n_2/n_1)$ is the critical angle for TIR), the electric field in medium **B** is entirely evanescent, and the incident beam is entirely reflected provided the layer **B** is sufficiently thick. However, when the thickness d of layer **B** is sufficiently small, the evanescent field extends to the high index exit medium and excites plane wave propagation ($\mathbf{k}_t$) there. This excitation of a transmitted wave in medium **C** is often called attenuated total reflection or FTIR [55].

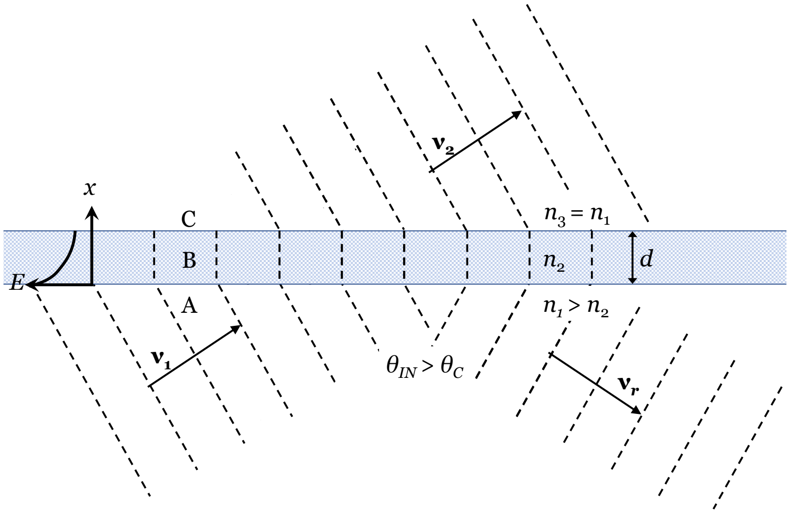

Figure 2.1. Typical optical tunneling scenario. The electric field decays evanescently in medium B due to TIR at the interface AB. However, when layer B is sufficiently thin, the electric field can extend through the layer and excites a propagating mode (i.e. plane wave) in medium C.

The transmission (for small values of *d*) through the TIR barrier layer can be found from analysis of the Fresnel coefficients. Taking the x-axis as the axis normal to the layer interfaces, the propagation wavenumber along this axis within the lossless high index medium is defined for arbitrary input angle as:

$$k_{1x} = \sqrt{\left(\frac{n_1 \omega}{c}\right)^2 - \beta^2} \equiv p \quad , \tag{2.1}$$

where ω is the optical frequency, while $\beta = n_1 k_0 \sin\theta$ is the propagation wavenumber along the direction parallel to the boundaries (z-axis), with k_0 the free-space wavenumber. For $\theta_{IN} > \theta_C$, the wave within the low index medium is purely evanescent and so the propagation wave number k_{2x} is purely imaginary [16]:

$$k_{2x} = -i\frac{2\pi}{\lambda}\sqrt{n_1^2 \sin^2\theta_1 - n_2^2} \equiv iq \quad , \tag{2.2}$$

and the transmittance (*T*) through the low index layer becomes [16]:

$$T \sim \left|t_{12}t_{23}\right|^2 e^{-2qd} \quad , \tag{2.3}$$

where, t_{12}, and t_{23} are the Fresnel transmission coefficients from medium 1 to medium 2 and from medium 2 to medium 3 respectively (n_1=n_3). Thus, the transmittance through the low-index layer becomes negligible for thickness $d >> 2\lambda$. This behavior allows a formal equivalence to be drawn between the behavior of a dielectric tunneling barrier and an ideal metal film [68], as both structures support purely evanescent waves and have transmission characteristics that decay with film thickness.

2.3 Resonant tunneling

Similar to a Fabry-Perot cavity clad by metallic mirrors, resonant tunneling conditions can be designed for a cavity consisting of two tunneling barriers separated by a single high index layer as depicted in Figure 2.2. The transmission through the two-barrier layer structure (T_2) can be treated simply with transfer matrices [16]:

$$\begin{aligned} T_2 = \left|t_2\right|^2 &= \frac{1}{1+4\left|C\right|^2\cos^2\left(K\Lambda\right)} \quad , \\ \cos\left(K\Lambda\right) &= \frac{1}{2}\left(A+D\right) \quad , \end{aligned} \tag{2.4}$$

where *A*, *C*, *D* are the components of the unit cell transfer matrix of the two period, periodic medium. Referring to the figure, note that the unit cell comprises one ‘barrier layer’ with index n_2

and thickness b followed by one 'tunneling layer' with index n_1 and thickness a. These transfer matrix components will be different for the TE and TM cases, with the TE case yielding [16]:

$$\cos(K\Lambda) = \cos(pa)\cosh(qb) - \frac{1}{2}\left(\frac{p}{q} - \frac{q}{p}\right)\sin(pa)\sinh(qb) \quad , \tag{2.5}$$

where a is the thickness of the central high index layer, b is the thickness of the barrier layers, while q and p are defined as above. Λ is the period $(a = \Lambda - b)$ of the unit cell, and K is the Bloch wave number of the periodic structure. Resonant tunneling will occur when $\cos(K\Lambda) = 0$, which only occurs for specific thicknesses of the central high-index layer (i.e. at a given λ).

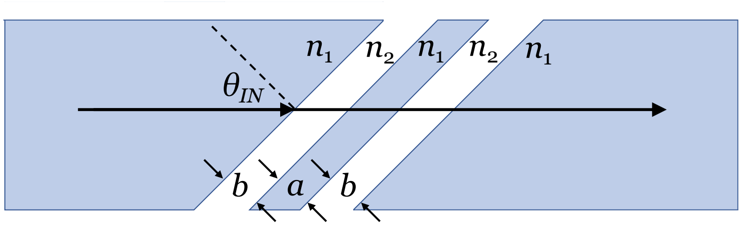

Figure 2.2. Schematic of a double barrier layer tunneling structure. Each barrier layer, of index n_2 and thickness b, is embedded in a higher index material n_1. The central cavity layer, of thickness a, between the two FTIR reflectors, acts analogously to the Fabry-Perot etalon. Adapted from [16].

This layered structure is directly analogous to a Fabry-Perot etalon. The barrier layers act as high reflectance mirrors, while the central high-index layer acts as the cavity medium. Thus, resonant tunneling will occur when the central spacer layer is ~$m\lambda/2$. Unlike the ideal Fabry-Perot, there is a finite phase shift upon reflection from each tunneling barrier, which results in the discrepancy from the ideal resonant condition. Such analysis can be generalized to N barrier layers, such that the transmittance for N barrier layers becomes [16]:

$$T_N = |t_N|^2 = \frac{1}{1 + |C|^2 \cdot \left\{\frac{\sin(NK\Lambda)}{\sin(K\Lambda)}\right\}^2} \quad , \tag{2.6}$$

with peak transmittance ($T_N = 1$) at:

$$\frac{\sin(NK\Lambda)}{\sin(K\Lambda)} = 0 \quad . \tag{2.7}$$

Resonant tunneling through a double barrier structure is directly associated with coupling to the quasi-guided (leaky) waveguide modes supported by the central high-index layer n_1. Such coupling occurs when the thickness a (from Figure 2.2) results in the bounce angle of a guided mode that matches the input angle θ_{IN}. Thus, energy is evanescently coupled through the input barrier to build up in the core, then is coupled evanescently to the output medium. In fact, resonant tunneling through any layered medium is associated with the excitation of in-plane guided modes, which can be TIR modes, non-normal incidence Fabry-Perot modes, surface-plasmon modes, etc. Periodic metal-dielectric structures can also exhibit resonant transmission characteristics under these conditions. Such structures are essentially a series of coupled Fabry-Perot cavities which can produce (N-1) – fold splitting of the resonant frequencies for the N-period system [72]. This can result in a reasonably wide band of high transparency and serves as the basis for many metal-dielectric filter structures [17].

2.4 Induced transmission filters

As mentioned in Section 1.3.3, a commonly used design methodology to produce metal dielectric bandpass filters relies upon the maximization of the potential transmittance at a particular wavelength and for a given thickness of metal. Filters designed in this way are referred to as induced transmission (IT) filters. The potential transmittance (PT) as defined by Macleod [17], is "the ratio of the irradiance leaving the rear surface to that actually entering at the front surface," i.e. the maximum transmittance that could be achieved neglecting reflectance at the front surface. For an assembly of layers including a metal layer with fixed parameters, the potential transmittance of the metal layer is then determined purely by the admittance of the structure at the exit face of the metal layer [63]. The admittance that produces a maximum potential transmittance can be found and a film stack to produce that admittance can be designed at the exit surface. Then an additional admittance matching coating at the front surface of the metal layer can be constructed to eliminate any input reflectance, producing a filter structure with the maximum potential transmittance (PT_{MAX}) at the design wavelength.

2.4.1 Potential transmittance and exit impedance

For the design of a filter with a single absorbing layer as shown in Figure 2.3, the potential transmittance of the filter at normal incidence can be shown to be [17]:

$$PT = \left[\begin{array}{l} \dfrac{\left(n^2-\kappa^2-2n\kappa Z/X\right)}{\left(n^2+\kappa^2\right)}\left(\sin^2\alpha\cosh^2\beta+\cos^2\alpha\sinh^2\beta\right) \\ +\left(\cos^2\alpha\cosh^2\beta+\sin^2\alpha\sinh^2\beta\right) \\ +\left(1/X\right)\left(n\sinh\beta\cosh\beta+\kappa\cos\alpha\sin\alpha\right) \\ +\dfrac{X^2+Z^2}{X\left(n^2+\kappa^2\right)}\left(n\sinh\beta\cosh\beta-\kappa\cos\alpha\sin\alpha\right) \end{array}\right]^{-1} . \qquad 2.8$$

Here:

$$\begin{aligned}\delta &= 2\pi\left(n-i\kappa\right)d_m / \lambda = \left(2\pi n d_m\right)/\lambda - i\left(2\pi\kappa d_m\right)/\lambda \\ &= \alpha - i\beta \\ \alpha &= \left(2\pi n d_m\right)/\lambda \\ \beta &= \left(2\pi\kappa d_m\right)/\lambda \quad ,\end{aligned}$$

and $Y_e = X + iZ$, is the exit admittance as 'seen' by the metal layer (i.e. looking towards the right in Figure 2.3(a)). Note that admittance is expressed in so-called 'free-space' units [17] here (i.e. as the medium admittance divided by the admittance of free space). For normal incidence onto a non-magnetic bulk medium, such as assumed for the entrance and exit media, the admittance in free-space units is then numerically equivalent to the refractive index. $N_m = n - i\kappa$ is the complex refractive index of the metal layer, d_m is the thickness of the metal layer, and λ is the wavelength of interest. Then, Equation 2.8 can be used to find the exit admittance $Y_{op} = X_{op} + iZ_{op}$ that produces $PT = PT_{MAX}$:

$$X_{op} = \left[\begin{array}{l}\dfrac{\left(n^2+\kappa^2\right)\left(n\sinh\beta\cosh\beta+\kappa\sin\alpha\cos\alpha\right)}{\left(n\sinh\beta\cosh\beta-\kappa\sin\alpha\cos\alpha\right)} \\ -\dfrac{n^2\kappa^2\left(\sin^2\alpha\cosh^2\beta+\cos^2\alpha\sinh^2\beta\right)^2}{\left(n^2\sinh\beta\cosh\beta-\sin\alpha\cos\alpha\right)^2}\end{array}\right]^{\frac{1}{2}} , \qquad 2.9$$

$$Z_{op} = \frac{n\kappa\left(\sin^2\alpha\cosh^2\beta+\cos^2\alpha\sinh^2\beta\right)}{\left(n\sinh\beta\cosh\beta-\sin\alpha\cos\alpha\right)} . \qquad 2.10$$

Adaptation of the above equations for off-normal incidence has been performed by Allen, *et al.* [62], however only the normal incidence case will be considered here.

Using the values of the exit admittance calculated from Equations 2.9 and 2.10 in Equation 2.8, the maximum PT can be determined for a given thickness of metal. In general, the thinner the metal layer, the higher the value of PT_{MAX}. Additionally, for increasing metal thicknesses, Y_{op} approaches the complex conjugate of the admittance of the bulk metal at a given wavelength [62]. Therefore, for a given design constraint on the minimum acceptable passband transmittance, a hard limit is placed on the thickness of metal that can be incorporated in the filter.

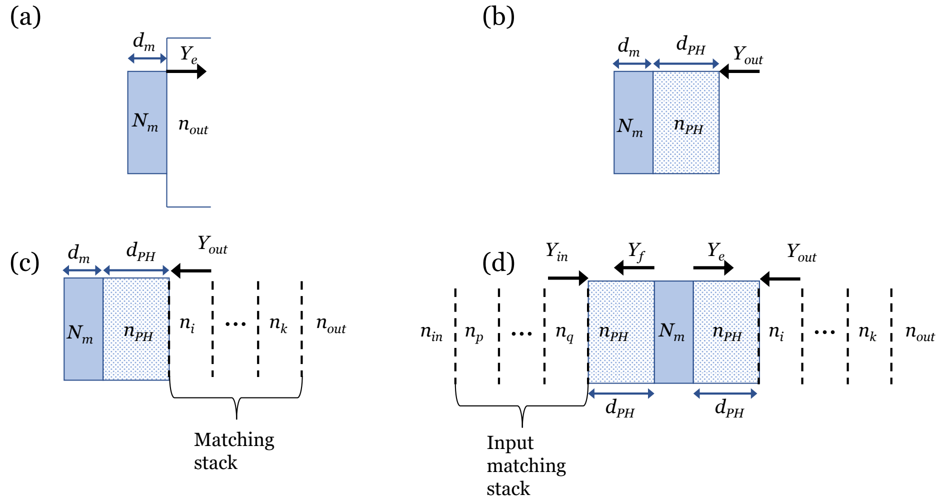

Figure 2.3. Procedural design of an induced transmission filter. (a) For a known metal layer N_m, d_m, the required backside admittance $Y_e = Y_{op}$ to produce maximum potential transmittance at a given wavelength can be calculated analytically. (b) Looking at the metal layer from the substrate, the conjugate of the admittance seen at the backside of the metal layer (Y_{op}*) is transformed by a phase matching layer of index n_{PH} and phase thickness δ_{PH} to give a real backside admittance Y_{out}. (c) A dielectric QWS is used to match this backside admittance to the substrate admittance n_{out}. (d) The procedure used in previous parts is repeated looking at the frontside admittance seen by the metal layer (Y_f, Y_f*), transforming it to the real admittance Y_{in}, and finally matching it to an input medium n_{in}.

2.4.2 Design of the dielectric matching stack

The next step in the design of the induced transmission filter is simplified through admittance matching. The maximum potential transmittance of the filter (i.e. $PT = PT_{MAX}$) will occur when $Y_e = Y_{op}$, where Y_{op} is the admittance found from the solution of Equations 2.9, and 2.10. Furthermore, the maximum transmission, $T = PT_{MAX}$ will occur when the admittance seen by the front side of the metal layer looking toward the input (Y_f) is equal to the optimal admittance, $Y_f = Y_e = Y_{op}$ which will guide the design of the input matching stack [62]. The problem becomes one of designing a stack of films terminating with the substrate ($n_{out} - i\kappa_{out}$) to produce Y_{op}. Often, the substrate is a material with low loss, i.e., $\kappa_{out} = 0$, thus, considering the reverse problem is more straightforward [17].

In this case, looking from the substrate towards the metal layer, the complex conjugate of the substrate index ($n_{out} + i\kappa_{out}$) is the first layer in a stack of films that must produce $Y_{op}{}^* = X_{op} - iZ_{op}$. To produce this admittance, matching can be done by first adding a “phase-matching” layer of sufficient thickness to transform the complex admittance $Y_{op}{}^*$ to a real value, then by the construction of a quarter-wave stack to match the substrate admittance. As in Macleod, to convert a complex admittance $Y_{op}^* = X_{op} - iZ_{op}$ to a purely real value, a film of phase thickness δ_{PH} for index n_{PH} can be used, where [17]:

$$\delta_{PH} = \frac{1}{4\pi}\arctan\left[\frac{2Z_{op}n_{PH}}{\left(n_{PH}^2 - X_{op}^2 - Z_{op}^2\right)}\right] \quad . \tag{2.11}$$

The resulting real admittance after this phase matching layer is:

$$Y_{out} = \frac{2X_{op}n_{PH}^2}{\left(X_{op}^2 + Z_{op}^2 + n_{PH}^2\right) + \left[\left(X_{op}^2 + Z_{op}^2 + n_{PH}^2\right)^2 - 4X_{op}^2 n_{PH}^2\right]^{1/2}} \quad . \tag{2.12}$$

Y_{out} will, in general, be less than the substrate admittance regardless of whether the phase matching layer is of high or low index [17]. A quarter wave layer of index n_1 will transform an initial admittance Y_I to Y_1 as [67]:

$$Y_1 = \frac{n_1^2}{Y_I} \quad . \tag{2.13}$$

Each following quarter wave layer (n_i, for i = 2, 3, ...) will similarly transform the new admittance Y_1 such that the new admittance after each layer (Y_i) becomes:

$$Y_2 = \left(\frac{n_2}{n_1}\right)^2 Y_I \,; Y_3 = \left(\frac{n_1 n_3}{n_2}\right)^2 \frac{1}{Y_I};.... \tag{2.14}$$

Thus, as $Y_{out} < n_{out}$ and $n_{out} > 1$, the quarter wave matching stack should be designed starting with a quarter wave layer of low index such that Y_{out} can be increased to match n_{out}. The design of the dielectric stack on the input side proceeds identically, only requiring that the order of the structure be reversed and the frontside impedance at the metal layer $Y_f = Y_e$ be matched to the input medium.

One advantage of this design technique is that multiple metal layer filters can be designed using the same methodology. The use of phase-matching layers serves to transform the complex admittance seen by the metal layers to real values, and hence the metal layers with surrounding phase-matching layers can be simply cascaded as DMD periods with real admittances [62,64,73]. The only modification from the above design philosophy is that the dielectric matching stacks are added only to admittance match to input and exit media, not between each DMD period. As mentioned in Section 1.3.3, additional metal layers serve to improve out-of-band rejection and the rate at which the band edge decays, but do so at the expense of PT_{MAX} [66].

2.5 Design of an air gap tunneling filter

The FP tunneling structure shown in Figure 1.10(b), is representative of a typical tunneling filter that relies upon solid barrier layers such as SiO_2 or MgF_2 to add support for a high-index central cavity layer. Thus, in order to achieve TIR (and tunneling) at the interfaces with these barrier layers, high index coupling prisms are required. These high index prisms are typically made of non-standard optical glasses or more exotic materials depending on the design wavelength [68]. As the range of angles required for TIR filter operation increases with the index of the tunneling layers, solid tunneling layers necessitate large substrates to accommodate these incident angles (in some cases, $\theta_C > 60°$). Such large substrates often produce increased scattering losses and spatial convolution effects resulting from non-uniformities in the deposition of thin films over large areas.

If, instead of using a FP tunneling structure, a single tunneling layer filter is designed, using air as the tunneling layer, many of these difficulties can be overcome [74]. Standard optical glasses can be used as coupling prisms, and the range of angles required for TIR operation are no longer as extreme ($\theta_C \sim 45°$). As mentioned above, this air-gap tunneling layer essentially behaves as a lossless metal layer and the design procedures developed for IT filters can be adapted as in the DeCorby group's previous work [5,68,75]. The result is an all-dielectric band pass filter (BPF) with a polarization dependent passband, but with strong suppression of the orthogonal polarization. The structure is as shown in Figure 2.4. Operation of the filter consists of resonant tunneling occurring through excitation of surface states supported at the interfaces between the air gap and the dielectric matching stacks [76–78].

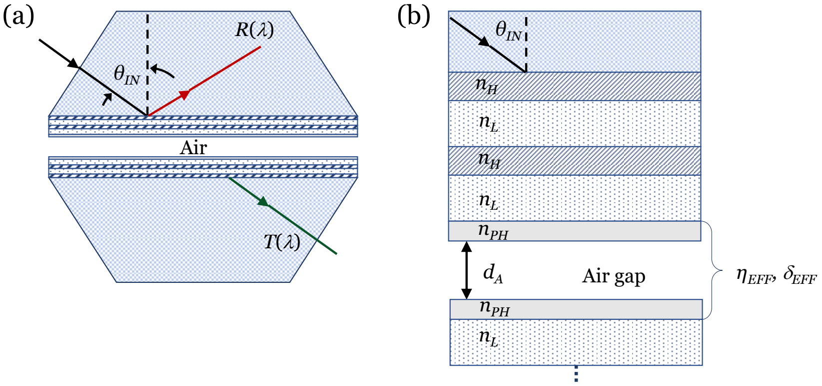

Figure 2.4 (a) A schematic diagram of an air gap tunneling filter. Nominally symmetric thin film stacks bracket an air gap. (b) The thin film structure of the filter centered around the air gap, where n_L and n_H are the refractive indices of the high- and low- index films respectively, $n_{PH} = n_L$ or n_H, and is the index of the phase-matching layer, and d_A is the thickness of the air gap. The air gap and the phase matching layers can be combined and represented by an effective layer with admittance η_{EFF} and phase thickness δ_{EFF}. Adapted from [5].

As described by Melnyk *et al.* [5], the concept of tilted admittance can be used to analyze the tunneling structure. Assuming lossless materials at off-normal incidence and TE polarization, the tilted admittance of layer j can be expressed as $n_j\cos\theta_j$; n_j is the refractive index of the layer and $\theta_j = \sin^{-1}[(n_{IN}/n_j)\sin\theta_{IN}]$ is the propagation angle in the given layer found from Snell's law (n_{IN} and θ_{IN} are the index and propagation angle in the coupling prism). Additionally, the phase thickness of the layer can be defined as $\delta_j = (2\pi/\lambda)n_j d_j \cos\theta_j$, where λ is the free-space wavelength and d_j is the physical thickness of the layer. Using these simplifications and the principle of equivalent layers [66], the three central layers of Figure 2.4(b) can be represented by an equivalent layer with effective phase thickness δ_{EFF} and effective admittance η_{EFF} given by [75]:

$$\eta_{EFF} = \eta_{PH} \times \left\{ \frac{\sin 2\delta_{PH}\cosh\mu_A - \frac{1}{2}Y_M\cos 2\delta_{PH}\sinh\mu_A - \frac{1}{2}Y_P\sinh\mu_A}{\sin 2\delta_{PH}\cosh\mu_A - \frac{1}{2}Y_M\cos 2\delta_{PH}\sinh\mu_A + \frac{1}{2}Y_P\sinh\mu_A} \right\}^{1/2} . \qquad 2.15$$

Here, $Y_M = (\kappa_A/\eta_{PH} - \eta_{PH}/\kappa_A)$ and $Y_P = (\kappa_A/\eta_{PH} + \eta_{PH}/\kappa_A)$, while $\eta_A = i\kappa_A$ and $\delta_A = i\mu_A$ are the imaginary admittance and phase thickness of the air layer. Finally, η_{PH} and δ_{PH} are the real admittance and phase-thickness of the phase-matching layers, respectively. Similar to the IT filter, η_{EFF} must be real [75] for transmission through the filter. Thus, the imaginary admittance of the air layer must be transformed through suitable thickness of the phase-matching layers at a desired wavelength. This thickness, for a given λ, θ_{IN}, η_{IN}, and η_{PH}, can be expressed as $d_{PH} = \delta_{PH}\lambda/(2\pi n_{PH}\cos\theta_{PH})$, where $\delta_{PH} = (\pi - \xi)/2$ and [66]:

$$\xi = \tan^{-1}\left\{ \frac{2\eta_{PH}\eta_A(\cosh 2\mu_A - 1)}{(\eta_A^2 - \eta_{PH}^2)\sinh 2\mu_A + \eta_A(\eta_A^2 + \eta_{PH}^2)(4\pi \cdot d_A \cdot C_A / \lambda)} \right\}. \qquad 2.16$$

Here, $C_A = \cos^2\theta_A$ or 1 for TM- and TE-polarized light respectively, and the tangent is evaluated in the first or second quadrant.

Thus, with suitable design of the phase-matching layers, the effective index (and hence the admittance) becomes suitably matched for only one polarization state, and a narrow range of wavelengths [5]. This results in a strong suppression of all other polarization states, and a narrow passband with steep band edges. The remaining layers in the matching stack shown in Figure 2.4(b) serve to match the input impedance to the transformed η_{EFF} of the three central layers and provide additional out-of-band suppression.

Chapter 3 Widely tunable bandpass filter based on resonant optical tunneling

This chapter was published as T. R. Harrison, G. J. Hornig, C. Huang, L. Bu, T. Haluza-Delay, K. Scheuer, and R. G. DeCorby, "Widely tunable bandpass filter based on resonant optical tunneling," Opt. Express **27**(16), 23633-23644 (2019), https://doi.org/10.1364/OE.27.023633.

3.1 Introduction

This section describes the theory and construction of a tunable bandpass filter based on frustrated total internal reflection through an air layer. A constructed filter based on a 4-layer a-Si/SiO_2 matching stack is demonstrated operating in the NIR region. The filter passband is tunable from 1200—1800 nm, with a fixed fractional bandwidth ~ 1%, and out-of-band rejection ~ OD6. Simulations indicate that a similar filter with better assembly could be tunable from 1000—1800 nm. This chapter was published in Optics Express [79].

3.2 Background

Tunable bandpass filters are used in fiber communication [1], hyperspectral imaging[2], fluorescence microscopy [3], and radiometry/photometry [4] systems. Desirable properties include fast tuning over a wide range, high angular acceptance (wide field of view), large clear aperture, flat-top passband shape [2], high transmission in the passband, variable pass bandwidth, high out-of-band rejection [2,3], and wide blocking range. While no single technology has been able to satisfy all of these requirements, their relative importance is of course application-dependent. For example, some imaging systems require filters with high angular acceptance and aperture, but often with relaxed specifications on pass-band characteristics. Conversely, many non-imaging applications of tunable filters can be addressed by commercially available fiber-coupled instruments (see for example [80]).

Length-tuned fiber- or MEMS-based Fabry-Perot filters [1] and conventional angle-tuned thin-film filters can provide narrow to moderate tuning range [3,6–8]. When a wider range is required, liquid-crystal (LC) [9] and acousto-optic (AO) [2] filters are commonly employed. Both can provide tuning over several hundred nanometers in wavelength and can accommodate high angular field of view (several degrees), but they suffer from sub-optimal pass-band shape, relatively high loss (< 50 % transmission in the passband for polarized light), and poor out-of-band blocking [3]. An alternative approach is the angle-tuned volume-Bragg-grating (VBG) filter [4], which can operate over several hundred nanometers in wavelength and provides high out-of-band blocking. The VBG filter has limited angular acceptance (~ 1 mrad), and thus has often been used in combination with a fiber-coupled, broadband supercontinuum laser source. However, it is worth noting that, through appropriate software correction to compensate angular shift of the passband, VBG filters can also be used for imaging spectroscopy [50].

While attracting theoretical interest, tunneling-based bandpass filters have historically been viewed as technologically impractical [68]. The reasons for this include their extreme angular sensitivity and polarization dependence, typically high insertion loss, and need for high-index coupling prisms and high incident angles when traditional solid tunneling layers are employed [68]. We recently demonstrated [5] a tunneling filter that addresses several of these shortcomings, in part by employing an air gap tunneling layer. Notably, we showed that, with the use of high-index-contrast admittance-matching stacks, the filter can simultaneously act as a broadband polarizer, eliminating the problem of polarization-dependent pass-bands associated with traditional tunneling filters. Furthermore, the air gap tunneling layer allows the use of standard glass or fused silica coupling prisms and operation at relatively convenient incident angles near 45 degrees. While the angular sensitivity of the pass-band is still very high (~ 40-50 nm/degree), it can result in an angular acceptance comparable to that of the commercial VBG filters (~ 0.5 mrad). Moreover, for applications that can accommodate such a restriction, high angular sensitivity confers potential for broadband and rapid tuning through the use of mechanical rotational stages. Here, we describe a strategy that combines angle tuning with piezo-based tuning of the air gap tunneling layer thickness. This enables the position of a flat-top pass-band, with fractional bandwidth $\Delta\lambda/\lambda$ ~ 1 %, to be varied over an extremely broad range (~ 1000 – 1800 nm wavelength), using a single optical prism assembly. Both a detailed theoretical treatment and an experimental verification are provided.

3.3 Admittance-matched tunneling—theory

As shown in Figure 3.1, a representative structure comprises an air gap symmetrically bounded by thin-film-stack-coated prisms, with light incident at an angle subject to total internal reflection (TIR) at the air interfaces. Consider the central 3 layers comprising the air gap and the adjacent 'phase matching' layers. As discussed previously [5], a resonant tunneling passband can occur when the effective admittance (η_{EFF}) of this tri-layer is made real and equal to the effective admittance 'looking into' the periodic-multilayer-coated prisms (i.e. η_Q, labeled in Figure 3.1). In

[5], we provided a partial analytic theory for achieving such a condition. We also showed that admittance matching for TE-polarized light resulted in rejection of TM-polarized light over a broad wavelength range, and vice-versa. As mentioned above, this polarizing property conveys a significant advantage over conventional tunneling-based filters. In the following, we present a more complete theoretical treatment, which provides additional insight and allows a more rational design of the desired flat-top bandpass filter response. In the interest of brevity, we will restrict the discussion to the case of designing a TE-polarization passband; the TM-polarization design follows easily [5].

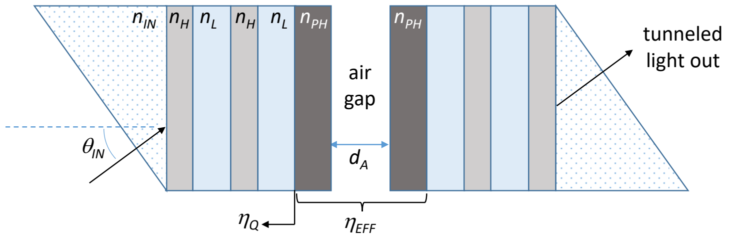

Figure 3.1. A schematic illustration of the tunneling filter concept is shown. Light is incident at an angle subject to total internal reflection at the air gap interfaces. The air gap is symmetrically bounded by prisms, each coated with a periodic Bragg reflector (2-period case shown) terminated by a 'phase-matching layer ($n_{PH} = n_L$ here). The air gap and the phase matching layers can be replaced by an 'equivalent' layer with effective admittance η_{EFF} at a given input angle and wavelength. For resonant tunneling to occur, η_{EFF} and η_Q (the admittance 'presented' by the periodic multilayer/prim substrate combination must be real and equal.

The symmetric tri-layer comprising the air gap and the phase matching layers can be replaced by an equivalent layer with effective admittance η_{EFF}, where [75]:

$$\eta_{EFF} = \eta_{PH} \left\{ \frac{\sin 2\delta_{PH} \cosh \mu_A - B \cdot \cos 2\delta_{PH} \sinh \mu_A - A \cdot \sinh \mu_A}{\sin 2\delta_{PH} \cosh \mu_A - B \cdot \cos 2\delta_{PH} \sinh \mu_A + A \cdot \sinh \mu_A} \right\}^{1/2} \quad . \qquad 3.1$$

Here, $\delta_{PH} = (2\pi/\lambda)\cdot(n_{PH}\cdot d_{PH}\cdot\cos\theta_{PH})$ and $\eta_{PH} = n_{PH} \cos\theta_{PH}$ are the phase thickness and 'tilted' optical admittance (in free-space units and for TE-polarized light) [17] of each phase-matching layer, θ_{PH} is the propagation angle, and n_{PH} and d_{PH} are the refractive index and thickness of these layers. For angles that produce tunneling conditions, the air gap is equivalent to a lossless metal layer with a purely imaginary tilted admittance, $\eta_A = \cos\theta_A = -i\cdot(n_{IN}^2\sin^2\theta_{IN}-1)^{1/2}$. Following Macleod [75], we define $\kappa_A = (n_{IN}^2\sin^2\theta_{IN}-1)^{1/2}$ and $\mu_A = (2\pi/\lambda)\cdot\kappa_A\cdot d_A$ as the (effective) real admittance and phase thickness of this layer, respectively. Finally, here $A = (\kappa_A/\eta_{PH} + \eta_{PH}/\kappa_A)/2$ and $B = (\kappa_A/\eta_{PH} - \eta_{PH}/\kappa_A)/2$.

Equation 3.1 allows the effective admittance to be calculated for a given set of (air gap and phase matching) layer thicknesses and input angle. We previously described [5] how to analytically predict the value of d_{PH} needed to produce a real value of η_{EFF} for a given combination of d_A and θ_{IN}. Once d_{PH} is determined accordingly, a matching stack of quarter-wave (i.e. for a given θ_{IN}) high- and low-index layers can be chosen to produce a real η_Q (see Figure 3.1) as close as possible to the resultant η_{EFF}, thereby producing a resonant tunneling passband. However, that design procedure involves trial-and-error and iteration. For a given input medium (i.e. prism) and input angle θ_{IN}, a more direct synthesis results from first choosing a quarter-wave matching stack (QWS), which for assumed lossless materials results in an easily calculated and real value of η_Q. Then, the exercise is to determine combinations of d_{PH} and d_A which result in $\eta_{EFF} = \eta_Q$. Starting from Eq. 3.1, the following relationship between μ_A and δ_{PH} (i.e. for a given $\eta_{EFF} = \eta_Q$) can be derived using an analysis similar to that of van der Laan et al. [81]:

$$\mu_A = \cosh^{-1}\left[\frac{B\cdot\cos 2\delta_{PH} - A\cdot C}{\left\{A^2\cdot\cos^2 2\delta_{PH} - 2\cdot A\cdot B\cdot C\cdot\cos 2\delta_{PH} + A^2\cdot C^2 - 1\right\}^{1/2}}\right] . \tag{3.2}$$

Here, $C = (h+h^{-1})/(h-h^{-1})$, where $h = \eta_{EFF}\ /\eta_{PH}$ and η_{PH} is the tilted admittance of the phase matching layers.

At this point, it is useful to consider a specific example. For comparison to our previously reported TE filter [5], we assume $\lambda = 1550$ nm, $n_H = 3.7$ (representing a-Si), $n_L = n_{PH} = 1.46$ (representing SiO_2) and $n_{IN} = 1.44$ (representing fused quartz prisms). Furthermore, we assume $\theta_{IN} = 48$ degrees, and that the matching stack has the form $(H\cdot L)^Z$, where H and L represent quarter-wave layers ($d_H = 109.4$ nm and $d_L = 390.2$ nm at this angle), and Z is the number of periods. For such a stack, $\eta_Q = \eta_{IN}\,(\eta_L/\eta_H)^{2\cdot Z}$, resulting in $\eta_Q << 1$, as necessary to match the typical values of real η_{EFF} attainable for the air gap tunneling layer and TE-polarized light [5]. For TM-polarized light, $\eta_{EFF} >> 1$ is typical, and $(H\cdot L)^Z\cdot H$ matching stacks are thus appropriate. Figure 3.2(a) is a plot of solutions to Eq. 3.2, in the range $0 < \delta_{PH} < \pi/2$ [81], for $Z = 1$, 2, and 3, corresponding to $\eta_Q = 7.6\text{x}10^{-2}$, $6.0\text{x}10^{-3}$, and $4.7\text{x}10^{-4}$ (in free-space units [17]), respectively. As is evident, an infinite number of combinations of d_A and d_{PH} can produce the required admittance match in each case. However, note that each curve is peaked, and that the location of the peak (versus d_{PH}) is relatively independent of η_Q (i.e. of Z).

The shape of the curves in Figure 3.2(a) can be understood from the fact that the physical basis for resonant tunneling is the excitation of coupled surface modes at the air interfaces [76,77,82]. In general, these two coupled surface states result in two transmission peaks, associated with a symmetric and an anti-symmetric 'super-mode' (see Fig. 4 of [76]). For a given curve, the maximum (e.g. points 1, 4 or 5 labeled in Figure 3.2(a)) corresponds to a critical coupling condition at which the symmetric and anti-symmetric resonances merge, producing a single flat-top transmission feature [76]. On the left side of this maximum (e.g. point 2 labeled in Figure 3.2(a)), every point on the curve represents a combination of d_A and d_{PH} that aligns the symmetric mode (i.e. lower energy) tunneling peak to the design wavelength. On the right side of the maximum (e.g. point 3 labeled in Figure 3.2(a)), every point aligns the anti-symmetric mode (i.e. higher energy) tunneling peak to the design wavelength. This behavior is confirmed by the transfer-matrix [17] simulation results shown in Figure 3.2(b), which are for the $Z = 2$ stacks and for three combinations of d_A and d_{PH} (labeled as points 1,2, and 3 in Figure 3.2(a)) that lie on the admittance-matching curve.

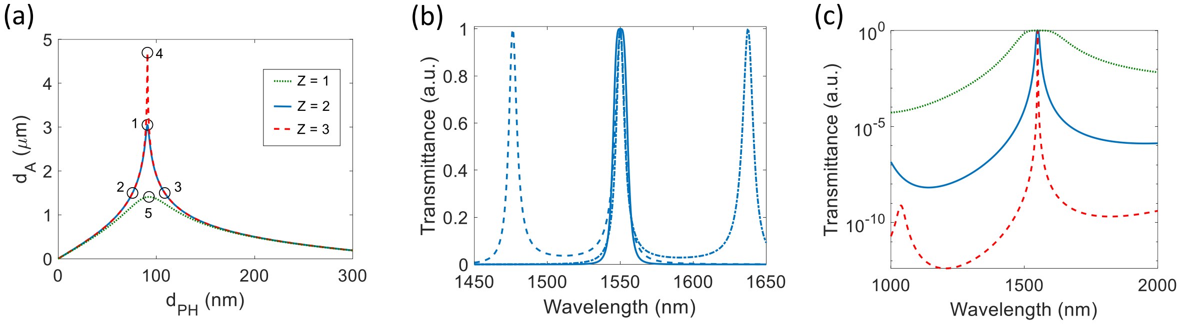

Figure 3.2. (a) Plots of d_A versus d_{PH} that produce an admittance match to 1, 2, and 3 period quarter-wave stacks, for $\lambda = 1550$ nm and $\theta_{IN} = 48$ degrees. The circled data points are referenced in subsequent plots. (b) Plots of transmittance versus wavelength for the 2-period QWS case, and for the combinations of d_A and d_{PH} labeled as points 1 (blue solid line), 2 (blue dashed line) and 3 (blue dash-dotted line) in part (a). (c) Plots of transmittance versus wavelength for the combinations of d_A and d_{PH} corresponding to the peaks of the curves in part (a), labeled as points 1 ($Z = 2$, blue solid line), 4 ($Z = 3$, red dashed line), and 5 ($Z = 1$, green dotted line).

Thus, the maximum of any particular curve of the type shown in Figure 3.2(a) represents a particularly desirable condition for bandpass filtering applications. The location of this maximum can be determined analytically by differentiating Eq. 3.2, leading to a quadratic solution:

$$\begin{aligned}
&\cos 2\delta_{PH}^{\#} = \frac{-b+\sqrt{b^2-4ac}}{2a} \quad , \\
&a = 2AB^3C - 2A^3BC \approx -2AB^3 + 2A^3B \quad , \\
&b = 2A^4C^2 + 2B^2 - 2A^2B^2C^2 \approx 2A^4 + 2B^2 - 2A^2B^2 \quad , \\
&c = -2ABC \approx 2AB \quad .
\end{aligned} \qquad 3.3$$

Here $\delta_{PH}^{\#}$ indicates the required phase thickness to achieve a flat-top passband, and the correct sign of the quadratic root was ascertained by checking the solutions against Eq. 3.1. The approximate forms of the coefficients in Eq. 3.3 reflect the fact that for TE-polarized light we typically have $\eta_{EFF} << 1$ (see example above) and thus $C \sim -1$. This furthermore explains the relative insensitivity of the peak location to $\eta_{EFF} = \eta_Q$, as observed in Figure 3.2(a). Once $\delta_{PH}^{\#}$ is determined, $d_{PH}^{\#}$ follows directly and $d_A^{\#}$ is easily calculated by substitution back into Eq. 3.2. As an example, for λ = 1550 nm, Z = 2, and θ_{IN} = 48 degrees, and the indices mentioned above, solution of Eqs. 3.3 and 3.2 produces $d_{PH}^{\#}$ ~ 91 nm and $d_A^{\#}$ ~ 3.05 μm, in agreement with the graphical results in Figure 3.2.

As the number of periods in the quarter-wave stacks is increased, the flat-top resonant tunneling passband becomes increasingly narrow. This can be traced to the higher phase dispersion and reflectance for increasing Z. The transmittance curves for flat-top passband conditions and Z = 1, 2, and 3 (corresponding to points labeled as 5, 1, and 4, respectively, in Figure 3.2(a)) are plotted in Figure 3.2(c). A flat-top passband condition is confirmed in each case, but with the FWHM dropping from ~140 nm to ~12 nm to ~0.8 nm, and the out-of-band rejection also increasing dramatically with increasing Z. Note that the secondary 'peak' near 1000 nm wavelength for the Z = 3 case is actually the edge of the 'stop band' associated with the matching stacks. Thus, the out-of-band rejection in these filters is attributable to both TIR at the air interface and coherent back-scattering within the periodic matching stacks. The narrow bandwidth and high out-of-band rejection predicted for the Z = 3 case is intriguing, but our numerical simulations indicate that this pass-band could only be observed with extremely well-collimated light and extremely high symmetry in the matching stacks, consistent with [76]. For example, if the thickness of the two phase matching layers (which is particularly critical) is mismatched by only ~ 0.2%, the predicted peak transmission is reduced by approximately half. The observation of such narrow passbands remains an interesting topic for future study, but might be impractical for most applications.

On the other hand, our previous work, which employed a conventional magnetron sputtering system [5], has already demonstrated the practicality of the Z = 2 case. The mismatch can be as high as 2-3% in this case, without significant degradation of the pass-band characteristics. Moreover, the angular sensitivity of the pass-band, while still high, is within a range that is compatible with off-the-shelf collimation optics (see Section 3.5). For these reasons, we restrict the remainder of the discussion to the Z = 2 case.

3.4 Tuning by varying the air gap and angle

We turn our attention to the prospect of achieving a tunable version of the filter described in Section 3.3. One option would be to implement a linearly varied version of the filter, where all layers (including the air gap) are proportionally tapered along one axis. However, this would be a rather challenging structure to fabricate. Moreover, linearly varied tunable filters (LVTFs) tend to suffer from slow tuning speeds, due to the need for linear translation of a large part, and passband broadening, due to spatial convolution effects [6]. Angular tuning of thin film filters is an alternative approach, which has been used extensively for narrow-range tuning in fiber systems and more recently for moderate-range tuning in fluorescence and Raman spectroscopy systems [7,8]. The latter work uses specialized thin-film filters (with high layer count) developed by Semrock [6], which can be tuned over a range equal to ~10% of their normal-incidence passband center wavelength. Angle-tuning is also the mechanism employed in most grating-based tunable filters including the VBG filters discussed above [4].

The principle of the proposed tunable filter is illustrated schematically in Figure 3.3(a). Assume that the prisms are uniformly coated with a thin film stack, designed to provide an admittance-matched tunneling band at a particular wavelength and incident angle, as described in Section 3.3. For illustration purposes, we will assume the values cited for the 2-period filter above (i.e. $n_{IN} = 1.44$, $n_H = 3.7$, $n_L = n_{PH} = 1.46$, $d_H = 109.4$ nm, $d_L = 390.2$ nm, and $d_{PH^\#} = 91$ nm) representing a QWS at $\theta_{IN} = 48$ degrees, terminated by a phase adjusting layer chosen to produce a flat-top bandpass response centered at 1550 nm wavelength. Now consider changing the incident angle to some new value θ_{IN}^*. At this new angle, the matching stack (i.e. *HLHL*) is no longer a QWS, either at 1550 nm or at any other wavelength, and its input admittance is in general complex, $\eta_Q = \eta_Q' \text{-i} \cdot \eta_Q''$, as easily calculated for example using transfer matrices. At any given wavelength, a real input admittance can be restored by adding an 'extra' low-index layer of phase thickness [17]:

$$\Delta\delta = 0.5 \cdot \tan^{-1}\left[\frac{2\eta_Q''\eta_L}{\eta_L^2 - (\eta_Q')^2 - (\eta_Q'')^2}\right] \quad , \qquad 3.4$$

where the tangent should be evaluated in the first or second quadrant. This corresponds to an 'extra' physical thickness of low-index material $\Delta d(\lambda) = (1/2\pi) \cdot \{\Delta\delta(\lambda)/\eta_L\}$, which can be positive or negative. This effectively moves the boundary between the matching stack and the phase matching layers, as depicted in Figure 3.3(a), such that the effective admittance η_Q^* (looking in from the new boundary) is a real quantity. From another point of view, the physical thickness of the phase matching layers is effectively changed from $d_{PH^\#}$ to $(d_{PH^\#} - \Delta d(\lambda))$. As shown in Figure 3.3(b), $\Delta d(\lambda)$ is a negative quantity at wavelengths much below the original design wavelength and monotonically increases towards positive values at long wavelengths.

Now, at the new input angle and using $\eta_Q^*(\lambda)$ determined above, Eqs. 3.2 and 3.3 can be solved to determine the values of phase-matching layers and air gap thicknesses, $d_{PH}^*(\lambda)$ and $d_A^*(\lambda)$, respectively, that are required to produce a flat-top tunneling passband. For a given angle, the spectral location of this passband is thus determined by the following condition:

$$d_{PH}^*(\lambda) = d_{PH}^{\#} - \Delta d(\lambda) \quad . \tag{3.5}$$

A graphical solution of Eq. 3.5, for an input angle of 53 degrees, is depicted in Figure 3.3(b), predicting an admittance-matched tunneling passband at $\lambda \sim 1322.7$ nm. Using the resultant value of $d_{PH}^* \sim 132$ nm, the required air gap thickness from Eq. 3.2 is $d_A^* \sim 1.94$ µm. To further understand this behavior, recall that the principle requirement for admittance-matched tunneling is that there exists a central tri-layer whose effective admittance η_{EFF}^* (at a particular angle and wavelength) is real and matched to the real input admittance η_Q^* presented by the adjacent thin-film-coated prisms. This occurs at a single wavelength for each particular input angle.

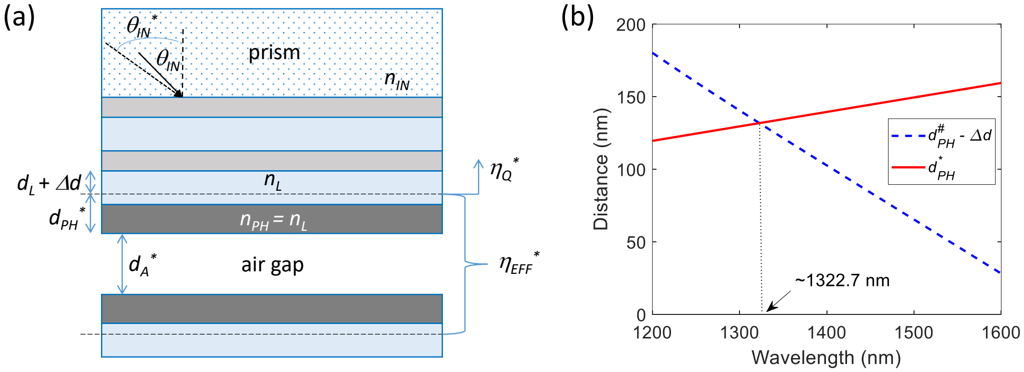

Figure 3.3. (a) A schematic illustration of the proposed tuning mechanism is shown. For a change in incident angle (θ_{IN} to θ_{IN}^*), the effective position of the interface between the phase matching layer and the matching stack shifts by some amount Δd (which can be positive or negative). The flat-top tunneling passband occurs at a new wavelength for which η_Q^* and η_{EFF}^* are real and equal, and with the air gap thickness d_A^* tuned to an appropriate value. (b) An example of the graphical determination of the flat-top tunneling wavelength for a particular incident angle (53 degrees) is shown. As described in the main text, for each incident angle there is a single wavelength at which $d_{PH}^* = (d_{PH}^{\#} - \Delta d)$, which in turn makes η_Q^* real while also enabling $\eta_{EFF}^* = \eta_Q^*$ through appropriate choice of d_A^*.

It follows that the spectral position of the flat-top pass-band can be continuously varied over a wide range by simultaneously tuning the air gap thickness and the incident angle. Plots of the predicted resonant tunneling wavelength, and the corresponding required air gap thickness, are shown in Figure 3.4. For the matching stacks assumed above, continuous tuning over a wavelength range from ~1000 nm to ~1800 nm is possible through angular tuning in the ~ 44 to

62 degrees range and corresponding air gap thicknesses in the ~ 7 to 1 μm range. Results with refractive index dispersion (calculated using previously described models for our sputtered SiO_2 and a-Si films [83]) taken into account are also shown.

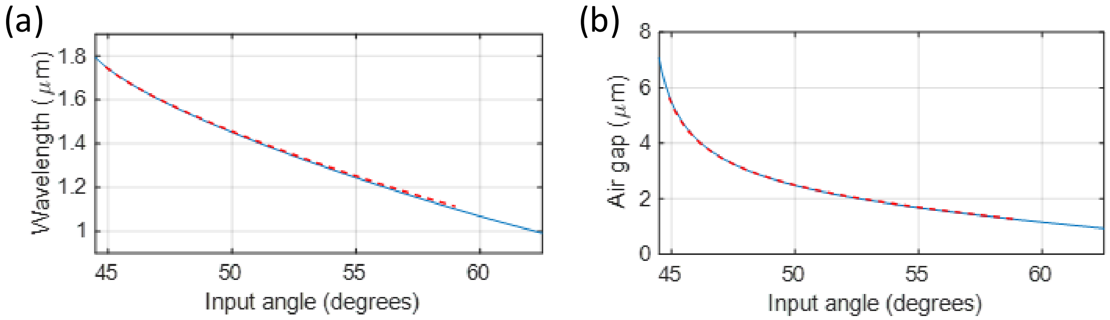

Figure 3.4. (a) Plot showing the predicted flat-top passband wavelength versus input angle, for the filter structure described in the main text. (b) Plot showing the predicted air gap thickness required to produce the flat-top passband at the corresponding wavelengths shown in (a). The solid (dashed) curves were calculated without (with) material dispersion taken into account.

Representative passbands, calculated using transfer matrices, are shown in Figure 3.5 for selected input angle and air gap combinations. Of course, unity transmission features are only possible in an idealized scenario neglecting loss and scattering. The impact of including absorption loss for the a-Si layers is shown for the two pass-bands near the opposite ends of the tuning range in Figure 3.5(a). We used an extinction coefficient model from our previous work [83], which gives κ_{aSi} ~ 0.006 and ~0.0006 at λ = 1000 nm and 1800 nm, respectively. As shown, the predicted impact on peak transmittance is tolerable, and is consistent with our previous experimental results [5]. Moreover, a-Si films have potential for significantly lower loss, for example through optimized hydrogenation [84].

As mentioned above, the high angular sensitivity of tunneling filters has traditionally been viewed as a major drawback, especially due to the existence of polarization-dependent pass-band splitting [68]. While the polarizing nature of the air gap tunneling filter described here significantly mitigates these issues, the high angular sensitivity of the polarized pass-band still limits the maximum acceptance angle. On the other hand, a high angular sensitivity imparts advantages, including the potential for wide tuning range and relatively fast tuning speeds [6]. The representative filter from above exhibits a shift in passband center wavelength on the order of ~40 nm / degree and pass-band bandwidths on the order of ~ 10 nm. For BPFs, the field of view (FOV) can be defined as the full angular width that results in a shift in center wavelength equal to half the passband width [16]. For the present filters, this implies that the incident light needs to be collimated with a half-angle less than ~ 0.5 mrad in order to avoid significant pass-band broadening. This is well within reach using commercial broadband collimators [85], as supported by our earlier experimental results [5] and confirmed below. It is also interesting to note that commercial VBG-based tunable filters have similar angular sensitivity and beam divergence restrictions [86]. Finally, it should be noted that it is always possible to limit angular acceptance through optical system design, to avoid passband broadening at the expense of throughput for sources with higher angular range. Similar tradeoffs are inherent in most diffraction grating instruments.

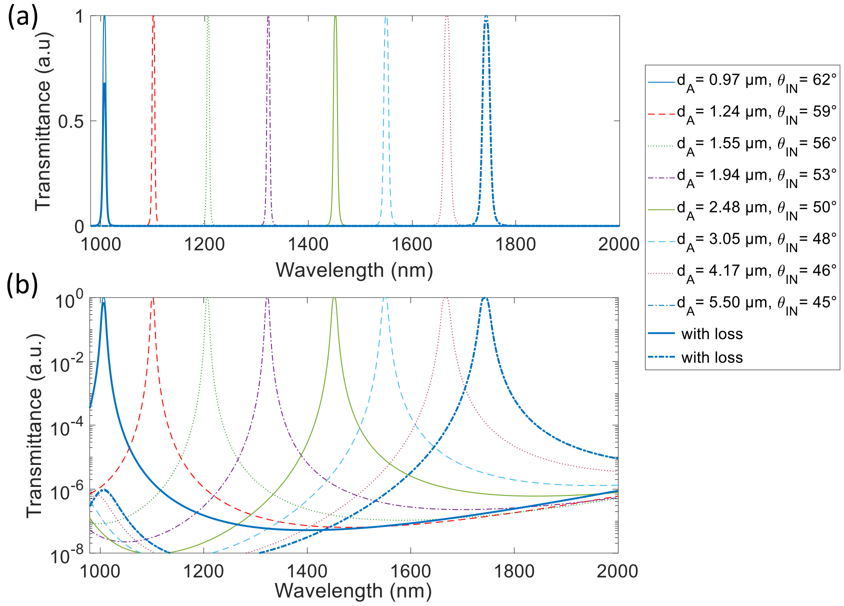

Figure 3.5. (a) Transmittance versus wavelength for a series of input angle combinations corresponding to the flat-top passband conditions depicted in Figure 3.4. A flat-top pass-band centered at the predicted wavelength is verified in each case. The FWHM linewidth varies from ~ 10 nm at the short wavelength end of the range to ~ 20 nm at the long wavelength end. For the two cases near the ends of the tuning range, the bold curves were calculated with the inclusion of absorptive loss for the a-Si layers (see main text). (b) The data from part (a) is shown on a logarithmic scale in order to reveal the predicted out-of-band rejection.

3.5 Experimental results

As an initial proof-of-concept, we assembled the system depicted in Figure 3.6(a), by using nearly hemi-cylindrical lenses (uncoated N-BK7 glass, Edmund Optics, stock #35-020) for the coupling prisms. They were first mounted in a custom holder to facilitate sputtering deposition of Si/SiO_2 matching stacks onto their flat faces. In order to improve film adhesion between the matching stacks and the N-BK7 prisms, a thin (10-20 nm) layer of SiO_2 was first deposited, followed by two-period (i.e. Z = 2) stacks with layer thicknesses nominally as described in Sections 3.3 and 3.4.

Next, pairs of lenses with well-matched coatings, as verified by photospectrometer measurements, were clamped together, and piezo-electric stack actuators (Thorlabs part no. PK2JA2P2) were glued to the lenses at each end (see Figure 3.6(b)). In the following, we will refer to the piezo-bonded pair of hemi-cylindrical lenses as simply the 'prism assembly'. Assuming the coated lens faces are flat and clamped in intimate contact, the 'resting' value of the air gap is approximately zero. The chosen piezo-actuators allow this gap to be increased up to a maximum value of ~8 μm.

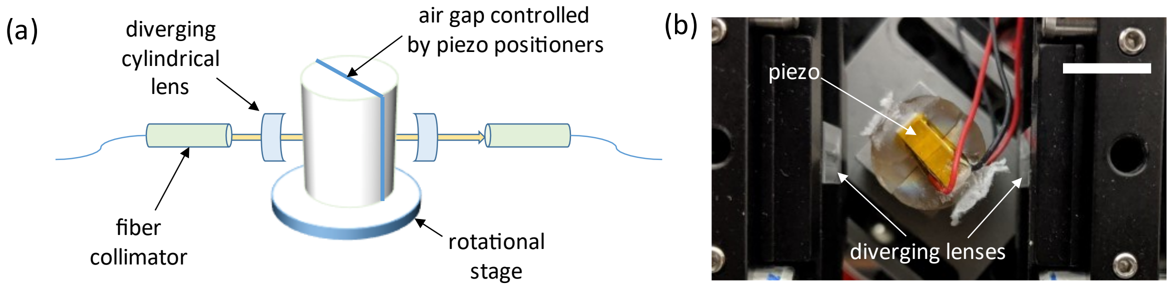

Figure 3.6. (a) Schematic depiction of the tunable filter assembly. Tuning is achieved by simultaneously controlling the incident angle (using a motorized rotational stage) and the thickness of the air gap between the matched hemi-cylindrical lenses. (b) Overhead photograph of the prism assembly mounted in an optical rail system (scale bar: 1 cm).

The choice of BK-7 coupling prisms, in place of the fused silica prisms used previously [5] and assumed for the theoretical treatments above, was motivated by the availability of suitable off-the-shelf lenses. This change has minimal effect on the operation of the filter, other than to shift the angular position of the resonant passbands to slightly smaller values, in keeping with Snell's law. For example, the 1550 nm flat-top passband predicted at ~ 48 degrees in Figure 3.4 and Figure 3.5 for fused silica prisms (n ~1.44) instead occurs at ~ 46 degrees for BK-7 prisms (n ~ 1.5).

The prism assembly was mounted on a rotational stage and aligned between fiber collimators (achromatic fiber ports, Thorlabs part no. PAF2-A4C). The use of hemi-cylindrical (or, as discussed below, hemi-spherical) input/output coupling prisms allows the angle of incidence to be varied by rotation of the prism assembly, without significant deflection of the beam path for a well-centered system. Diverging cylindrical lenses (Thorlabs part no. LK1363L2) were positioned between the collimators and the prism assembly, to cancel the focusing effects imparted by the curved surfaces of the coupling prisms. The lens focal lengths and positions were optimized through ray-tracing simulations (Zemax). Light from a broadband source, either a multiple-SLED-based instrument (LuxMux BeST-SLED) or a laser supercontinuum source (NKT

SuperK Compact), was coupled via a polarization maintaining single mode fiber (SMF). The results shown below correspond to TE polarized input light. We verified (not shown) that the filters provide strong rejection of TM-polarized light (~ OD4) across the entire wavelength range considered [5].

Light transmitted through the filter assembly was collected into a SMF or MMF and delivered to an optical spectrum analyzer (Yokogawa AQ6370B). All data shown below were obtained using the SMF output; the MMF output was used to more accurately assess the optical throughput of the prism assembly. Typical fiber-to-fiber insertion loss at the peak of the passband was ~ 10 dB for the SMF output and ~5 dB for the MMF output. Note that the tunneling filter, on its own, can exhibit very low insertion loss for well-collimated light, as per the results from Section 3.4 and as verified for a fixed filter previously [5]. Most of the extra insertion loss observed here can be attributed to the multiple uncoated surfaces in the optical path, and to imperfect compensation of beam divergence by the cylindrical surfaces. We expect that lower insertion loss can be achieved through further optimization, in particular if the cylindrical coupling prisms are replaced by spherical coupling prisms as discussed below.

For these studies, SMF-to-SMF coupling was optimized at a single wavelength and the coupling and alignment optics were then fixed as the passband wavelength was tuned. All experimental curves were spectrally calibrated against a base scan for the broadband source, captured without the prism assembly and diverging lenses in the optical path, and were normalized to their peak value to facilitate direct comparison with theory. Notably, the insertion loss was nearly constant (within ~ 2 dB) across the entire tuning range, verifying that small changes in angle and air gap do not significantly alter the beam path.

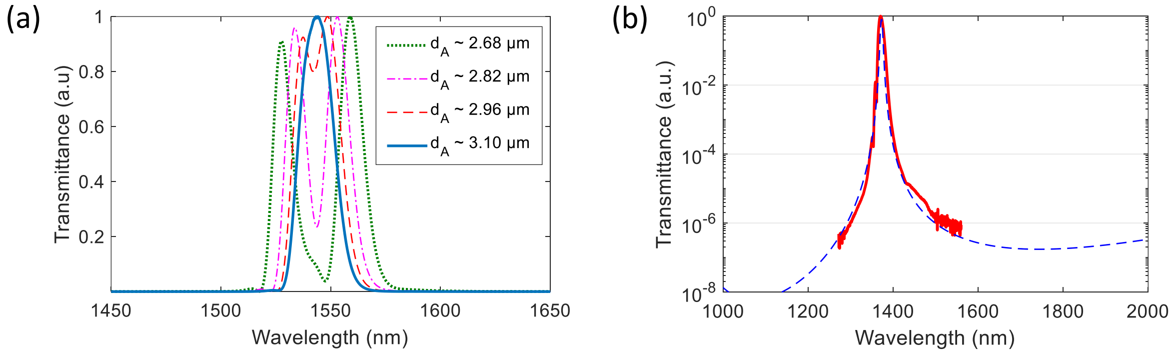

Figure 3.7. (a) Experimental passband centered near 1550 nm wavelength for an incident angle ~ 46 degrees and various values of the air gap thickness. The legend indicates the estimated gap in μm (see main text). (b) A typical passband feature (at ~1370 nm wavelength) is shown on a logarithmic scale, as theoretically predicted (blue dashed curve) and measured (red solid curve).

Figure 3.7(a) shows transmission curves for a typical passband centered near 1550 nm and for several different air gap thicknesses. Here, the incident angle was fixed and the piezo voltage was stepped in increments of 4 V, corresponding to increments in the air gap of ~ 0.14 μm. In keeping with the theoretical predictions, two separate peaks are observed for low values of the air gap thickness, and these peaks merge to produce a single passband feature when the air gap thickness is increased to an appropriate value.

Figure 3.7(b) shows a typical flat-top passband plotted on a logarithmic scale, revealing good agreement between theory and experiment. Some small notches were typically observed in the experimental data, and are likely artifacts arising from imperfect calibration. Notably, they were observed only in the case of SMF-to-SMF coupling, while different artifacts (a periodic ripple in the passband) was observed for SMF-to-MMF coupling. The measured out-of-band-rejection of ~OD4 at +/- 25 nm and ~OD6 at +/- 100 nm is in very good agreement with theoretical predictions. Theory also predicts higher rejection outside this interval, but the limited dynamic range of our experiment prevented direct corroboration.

We subsequently verified that we could tune the passband over a wide range of wavelength by simultaneously adjusting the incident angle and the air gap thickness. Figure 3.8(a) shows representative passbands spanning the ~ 1250-1700 nm wavelength range. From normal-incidence measurements, the prism assembly was determined to have a resting-point air gap of ~ 1.8 μm. This is likely attributable to the manual nature of the assembly, and prevented us from demonstrating passbands at shorter wavelengths. On the long wavelength end, we were limited by the operational range of our sources and the available OSA. The measured flat-top passbands exhibit wider FWHM linewidths (by ~40-50 %) compared to the theoretical predictions in Figure 3.5. This might be attributed to imperfect collimation of the input beam (angular convolution effects) combined with non-uniformities in the air gap and thin film thicknesses (spatial convolution effects), but is the subject of ongoing study. Nevertheless, the global behavior of the tunable filter is in excellent agreement with predictions.

Figure 3.8(b) shows a comparison of the theoretically predicted and experimentally observed combinations of incident angle and air gap thickness needed to observe the flat-top passband feature versus wavelength. The theoretical curves were based on the analysis in Sections 3.3 and 3.4, but with N-BK7 coupling prisms and a phase matching layer thickness of 88 nm assumed (as estimated from photospectrometer measurements). The experimental air gaps were estimated based on the manufacturer-supplied voltage-extension curve for the piezo actuators, under ‘low stiffness’ loading conditions [87]. The experimental angles were estimated from overhead images of the prism assembly captured by a camera (see Figure 3.6(b) for example) at one particular setting, and then using the incremental angle readout supplied by the motorized rotational stage. Error bars for the air gap represent the range of voltage-extension variation (+/- 15%) specified by the manufacturer, and the error bars for the angle represent the estimated accuracy (+/- 0.02 rad) for the angle extracted from the camera images.

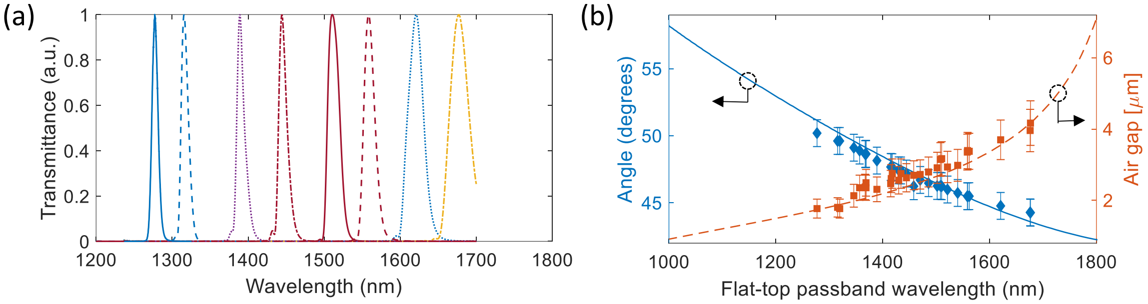

Figure 3.8. (a) Experimental passbands centered at various wavelengths in the ~1250 – 1700 nm wavelength range, corresponding to selected combinations of angle and air gap indicated by the symbols in part b. FWHM linewidths vary from ~ 15 nm to ~ 30 nm, approximately 50% larger than the theoretical predictions shown in Fig. 5. (b) Comparison between theoretical and experimental combinations of air gap thickness (dashed curve and square symbols) and incident angle (solid curve and diamond symbols) required to observe a flat-top passband versus wavelength.

3.6 Discussion and conclusions

We have described and demonstrated a new type of bandpass filter, with potential to be tuned across a large portion of the near infrared spectrum. The physical basis of the filter is admittance-matched tunneling of light through an air gap, where the matching is achieved using a simple (4-layer) thin film stack. The spectral position of the resonant passband is tuned through simultaneous adjustments in the incident angle and the air gap thickness. We fabricated and tested a proof-of-principle system using hemi-cylindrical input/output prisms with an intervening air gap controlled by piezo actuators. Experimental results provided good corroboration of the theoretical predictions. Even simpler systems can be envisioned using hemi-spherical prisms, which might act as both the coupling and collimating/focusing elements and thereby eliminate the need for additional lenses. Moreover, systems operating in different wavelength regions (e.g. the visible band) could be realized through the use of appropriately transparent thin-film materials. It is also worth noting that resonant tunneling filters have recently been implemented in an on-chip MEMS platform [88]; this might be an interesting avenue to explore for miniaturization and integration of the present filter.

A further advantage is that operation of the tunable filter is not particularly sensitive to the exact thicknesses of the thin film matching layers, as long as the stacks are well-matched on each side of the air gap [5,76]. Thickness errors simply result in slight changes in the combinations of angle and air gap needed to observe the flat-top passband at a given wavelength. The ability to adjust the tunneling layer thickness during operation thus makes the filter quite robust to variations in the fabrication process. Moreover, it might be interesting to explore strategies for post-fabrication compensation or fine-tuning (e.g. through thermal tuning of the refractive index) of the matching stacks.

Finally, it is worth reiterating that resonant optical tunneling filters, after a few decades of study, were essentially deemed as impractical in the late 1960s [68], with Baumeister concluding: "It is doubtful if the single tunnel layer filter will ever be produced as a practical bandpass filter, owing to its disadvantages of a large angle shift and its strong polarization." To our knowledge, this viewpoint has not changed significantly in the past 50 years, with resonant tunneling filters attracting only sporadic interest and mainly as a theoretical curiosity [17,88]. The filter described here in large part addresses the drawbacks that contributed to such a gloomy perspective. The use of an air gap tunneling layer enables convenient substrates and incident angles [74], and the use of high-index-contrast matching stacks can result in a strong rejection of one polarization state – i.e. the filter simultaneously plays the role of a polarizer, rather than exhibiting polarization-dependent passbands. By introducing an adjustable tunneling layer, the need for extreme control over thin film thicknesses is removed. Moreover, the tunable air gap allows us to turn the angular dependence into an advantage, potentially enabling passband tuning over a very large wavelength range. Combined with the modern ability to deposit thin films having vanishingly low absorption and scattering losses, our approach could spur renewed interest in the practical application of tunneling-based filters.

Chapter 4 Tunable bandpass imaging filter based on resonant tunneling through a ball lens assembly

This chapter has been submitted for publication to Applied Optics as T. R. Harrison, K. G. Scheuer, and R. G. DeCorby, “Tunable bandpass imaging filter based on resonant tunneling through a ball lens assembly”.

4.1 Introduction and background

Tunable bandpass filters are widely sought optical devices, especially for spectroscopy and radiometry [2,4,52]. Diffraction-grating-based monochromators, which can provide broad tuning range, bandwidth flexibility, and potentially high out-of-band blocking (particularly for double-grating instruments) are often used as tunable filters. However, they also introduce significant loss that scales in a nonlinear way with the resolving power [7], and do not typically preserve the wavefront of the input signal.

Many important applications require tunable filters with wavefront-preserving properties. For example, the emergence of fiber-based supercontinuum sources [4,47,89,90] has created a need for filters that are tunable within the visible-to-near-infrared (~ 400-2500 nm wavelength) region, and which preserve the Gaussian beam profile of the source [85]. As another example, tunable-filter-based hyper-spectral imaging systems (so-called ‘staring’ systems) [2,91] are widely sought for applications in both the visible and near-infrared (NIR) ranges [92,93]. Acousto-optic or liquid-crystal tunable filters are often used, but both suffer from high insertion loss and poor out-of-band blocking [2,52]. A newer alternative is the volume-Bragg-grating (VBG) [4], a diffraction-based device with wavefront-preserving capabilities. Instruments based on VBGs can provide low polarization dependence and loss, as well as high out-of-band rejection, but usually incorporate two or more gratings along with supplementary optics (retro-reflectors, collimation lenses) [47,50,86], and are relatively complex and costly.

Thin-film Fabry-Perot filters can address some of the limitations of existing instruments. Advances in computer-based design and deposition processes have enabled new options for bandpass tuning by linear or angular translation [7,8,52]. In order to achieve an extended tuning and out-of-band blocking range, these filters typically employ hundreds of layers [8]. Single-part linearly variable filters (LVF) can be tuned over a large range (e.g. ~400-900 nm) but through relatively slow translation of a large piece [89]. Angle-tuned filters can be tuned more rapidly, but are more limited in tuning range, such that several individual filters are needed to address broadband applications [4].

In earlier work [5,79], we described a bandpass filter based on an air gap tunneling layer between prisms coated by few-layer, high-index-contrast admittance-matching stacks. We furthermore demonstrated wide-range tuning by simultaneously adjusting the air gap thickness and the angle of incidence. A first-generation prototype was constructed using cylindrical lenses [79], and operation over the ~1000-1800 nm wavelength range was demonstrated. Here, we describe filters implemented using half-ball lenses as coupling prisms, and with operational ranges in both the visible and NIR. These ball-lens assemblies can function as extremely compact fiber- or aperture-coupled spectrometers, or as the tunable filter in a compact hyperspectral imaging assembly.

4.2 Ball-lens spectrometer / tunable filter

4.2.1 Concept and operating principles

The proposed system is illustrated schematically in Figure 4.1(a). Two half-ball lenses are symmetrically coated by admittance-matching stacks and then configured with a small (μm-scale) air gap between them. From a high-level perspective (i.e. ignoring refraction effects, etc., in the matching stacks and air gap), the lens pair can be expected to function approximately as a single ball lens for transmitted light. As is well known, a ball lens can perform very well as a fiber-to-fiber coupling element [94]. Thus, as depicted, an extremely compact spectrometer unit can be envisioned with appropriate positioning of input and output apertures such that light is collimated inside the ball lens assembly [95]. As detailed in our previous work [79], spectral scanning (i.e. filter tuning) is achieved by simultaneously adjusting the angle of incidence (θ_{IN}) and the thickness of the air gap (d_A).

A key figure of merit for any spectrometer (or scanning tunable filter) is its light-gathering capability, often quantified by the so-called optical invariant or étendue [96]. The limiting étendue can be expressed as the product of the maximum solid input angle with the area of the maximum allowed input aperture. As depicted in Figure 4.1(b), the acceptance angle is determined by the projected aperture of the air gap, with the filter ball rotated to the maximum required value of the incident angle ($\theta_{IN,MAX}$). As discussed previously [79] and further below, typically $\theta_{IN,MAX}$ ~ 60 degrees, which corresponds to a limiting numerical aperture (NA) ~ 0.2. Also shown in Figure 4.1(b) is the angular spread corresponding to NA = 0.13, which is a typical value for standard single-mode optical fibers. Note that NA = 0.2 corresponds to an f/# ~ 2.5, comparable to that of many compact commercial spectrometers [96].

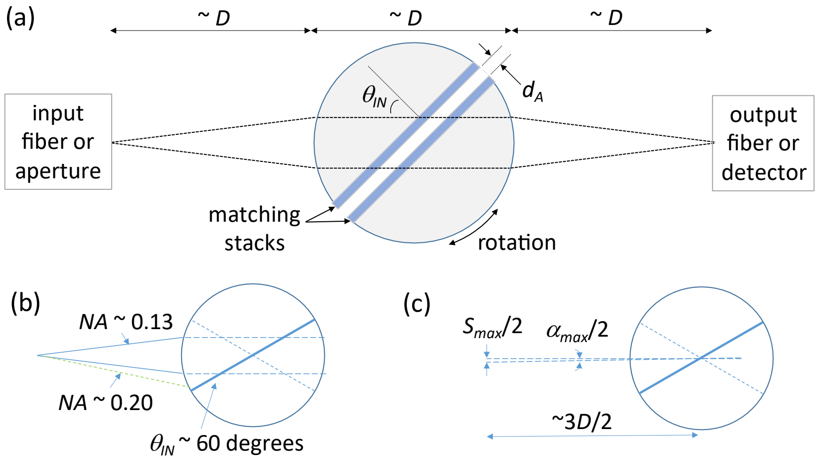

Figure 4.1 (a) Schematic illustration of the spectral filter assembly. Two half-ball lenses with nominally identical admittance-matching stacks are aligned in a jig that enables the incident angle (θ_{IN}) and the air gap thickness (d_A; shown at an exaggerated scale for illustration purposes) to be varied. The overall assembly functions approximately as a ball lens (i.e. for light that tunnels through the air gap), collecting and collimating input light from an appropriately positioned input aperture and focusing the output light (i.e. with focal length $f \sim D$). (b) Schematic showing the assessment of the acceptance angle, for the limiting case with θ_{IN} near its maximum required value. (c) Schematic showing the assessment of the maximum input aperture size, which is determined by the maximum allowed angular spread inside the ball lens assembly, to avoid passband broadening.

The maximum input aperture is determined by the need to ensure that the light incident onto the air gap is highly collimated, in order to avoid passband broadening. As depicted in Figure 4.1(c), and using a small-angle approximation, we can estimate $S_{MAX} \sim (3/2) \cdot D \cdot \alpha_{MAX}$, where S_{MAX} is the maximum diameter of the input aperture, α_{MAX} is the maximum allowable beam angular spread inside the ball lens, and D is the diameter of the ball lens. For the passband design discussed below, we've previously estimated $\alpha_{MAX} \sim 0.001$ rad [79]. Furthermore, we've chosen 10 mm diameter lenses for the experimental work here, resulting in $S_{MAX} \sim 15$ µm, compatible with the use of a standard single mode fiber as the input aperture. Note that this is not dissimilar to typical slit widths of compact diffraction-grating-based spectrometers available commercially, although in those instruments the slit height is typically much larger.

Taken together, this results in an étendue $\acute{E} = A \cdot \Omega \sim S_{MAX}^2 \cdot \pi^2 \cdot NA^2/4 \sim 2\text{x}10^{-5}$ mm^{2}Sr. This is a relatively small value, limited mainly by the input aperture, but nevertheless comparable to many integrated optic [97] and compact commercial [98] spectrometers. In principle, $\acute{E}$ could be increased by using larger ball lenses. However, the use of larger lenses also implies a larger optical system and a need to achieve uniform matching stacks and air gap over a wider area. In any case, the analysis illustrates that the ball lens assembly has potential as a fiber-coupled spectrometer/filter unit. It is also worth reiterating that ball lenses have found extensive use historically as fiber-fiber and fiber-chip coupling elements [94,95].

As mentioned, the design and operational principles of the filter have been detailed elsewhere [79]. In that previous work, a 4-layer a-Si/SiO_2 admittance-matching stack was implemented, enabling a tunable filter for the NIR range. The NIR filter discussed below uses the same matching stacks, but deposited on half-ball lenses rather than the half-cylindrical lenses used previously.

The concept can be adapted to other wavelength ranges, provided suitable thin film materials, with low optical loss and ideally high index-contrast, are available. To demonstrate this, we designed a tunable filter for the visible range, using the theory from our previous work [79] and with Ta_2O_5 ($n \sim 2.2$) and SiO_2 ($n \sim 1.46$) as the thin film materials. For example, an 8-layer matching stack, comprising alternating layers of Ta_2O_5 and SiO_2 with thicknesses ~ 85/162/85/162/85/162/85/200 nm is predicted to enable a filter that is tunable over the ~ 400–700 nm wavelength range. Note that these film thicknesses correspond to quarter-wave-layers at $\lambda_o = 650$ nm and for $\theta_{IN} = 45$ degrees. The last SiO_2 layer (next to the air gap) is thicker because it includes a 38 nm 'phase-matching' layer selected to produce, in combination with an appropriate air gap thickness, a flat-top tunneling pass-band for TE-polarized light (i.e. at $\lambda_o = 650$ nm and for $\theta_{IN} = 45$ degrees).

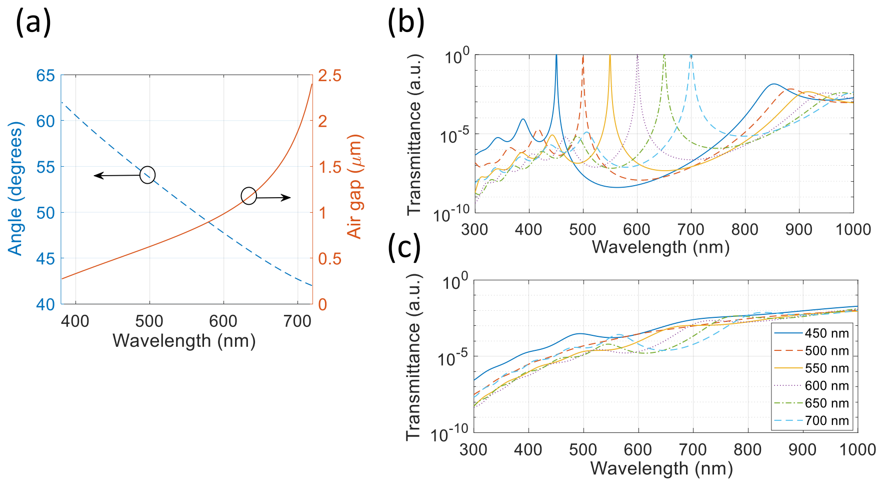

Figure 4.2 (a) Predicted combinations of incident angle (blue dashed curve) and air gap (red solid curve) that produce a flat-top resonant tunneling passband (for TE-polarized light) versus wavelength, as predicted for the visible-band tunable filter described in the main text. (b) Representative passbands for selected data points from the plots in part a, predicted using transfer matrix calculations. (c) Transmittance of TM-polarized light for the selected combinations of angle/air gap from part b. The legend indicates the position of the TE-polarized passband peak for each case.

The position of the flat-top passband can be tuned over a wide range by concurrently adjusting the air gap thickness and the incident angle [79]. The predicted combinations of air gap and incident angle that produce a flat-top passband versus wavelength are plotted in Figure 4.2(a), and representative passbands as predicted using standard transfer-matrix calculations are plotted in Figure 4.2(b). Passbands in the ~ 400-700 nm wavelength range can be accessed by varying the incident angle from ~ 60 to 42 degrees and the air gap from ~ 0.3 to 2 µm. This implies a high angular dispersion ~ 15 nm/degree (very similar to VBG filters [4,50,86]), which is favorable for rapid and wide angle-based tuning, but also limits the acceptance angle to avoid passband broadening as mentioned above. The predicted FWHM passband widths, which of course for transfer-matrix predictions pertain to perfectly collimated light incident onto the air gap, range from ~ 2 to 4 nm over the tuning range, corresponding to a resolving power ($\lambda/\Delta\lambda$) ~ 200. As shown below, and similar to previous results [79], the experimental passbands are approximately twice as wide, likely attributable to both angular and spatial convolution effects.

As discussed elsewhere [5,79], these tunneling filters also act as polarizers, strongly rejecting the non-admittance-matched TM-polarized light for the design discussed here. This is verified by the transfer-matrix predictions shown in Figure 4.2(c). The polarizing property, while not always desirable, is much preferable to the polarization-dependent passbands which hindered traditional bandpass filters based on optical tunneling [68]. Note that both the polarization rejection (~ 30-50 dB) and the blocking range (for out-of-band TE-polarized light) is somewhat inferior to the NIR filter described previously [5,79]. This can be attributed mostly to the lower index-contrast of the matching stacks used for the visible-range filter. Nevertheless, the out-of-band rejection is very good (>OD6), at least for filter settings near the central part of the tuning range. We anticipate that further improvements might be possible through the use of more advanced matching stacks, the design of which might be an interesting topic for future study.

4.2.2 Experimental results – tunable filter

Prototype ball-lens assemblies were constructed and tested as follows. First, half-ball lenses (N-BK7 glass, Edmund Optics 45-937) were placed in a custom holder and thin-film admittance matching stacks were deposited (by magnetron sputtering) onto their flat sides. Matched pairs of these lenses were then clamped using a custom jig (see Figure 4.3(a)), with their coated faces in nominal contact. The jig was designed to also hold a pair of piezo positioners (Thorlabs PK2JA2P2), which are used to control the thickness of an air gap between the two lenses. Both the lenses and the piezo stacks were glued in place, such that, after removal of clamping elements, the two sides of the assembly are free to move under the action of the piezos. This ball-lens assembly is subsequently mounted on a motorized rotational stage, so that both the incident angle and air gap are under computer control. As shown in Figure 4.3(b) and described in Section 4.3, these assemblies were assessed for potential use as the tunable filter in a compact spectral imaging system.

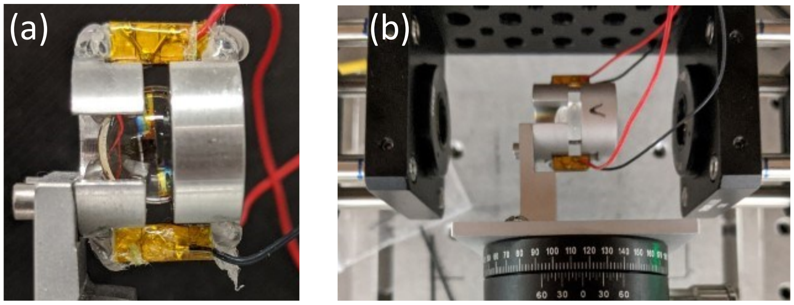

Figure 4.3 (a) Photograph of an assembled spectral filter. Two half-ball lenses are mounted in a custom holder along with a pair of piezo positioners. Actuation of the piezo positioners varies the air gap between the two lenses. (b) Photograph of the imaging setup, with the ball filter assembly mounted on a rotational stage approximately midway between a pair of achromat lenses (see Section 4.3).

Experimental scans were initially obtained with a fiber-fiber coupling arrangement as depicted in Figure 4.1. A standard SMF (OZ Optics SMJ-3S3A-1300/1550-9/125-3-2, 9 µm core) terminated by an FC/PC connector was used at the input. Either single-mode (SMF) or multi-mode fibers (MMF) (Thorlabs M16L01, with 50 µm core), also terminated by FC/PC connectors, were used at the output side. The FC/PC-terminated fibers were mounted in standard 5-axis micro-positioners to facilitate axial and angular alignment, and to optimize their positions with respect to the focal length of the ball-lens-assembly (see Figure 4.1(a)). Passband characteristics of both the visible- and NIR-range filters were measured using this fiber-to-fiber coupling arrangement, and also using the 'imaging' setup shown in Figure 4.3(b), with fiber collimators at the input and output ends in the latter case. Similar results were obtained for both setups, although slightly broadened passbands were typically observed for the fiber-fiber setup, likely due to inferior collimation of the input light passing through the ball lens. A supercontinuum laser (NKT SuperK Compact) was used as the input source and the transmitted light, at various filter settings, was captured by either an Ocean Optics USB4000 fiber-coupled spectrometer (for the visible-range filter) or by a Yokagawa AQ6370B optical spectrum analyzer (OSA) (for the NIR-range filter). Transmission scans were normalized to base scans obtained by coupling the source directly into the spectrometer. Typical representative passbands for both the visible- and NIR-range filters are shown in Figure 4.4.

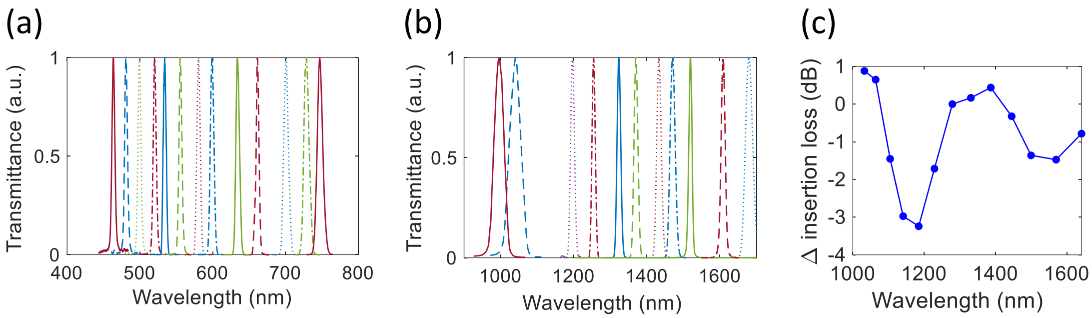

Figure 4.4 (a) Representative experimental passbands for the visible-band filter, which is continuously tunable over the ~ 460-750 nm range. (d) Representative experimental passbands for the NIR-band filter, which is continuously tunable over the ~ 1000-1800 nm range. (c) Change in insertion loss versus wavelength for the NIR-band filter, relative to the optimized insertion loss for the passband at 1279 nm and for output coupling into a MMF.

For the visible-range filter, we were only able to access passbands above ~ 450 nm wavelength. From normal-incidence spectral scans (not shown), we attributed this to a 'resting' air gap ~ 0.6 µm in thickness introduced during the manual assembly. Higher-quality optics (improved flatness and surface roughness) and a more sophisticated and automated assembly could likely address this shortcoming. The passband shown near 460 nm exhibits lower SNR, in part due to a higher-than optimal air gap (see Figure 4.2), but mainly due to the limited power spectral density of the source in this range.

As described previously [79], the NIR filter is tunable over the ~ 1000-1800 nm wavelength range by varying the incident angle between ~ 60 and 45 degrees and simultaneously adjusting the air gap between ~ 1 µm and 6 µm. The full designed range of the NIR device was accessible, although Figure 4.4(b) is truncated at the upper-limit wavelength (1700 nm) of the OSA used. The experimental FWHM linewidths are similar to the cylindrical-lens-based prototype [79]. However, for passbands with center wavelengths < 1100 nm, the aluminum jig used to hold the half-ball lenses impeded optimal location of the input and output fibers. This resulted in a less-collimated beam at the air gap and passband broadening due to increased angular convolution effects. This could be resolved through redesign of the jig and is left for future work.

System throughput was assessed using both SMF and MMF fibers at the output. For the MMF pickup and the NIR filter, the best-case pass-band insertion loss was ~ 4.5 dB, measured using a polarized broadband source (LUXMUX BeST-SLED) aligned to launch TE light [79]. For the visible-range filter, only the nominally unpolarized supercontinuum source was available, and the best-case insertion loss was ~ 6 dB for a MMF pickup. The insertion loss for coupling back into a SMF was typically 3-5 dB higher. Note that neither the fiber end facets nor the curved surfaces of the ball lenses were anti-reflection (AR) coated here. Furthermore, we believe that the manual assembly procedure resulted in imperfect alignment of the two half-ball lenses. This likely imparts a lateral offset, which would make the overall assembly somewhat aspherical. It might also result in an unintended wedge in the air gap thickness, which is predicted to broaden the pass-bandwidth and reduce peak transmission. Based on modeling results (not shown), we anticipate that significantly reduced throughput loss can be achieved with the addition of AR coatings and with improvements in alignment and assembly.

Perhaps equally important, given the proposed use of the ball-lens-assembly as a tunable filter configured between fixed input and output apertures, is the variation in the insertion loss across the tuning range. A typical result for the NIR filter is shown in Figure 4.4(c). For this experiment, the filter was first tuned to produce a flat-top passband at ~ 1279 nm wavelength and the input and output fiber positions were adjusted to maximize throughput. Then, without fiber or filter realignment, the change in insertion loss was recorded at various flat-top passband settings within the tunable range by rotating the filter stage and adjusting the air gap accordingly. As shown, insertion loss was actually lower at some settings, and overall there was no discernible trend. The maximum deviation in the insertion loss is ~ 3 dB, and it can likely be attributed in part to imperfect alignment and assembly of the ball lenses, which would cause the beam to be slightly re-directed on rotation. Furthermore, even slight non-centering of the ball-lens-assembly on the rotational stage is expected to further exacerbate such effects. Spatial variations and roughness in the matching stacks could also play a role, but a full understanding of these details is left for future work.

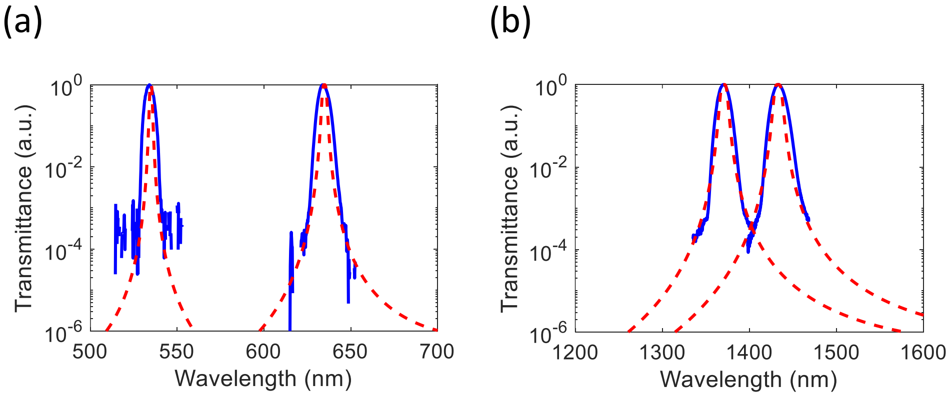

Figure 4.5 Representative experimental spectra (solid blue lines) are plotted on a logarithmic scale and compared to theoretical predictions (dashed red lines) for (a) the visible-range filter and (b) the NIR-range filter. For the theoretical curves, the air gap was selected to align the passband peak to the experimental result in each case.

In order to better assess the shape of the experimental passbands and the out-of-band rejection characteristics of the filter, representative passbands are plotted on a logarithmic scale in Figure 4.5, along with theoretical predictions from transfer matrix theory. The passband broadening mentioned above is evident, especially for the visible-range filter. The dynamic range of our experimental setup, combined with the insertion loss discussed above, did not allow the out-of-band rejection to be fully verified. However, note that we have previously confirmed [5,79] blocking >OD6 for similar NIR-range filters.

4.3 Hyperspectral imaging system using the tunable ball lens filter

4.3.1 Concept and system design

It is well known that ball lenses have unique imaging capabilities. Like all spherical lenses, they can introduce spherical aberrations. However, their inherent symmetry can eliminate many sources of aberrations and distortion in a properly configured system [99]. Moreover, they can accommodate a wide field of view and form high-resolution images on a centrosymmetric spherical imaging surface, a property which has recently made them key enablers of so-called "Gigapixel" imaging systems [100,101]. In a paraxial system with a flat imaging plane, spherical aberrations can be minimized by limiting the aperture angle and field angle [102] in the object space of the ball lens. For our filter, limiting the field angle also has the benefit of reducing pass-band variations arising from angular variations over the field of view. However, depending on the design of the optical system, tradeoffs between aberrations, pass-band variations, and insertion loss (i.e. due to reductions in étendue) [102] can be anticipated. A full study of these tradeoffs is left for future work. Here, we describe a proof-of-concept microscope assembly which uses the visible-range ball filter to achieve hyperspectral imaging.

The proposed imaging system is depicted in Figure 4.6(a). The ball-lens assembly is symmetrically configured between a pair of longer focal-length achromat lenses, forming a 1:1 relay system. This configuration, with appropriate choice of the input pupil, ensures that the bundle of rays passes mainly through the central portion of the ball lens (i.e. limits the aperture angle for the ball lens), and also ensures that rays from each point in the object space (not shown) are nominally collimated inside the ball lens assembly. Note, however, that longer focal-length achromats result in a larger range of field angles in the object space of the ball lens, which is expected to increase variations (over the field of view) in the pass-band of the tunneling filter. This could be mitigated by the use of larger ball lenses, without sacrificing étendue (see Section 4.2). Note that with the camera lens focused at ~ infinity, the angle sub-tended by the aperture of the exit achromat sets the field of view for this system. Also, the camera lens aperture can be adjusted to reduce aberrations at the expense of reduced light throughput.

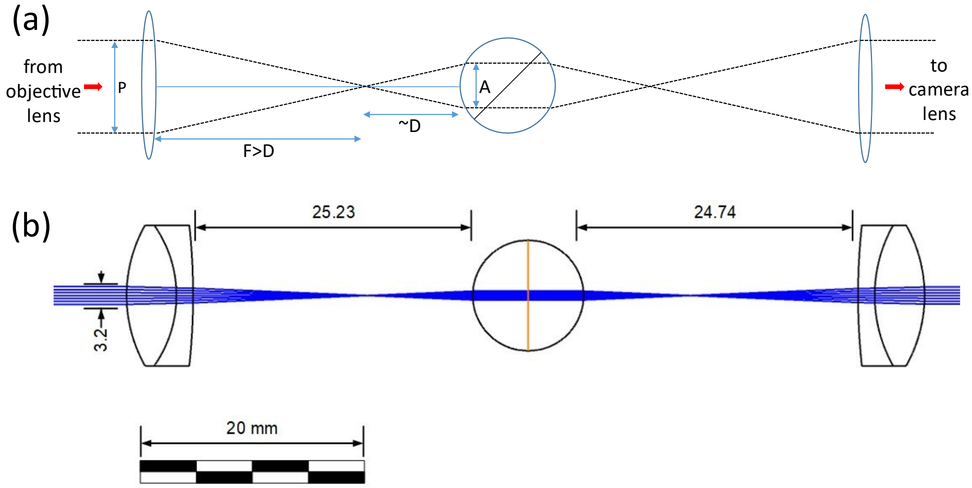

Figure 4.6 (a) Schematic illustration of an imaging system that incorporates the ball lens tunneling filter. The input pupil aperture (P) and supplementary lens focal length (F) are chosen according to a desired aperture (A) at the ball lens, and to limit angular spread of rays inside the ball lens. (b) Ray-tracing results for an object at the focal plane and on the optical axis of the objective lens (not shown), after optimization of the lens positions to achieve collimation inside the ball lens and collimation of rays delivered to the camera lens.

We implemented this system using anti-reflection-coated achromatic doublet lenses with a 19 mm focal length (Thorlabs AC127-019-A), as shown in Figure 4.3(b). For an object point on the optical axis, a ray-tracing model (Zemax) was used to optimize the spacing between the achromats and the ball lens, as depicted in Figure 4.6(b). The optimization criteria for the input achromat-to-ball spacing was the collimation of rays inside the ball lens, and for the output ball-to-achromat spacing it was the collimation of rays delivered to the camera lens (assumed to be focused at ~ infinity).

Of course, each point in the object plane will produce a bundle of collimated rays that passes through the tunneling-filter air gap at a unique angle. Given the angular dependence of the passband here, this furthermore implies that the passband center wavelength will vary radially within the field of view for a given filter setting. In other words, for a large field-of-view system, concentric 'rainbow' bands of color are expected in the image plane. This type of spectral passband variation over the field of view is a common feature of many other tunable filters used for hyperspectral imaging, including Fabry-Perot filters [103,104], angularly-tuned [52,105] or linear variable [106] thin film filters, and volume Bragg grating filters [86]. It can be compensated by scanning the calibrated filter over some range of wavelengths around the desired wavelength, and then performing a software correction to produce an image that is centered at a single common wavelength over the entire field of view in the image plane [50]. For smaller fields of view and moderate resolving powers, as considered here, it is possible to neglect these effects, similar to operating in the so-called 'Jacquinot-spot' region for a Fabry-Perot filter [104].

4.3.2 Hyperspectral imaging results

For proof-of-principle experiments, the imaging system described above was augmented by an infinity-corrected objective lens (Zeiss 5x with F_{OBJ} = 33 mm and pupil diameter 4 mm) at the input, and a TV-lens (F_{TV} = 25 mm, focused at ~infinity) coupled to a consumer-grade silicon CMOS camera (Thorlabs DCC 1645-C or DCC 1545-M) at the output. An adjustable iris was placed after the objective in order to further reduce the input pupil size (see Figure 4.6(b)), and it was set to ~ 3 mm for the results below. The overall system magnification ($M \approx F_{TV}/F_{OBJ}$) was close to unity. A dark-field object was implemented by coupling LEDs of various colors into a 1-to-4 fan-out fiber bundle (Thorlabs BF42LS01). The individual fibers in this bundle have nominally 200 μm core diameter and 225 μm cladding outer diameter.

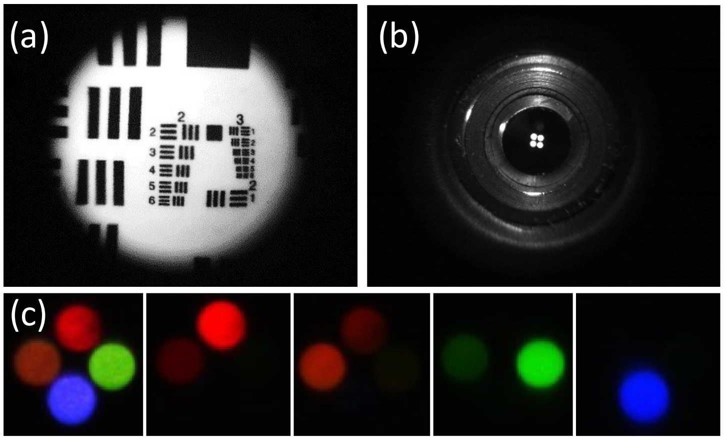

Figure 4.7 (a) Bright-field image of a USAF resolution target captured by the monochrome camera. (b) Image of the fiber bundle end facet captured with the monochrome camera. Both were captured with the ball filter at normal incidence. (c) A series of images of the facet of a 4-fiber bundle (see main text) coupled by LEDs of different colors. The first image was captured with the air gap at roughly normal incidence. The remaining images were captured at various settings in the tunneling regime, with angle increasing towards the right. Note that the white LED (left) has significant spectral content in both the green and red parts of the spectrum.

Acceptable imaging quality was achieved with only minimal efforts to optimize alignment and without any supplemental stops in the optical path, aside from the adjustable aperture of the TV lens. A typical bright-field image of a standard 1951 USAF resolution target, with the ball filter rotated to near-normal incidence (i.e. in the non-tunneling regime, where it transmits over the entire visible range), is shown in Figure 4.7(a). Resolution at 14 lp/mm (Group 3, element 6) or better was verified for central regions of the image, although residual aberrations and distortions are apparent near the peripheries. As shown in Figure 4.7(b), the fiber cores, and the ~25 μm spaces between them, were well-resolved. Very slight defocusing and glare were evident in some dark-field images, possibly including slight comatic effects at the higher-angle (green and blue) settings of the filter. This might be caused in part by imperfect centering of the optical system [107]. A more in-depth optimization, possibly including the addition of compensating lenses and stops, is the subject of ongoing study.

For illustration purposes Figure 4.7(c) shows a sequence of images captured by a color camera and with white, red, green, and blue LEDs coupled into individual fibers. The left-most image was captured in the non-tunneling regime, where the transmission is relatively flat over the entire visible range. The subsequent images were captured at a series of settings (increasing angle and reducing air gap, see Section 4.2) in the tunneling regime, chosen to selectively pass light from a particular LED or LEDs while blocking light from the others. The white LED (bottom left) is visible in the 3rd and 4th images, but has lower power spectral density than the red and green LEDs at these settings. The increased spectral purity of the filtered light is particularly evident for the green and blue LEDs (4th and 5th images, respectively).

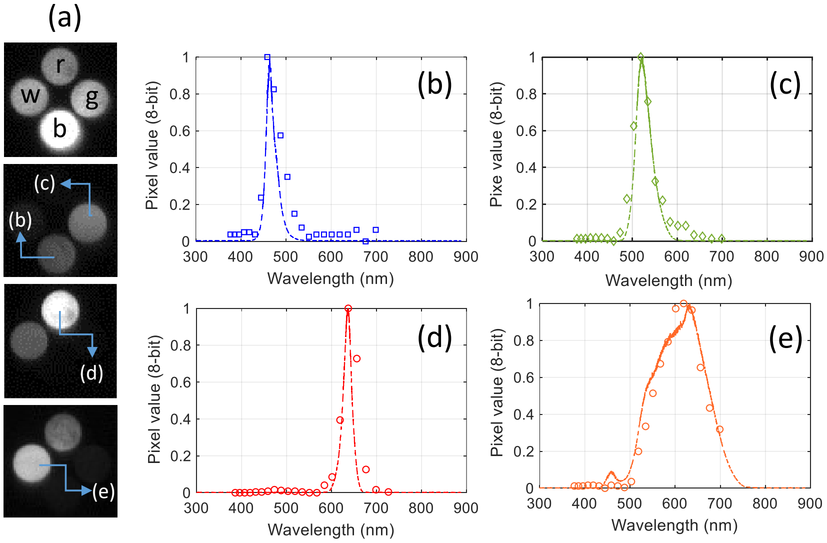

Figure 4.8 (a) Top picture is a monochrome camera image of the 4-fiber bundle captured at normal incidence on the air gap. Remaining pictures are representative images captured at various settings in the tunneling regime. (b) Extracted raw spectrum (symbols) for pixels within the blue fiber core, compared to reference spectra from a commercial spectrometer (dashed line). (c-e) As in part (b), but for the green, red and white LEDs, respectively.

To demonstrate hyperspectral imaging, the color camera was replaced by a monochrome camera, and data cubes were obtained by recording pixel intensity values at a series of tunable filter settings. Figure 4.8(a) shows a sequence of images captured at various settings of the filter. Raw spectra were extracted for individual pixels within the portion of the image corresponding to individual fiber cores. Pixel values were plotted versus the wavelength setting of the ball filter, using calibration curves determined from measurements such as described in Section 4.2.

As shown in Figure 4.8(b-e), the extracted spectra are in good agreement with those measured using a commercial spectrometer (Ocean Optics USB4000 with resolution ~ 7 nm). Notably, the extracted spectra represent raw data, in that they were not calibrated for variations in quantum efficiency of the CMOS camera or for variations in the optical throughput (including the insertion loss of the ball filter). For the white LED, the noisy part of the reference spectrum near 600 nm is an artifact of the order blocking filter in the commercial spectrometer. The spectrum extracted by the imaging setup is actually closer in shape to the curve supplied by the LED manufacturer (Everlight 334-15/X2C1-1SUA). For the single-color LEDs, the passband resolution (~ 4-10 nm, see Figure 4.4) of the ball filter results in some broadening of the extracted spectra. In spite of these slight inconsistencies, the results are encouraging for a first-generation prototype, especially given the challenges with manual assembly and alignment mentioned above.

4.4 Summary and conclusions

We described a novel type of widely tunable filter, with imaging capabilities, based on resonant optical tunneling through an adjustable air gap between two thin-film-coated half-ball lenses. Filters that can be tuned over the visible and NIR ranges were designed, fabricated, and experimentally verified. We showed that they have potential as a relatively compact fiber-coupled spectrometer technology, providing good compatibility with the numerical aperture and étendue of standard optical fibers. Moreover, they could potentially enable a new class of hyperspectral imaging systems. The imaging system described here measures only a few square centimeters in size and could fit easily into the optical path of a fluorescence microscope, for example [52]. With the addition of software calibration routines, and in some cases with the use of larger lenses, the concept might have potential to also address other hyperspectral imaging applications.

Many tunable filter technologies have been used or proposed for hyperspectral imaging [2,96], each having strengths and weaknesses. Perhaps the most conceptually similar approach to ours is the conventional air-gap Fabry-Perot interferometer [103,104], which recently has been miniaturized using MEMS technology [96,108]. Compared to Fabry-Perot filters, the tunneling filter offers some advantages, however, including its relatively simple thin-film stack, its inherently flat-top passband shape [5], its ability to strongly reject out-of-band light over a wide blocking range (i.e. no free-spectral-range limitations), and (at least for some applications) its simultaneous function as a broadband polarizer. Conceivably, these properties could allow broadband operation without the need for supplemental filters. Furthermore, we have shown previously [79] that there is potential to implement versions of the tunneling filter that provide greatly increased resolving power and out-of-band rejection.

An undeniable challenge is presented by the high angular dependence of the passband center wavelength, which is approximately 10-15 nm/degree for the visible-range filter. In this respect, and in terms of its other performance characteristics (out-of-band blocking, operational tuning ranges for a single part, etc.), VBG imaging filters [50,86] likely provide the best comparable. VBG filters are relatively, although not completely, polarization independent, which provides a throughput advantage. However, to cover the operational ranges demonstrated by the individual tunneling filters described here, VBG-based systems [47] and conventional angularly tuned thin-film-filter systems [7,52] typically require multiple gratings or filters on a turret. Given its attributes, the resonant tunneling filter might be a simpler and lower-cost solution for some applications, provided practical difficulties with respect to assembly, alignment and image aberrations are addressed. We hope to explore these improvements in future work.

Chapter 5 Summary and future work

5.1 Summary

The work contained in this thesis focused on the development of a broadband tunable filter based on resonant optical tunneling through an embedded air gap layer. When appropriately situated within surrounding phase-matching and admittance-matching dielectric layers, a narrow, flat-top passband is produced with excellent out of band rejection and blocking range. This passband, when designed for one polarization state, strongly rejects orthogonal polarizations. However, in contrast to the static filter reported previously [5], the filters produced in this work can be tuned over a broad wavelength range through rotation of the angle of incidence and actuation of the air gap thickness.

In Chapter 3, the theory for the analytical design of such tunable filters was expanded from prior work. A first-generation tunable filter prototype based on hemi-cylindrical lenses was fabricated for testing using 4-layer a-Si/SiO_2 admittance matching stacks designed to produce a flat-top passband centered at 1550 nm for an incident angle ~ 45°. These stacks were sputtered directly onto the rectangular face of these hemi-cylindrical lenses. Then, the two lenses were clamped with the deposited films in nominal contact, and piezo stack actuators were glued in place. After removing the clamps, the filter was complete and could be tested. During testing, a matched pair of collimators and diverging lenses were used to deliver fiber-to-fiber coupling, while compensating for the curved surfaces of the assembled filter. Angle tuning and airgap tuning were used to produce a variety of different passbands spanning the range from ~ 1100 – 1700 nm. Theory predicted a tunable range from ~ 1000 – 1800 nm. However, an estimated “resting point” air gap of ~ 1.8 μm prevented the observation of passbands with center wavelength < 1100 nm while the range of the optical spectrum analyzer used prevented observation of passbands with center wavelength > 1700 nm.

Experimental passband characteristics such as out of band rejection (~OD6 at ± 100 nm) as well as the angles and air gaps required to produce flat-top passbands agreed closely with theory. Meanwhile, typical bandwidths were observed to be ~ 40 – 50 % wider than predicted. Likely causes of these broader passbands include imperfect collimation of the beam at the air gap (angular convolution), as well as non-uniformities in the air gap width and matching stack thin film thicknesses (spatial convolution). Regardless, these filter characteristics compared favorably to current commercial solutions such as volume Bragg grating [46], acousto-optic [36], liquid-crystal [30], and angle-tuned tunable filters [6].

A new version of this NIR filter was fabricated in Chapter 4 using 10 mm diameter hemi-spherical lenses to simplify fiber to fiber coupling and enable the tunneling filter to be used in a hyperspectral imaging apparatus. The transition to spherical coupling prisms necessitated the design of a jig in which to hold the prisms and the piezo actuators, but direct fiber-to-fiber coupling could occur using the filter ball as a coupling lens. Similar passband characteristics were observed to the cylindrical filter case, while fiber to fiber coupling efficiency was improved by ~ 2 dB despite there being no anti-reflection coatings used in the optical path. Additionally, improved assembly reduced the resting point air gap such that the full designed range of the filter could be accessed. The spherical NIR filter utilized the same admittance matching stacks used previously, however, a spherical visible range filter was also produced using an 8-layer matching stack based on Ta_2O_5/SiO_2 layers and designed to produce a passband at 650 nm and 45°. The out of band and polarization rejection of this VIS filter were predicted to be inferior to the NIR case, owing to the lower refractive index contrast of the materials used. Near the center of the tunable range, out-of-band rejection was still predicted to reach ~ OD6, but due to a limited dynamic range in the experimental setup, such rejection characteristics could not be verified. Passbands for the visible filter were observed from ~ 460 – 750 nm, indicating a resting air gap ~ 0.6 µm, while passband widths were approximately twice what theory predicted (~ 4 – 10 nm) owing to similar angular and spatial convolution effects as the cylindrical NIR filter. Thus, a wavelength calibration curve for corresponding angle and air gap was compiled for this filter.

In addition to testing direct fiber-to-fiber coupling, an imaging apparatus was constructed. This apparatus consisted of placing the filter ball between a pair of longer focal length achromat lenses. Thus, collimated input, such as from an infinity corrected microscope objective, is focused by the achromats to be collimated at the air gap by the spherical surface of the ball lens. Initial testing with this imaging setup consisted of fiber collimators at input and output to corroborate the fiber-to-fiber calibration data. Eventually these collimators were replaced by a 5x objective and a consumer grade camera with a TV lens focused at ~ infinity to create a hyperspectral imaging system. For the VIS filter, ray-tracing simulations were used to predict the optimal lens spacings for beam collimation at the air gap and collimation at the front surface of the camera lens. Then, a brightfield 1951 USAF imaging test target was used to confirm and adjust these spacings to remove aberration in the imaging system. A dark field target with a variety of spectral content, consisting of 4 colored LEDs (red, white, green, and blue) coupled through a 1 – 4 fiber fan out bundle was constructed. This target was then imaged through the tunable filter and image cubes were assembled. By tracking single pixel intensities within these image cubes and utilizing the wavelength calibration curve for the filter, the spectral characteristics of those LEDs located within each image were extracted. Comparison of these spectral curves to those obtained for the LEDs on a commercial spectrometer showed good agreement, with the imaging system obtaining curves slightly wider than the spectrometer.

5.2 Future work

With the successful demonstration of these tunable filter prototypes, future work might include producing filters with more periods in the admittance matching stacks. Provided extremely well collimated light and high symmetry in the matching stacks can be achieved, passbands with out of band rejection >OD10 and extremely narrow linewidths (see Figure 3.2(c)) might be possible. Such characteristics could make these filters attractive for use in quantum optics [109,110], or wavelength division multiplexing applications [11] where the narrow bandwidth requirements are outside the scope of the current filters. To meet the high symmetry requirements for the matching stacks, more uniform and more precisely controlled deposition methods could be used. Examples of improved deposition methods include computer controlled sputtering systems with more complex substrate rotation mechanisms [111,112] and *in situ* monitoring of film thickness, or plasma enhanced chemical vapor deposition [113]. In order to improve collimation at the air gap, supplementary lenses can be used such as in Chapter 4, with further adjustments made to the lens system based on more comprehensive ray-tracing simulations.

The manual assembly method of the filter system from the constituent ball lenses and associated parts is another suspected cause of coupling inefficiencies and passband broadening, due to the potential for misalignment. Non-concentric placement of the hemi-spherical lenses would make the resulting assembly slightly aspheric, increasing scattering losses and beam walk-off as the filter is rotated. The result is likely a filter with increased insertion loss and in particular, an increased change in insertion loss with tuning. Co-planarity at the air gap between the flat surfaces of the lenses is likely another source of passband broadening in filters assembled to date. With non-coplanar surfaces, the air gap takes a wedge shape. Hence, different sections of the beam see slightly different angles and the passband is broadened accordingly. Future improvements of the jig designed to hold the hemi-spherical lenses, especially with an aim towards improving the concentricity, could include using parts machined to higher tolerances, mechanized assembly using pick-and-place type machinery and machine vision [114], as well as larger jigs with larger lenses so that the relative impact of non-concentricity is minimized. As the original parts of the jig were machined out of aluminum, the use of a sturdier metal such as stainless steel could improve the co-planarity of the hemi-spheres, since the clamping force applied during assembly would be less likely to distort the machined parts and cause the lenses to lose their nominal contact during assembly.

With regards to the hyperspectral imaging system designed in Section 4.3, improvements can conceivably be made in elements of the optical path to correct for the spherical aberration caused by the filter. This could include simply using larger hemi-spherical coupling prisms, or through the use of supplementary optics. Of interest, during the normal incidence optimization of the imaging system, placing the filter ball further away from the input achromat lens and closer to the output achromat appeared to remove the spherical aberration almost completely. However, the ray angle at the air gap was no longer optimally collimated under these conditions, leading to passband broadening. This led to the conclusion that the introduction of additional compensating lenses after the ball filter should be able to perform a similar aberration–compensating function, while maintaining the necessary collimation at the air gap. Such a broadly tunable hyperspectral imaging system with very high image quality might be very attractive compared to alternative tunable filter solutions.

References

1. H. Kobrinski and K. W. Cheung, "Wavelength-Tunable Optical Filters: Applications and Technologies," IEEE Commun. Mag. **27**(10), 53–63 (1989).
2. N. Gat, "Imaging spectroscopy using tunable filters: a review," in *Wavelet Applications VII* (SPIE, 2000), **4056**, pp. 50–64.
3. P. Favreau, C. Hernandez, A. S. Lindsey, D. F. Alvarez, T. Rich, P. Prabhat, and S. J. Leavesley, "Thin-film tunable filters for hyperspectral fluorescence microscopy," J. Biomed. Opt. **19**(1), 011017 (2013).
4. A. P. Levick, C. L. Greenwell, J. Ireland, E. R. Woolliams, T. M. Goodman, A. Bialek, and N. P. Fox, "Spectral radiance source based on supercontinuum laser and wavelength tunable bandpass filter: the spectrally tunable absolute irradiance and radiance source," Appl. Opt. **53**(16), 3508 (2014).
5. A. Melnyk, M. H. Bitarafan, T. W. Allen, and R. G. DeCorby, "Air gap resonant tunneling bandpass filter and polarizer," Opt. Lett. **41**(8), 1845 (2016).
6. T. Erdogan and L. Wang, "Semrock VersaChrome - the First Widely Tunable Thin-film Optical Filters," 1–15 (2010).
7. G. Hennig, G. M. Brittenham, R. Sroka, G. Kniebühler, M. Vogeser, and H. Stepp, "Bandwidth-variable tunable optical filter unit for illumination and spectral imaging systems using thin-film optical band-pass filters," Rev. Sci. Instrum. **84**(4), (2013).
8. J. Lumeau, F. Lemarchand, T. Begou, D. Arhilger, and H. Hagedorn, "Angularly tunable bandpass filter: design, fabrication, and characterization," Opt. Lett. **44**(7), 1829 (2019).
9. S. Isaacs, F. Placido, and I. Abdulhalim, "Investigation of liquid crystal Fabry–Perot tunable filters: design, fabrication, and polarization independence," Appl. Opt. **53**(29), H91 (2014).
10. S. R. Mallinson, "Wavelength-selective filters for single-mode fiber WDM systems using Fabry-Perot interferometers," Appl. Opt. **26**(3), 430 (1987).
11. D. Sadot and E. Boimovich, "Tunable Optical Filters for Dense WDM Networks," IEEE Commun. Mag. **36**(12), 50–55 (1998).
12. A. T. T. D. Tran, Y. H. Lo, Z. H. Zhu, D. Haronian, and E. Mozdy, "Surface micromachined fabry-perot tunable filter," IEEE Photonics Technol. Lett. **8**(3), 393–395 (1996).

13. J. S. Milne, J. M. Dell, A. J. Keating, and L. Faraone, "Widely tunable MEMS-based fabry - Perot filter," J. Microelectromechanical Syst. **18**(4), 905–913 (2009).

14. H. Omran, Y. M. Sabry, M. Sadek, K. Hassan, M. Y. Shalaby, and D. Khalil, "Deeply-etched optical MEMS tunable filter for swept laser source applications," IEEE Photonics Technol. Lett. **26**(1), 37–39 (2014).

15. P. A. Stupar, R. L. Borwick, J. F. DeNatale, P. H. Kobrin, and W. J. Gunning, "MEMS tunable Fabry-Perot filters with thick, two sided optical coatings," TRANSDUCERS 2009 - 15th Int. Conf. Solid-State Sensors, Actuators Microsystems 1357–1360 (2009).

16. P. Yeh, *Optical Waves in Layered Media (Wiley Series in Pure and Applied Optics)* (Wiley-Interscience, 2005).

17. H. A. Macleod, *Thin-Film Optical Filters*, 4th ed. (IOP Publishing Ltd, 1986), **2nd**.

18. Y. Suemura, A. Tajima, N. Henmi, H. Morimura, and H. Takahashi, "An adaptive wavelength tunable optical filter employing an angle-tuned interference filter and an intelligent digital controller," J. Light. Technol. **14**(6), 1048–1055 (1996).

19. N. P. Ayerden, G. de Graaf, and R. F. Wolffenbuttel, "Compact gas cell integrated with a linear variable optical filter," Opt. Express **24**(3), 2981 (2016).

20. M. Lequime, "Tunable thin film filters: review and perspectives," Adv. Opt. Thin Film. **5250**(February 2004), 302 (2004).

21. A. Piegari, J. Bulir, and A. K. Sytchkova, "Variable narrow-band transmission filters for spectrometry from space. 2. Fabrication process," Appl. Opt. **47**(13), 151–156 (2008).

22. A. Emadi, H. Wu, S. Grabarnik, G. De Graaf, and R. F. Wolffenbuttel, "Vertically tapered layers for optical applications fabricated using resist reflow," J. Micromechanics Microengineering **19**(7), (2009).

23. A. Emadi, H. Wu, S. Grabarnik, G. De Graaf, K. Hedsten, P. Enoksson, J. H. Correia, and R. F. Wolffenbuttel, "Fabrication and characterization of IC-Compatible Linear Variable Optical Filters with application in a micro-spectrometer," Sensors Actuators, A Phys. **162**(2), 400–405 (2010).

24. C. Williams, G. Rughoobur, A. J. Flewitt, and T. D. Wilkinson, "Single-step fabrication of thin-film linear variable bandpass filters based on metal–insulator–metal geometry," Appl. Opt. **55**(32), 9237 (2016).

25. P. Ji, C.-S. Park, S. Gao, S.-S. Lee, and D.-Y. Choi, "Angle-tolerant linear variable color

filter based on a tapered etalon," Opt. Express **25**(3), 2153 (2017).

26. "Santec OTF-930," https://www.santec.com/en/products/instruments/tunablefilter/otf-930.

27. "Delta optical thin film: Continuously Variable Filters (A.K.A. Linear Variable Filters)," https://www.deltaopticalthinfilm.com/products-old/linear-variable-filters/.

28. G. Di Caprio, D. Schaak, and E. Schonbrun, "Hyperspectral fluorescence microfluidic (HFM) microscopy," Biomed. Opt. Express **4**(8), 1486 (2013).

29. N. Tack, A. Lambrechts, P. Soussan, and L. Haspeslagh, "A compact, high-speed, and low-cost hyperspectral imager," Silicon Photonics VII **8266**(February 2012), 82660Q (2012).

30. O. Aharon and I. Abdulhalim, "Liquid crystal Lyot tunable filter with extended free spectral range," Opt. Express **17**(14), 11426 (2009).

31. A. Sneh and K. M. Johnson, "High-speed continuously tunable liquid crystal filter for WDM networks," J. Light. Technol. **14**(6), 1067–1080 (1996).

32. H. J. Masterson, G. D. Sharp, and K. M. Johnson, "Ferroelectric liquid-crystal tunable filter," Opt. Lett. **14**(22), 1249 (1989).

33. T. Yano and A. Watanabe, "New noncollinear acousto-optic tunable filter using birefringence in paratellurite," Appl. Phys. Lett. **24**(6), 256–258 (1974).

34. S. E. Harris and R. W. Wallace, "Acousto-Optic Tunable Filter*," J. Opt. Soc. Am. **59**(6), 744 (1969).

35. D. A. Smith and J. J. Johnson, "Switching speed of integrated acoustically-tunable optical filter," Electron. Lett. **27**(23), 2102–2103 (1991).

36. L. Bei, G. I. Dennis, H. M. Miller, T. W. Spaine, and J. W. Carnahan, "Acousto-optic tunable filters: fundamentals and applications as applied to chemical analysis techniques," Prog. Quantum Electron. **28**(2), 67–87 (2004).

37. H. R. Morris, C. C. Hoyt, and P. J. Treado, "Imaging Spectrometers for Fluorescence and Raman Microscopy: Acousto-Optic and Liquid Crystal Tunable Filters," Appl. Spectrosc. **48**(7), 857–866 (1994).

38. D. N. Stratis, K. L. Eland, J. C. Carter, S. J. Tomlinson, and S. M. Angel, "Comparison of acousto-optic and liquid crystal tunable filters for laser-induced breakdown spectroscopy," Appl. Spectrosc. **55**(8), 999–1004 (2001).

39. D. A. Smith, J. E. Baran, J. J. Johnson, and K.-W. Cheung, "Integrated-Optic Acoustically-Tunable Filters for WDM Networks," IEEE J. Sel. Areas Commun. **8**(6), (1990).

40. D. Östling and H. E. Engan, "Narrow-band acousto-optic tunable filtering in a two-mode fiber," Opt. Lett. **20**(11), 1247 (1995).

41. K. Takabayashi, K. Takada, N. Hashimoto, M. Doi, S. Tomabechi, T. Nakazawa, and K. Morito, "Widely (132 nm) wavelength tunable laser using a semiconductor optical amplifier and an acousto-optic tunable filter," Electron. Lett. **40**(19), 1187 (2004).

42. M. Volanthen, H. Geiger, M. G. Xu, and J. P. Dakin, "Simultaneous monitoring of multiple fibre gratings with a single acousto-optic tunable filter," Electron. Lett. **32**(13), 1228–1229 (1996).

43. M. G. Xu, H. Geiger, and J. P. Dakin, "Modeling and performance analysis of a fiber bragg grating interrogation system using an acousto-optic tunable filter," J. Light. Technol. **14**(3), 391–396 (1996).

44. O. M. Efimov, L. B. Glebov, and H. P. Andre, "Measurement of the induced refractive index in a photothermorefractive glass by a liquid-cell shearing interferometer," Appl. Opt. **41**(10), 1864 (2002).

45. S. Blais-Ouellette, "Method and apparatus for a Bragg grating tunable filter," U.S. patent US007557990B2 (2005).

46. B. Y. D. Gagnon and L.-I. Dion-Bertrand, "White Paper Widely Tunable Filter Technology & Measurement," 1–12 (2015).

47. K. Maham, A. Vaskuri, F. Manoocheri, and E. Ikonen, "Calibration of Near-Infrared Detectors Using a Wavelength Tunable Light Source," Opt. Rev. **27**(2), 183–189 (2020).

48. "Photon Etc. Laser Line Tunable Filter," http://www.photonetc.com/laser-line-tunable-filter.

49. S. Hengesbach, N. Krauch, C. Holly, M. Traub, U. Witte, and D. Hoffmann, "High-power dense wavelength division multiplexing of multimode diode laser radiation based on volume Bragg gratings," Opt. Lett. **38**(16), 3154 (2013).

50. E. Gaufrès, S. Marcet, V. Aymong, N. Y. W. Tang, A. Favron, F. Thouin, C. Allard, D. Rioux, N. Cottenye, M. Verhaegen, and R. Martel, "Hyperspectral Raman imaging using Bragg tunable filters of graphene and other low-dimensional materials," J. Raman

Spectrosc. **49**(1), 174–182 (2018).

51. "Micron Optics Fiber Fabry-Perot Tunable Filter," http://www.micronoptics.com/product/fiber-fabry-perot-tunable-filter-ffp-tf/.

52. P. F. Favreau, C. Hernandez, T. Heaster, D. F. Alvarez, T. C. Rich, P. Prabhat, and S. J. Leavesley, "Excitation-scanning hyperspectral imaging microscope," J. Biomed. Opt. **19**(4), 046010 (2014).

53. "Semrock 2019 Master Catalog," https://www.semrock.com/Data/Sites/1/semrockpdfs/SemrockCatalog-2019.pdf.

54. N. Gupta and V. Voloshinov, "Hyperspectral imager, from ultraviolet to visible, with a KDP acousto-optic tunable filter," Appl. Opt. **43**(13), 2752–2759 (2004).

55. S. O. Kasap, *Optoelectronics and Photonics: Principles and Practices*, Second (Pearson Education Inc., 2001).

56. J. Stone, L. W. Stulz, C. A. Burrus, and J. C. Centanni, "F:End filters: etalon on the beveled facet of a fiber with an outdiffused core," IEEE Photonics Technol. Lett. **3**(3), 216–218 (1991).

57. M. S. O'Sullivan, E. Desurvire, J. R. Simpson, and J. Chrostowski, "High-power narrow-linewidth Er^3+-doped fiber laser," Opt. Lett. **14**(9), 438 (1989).

58. J. A. Dobrowolski, "Mica Interference Filters with Transmission Bands of Very Narrow Half-Widths*," J. Opt. Soc. Am. **49**(8), 794 (1959).

59. R. R. Austin, "The Use of Solid Etalon Devices as Narrow Band Interference Filters," Opt. Eng. **11**(3), (1972).

60. D. M. Beggs, M. A. Kaliteevski, S. Brand, and R. A. Abram, "Optimization of an optical filter with a square-shaped passband based on coupled microcavities," J. Mod. Opt. **51**(3), 437–446 (2004).

61. S. D. Smith, "Design of Multilayer Filters by Considering Two Effective Interfaces," J. Opt. Soc. Am. **48**(1), 43 (1958).

62. T. W. Allen and R. G. DeCorby, "Conditions for admittance-matched tunneling through symmetric metal-dielectric stacks," Opt. Express **20**(S5), A578 (2012).

63. P. H. Berning and A. F. Turner, "Induced Transmission in Absorbing Films Applied to Band Pass Filter Design," J. Opt. Soc. Am. **47**(3), 230 (1957).

64. T. W. Allen and R. G. DeCorby, "Assessing the maximum transmittance of periodic metal-dielectric multilayers," J. Opt. Soc. Am. B **28**(10), 2529 (2011).

65. P. H. Lissberger, "Coatings with induced transmission," Appl. Opt. **20**(1), 95 (1981).

66. B. V. Landau and P. H. Lissberger, "Theory of induced-transmission filters in terms of the concept of equivalent layers," J Opt Soc Am **62**(11), 1258–1264 (1972).

67. S. W. Teare, *Optical Interference Filters Using MATLAB* (SPIE, 2019).

68. P. W. Baumeister, "Optical Tunneling and Its Applications to Optical Filters," Appl. Opt. **6**(5), 897 (1967).

69. A. E. Gee and H. D. Polster, "A Method for Measuring Extremely Small Non-Uniformities in the Optical Thickness of Evaporated Films," J. Opt. Soc. Am. **39**(12), 1044 (1949).

70. D. T. F. Marple, "Refractive index of ZnSe, ZnTe, and CdTe," J. Appl. Phys. **35**(3), 539–542 (1964).

71. R. P. Netterfield, "Refractive indices of zinc sulfide and cryolite in multilayer stacks," Appl. Opt. **15**(8), 1969 (1976).

72. M. Scalora, M. J. Bloemer, A. S. Pethel, J. P. Dowling, C. M. Bowden, and A. S. Manka, "Transparent, metallo-dielectric, one-dimensional, photonic band-gap structures," J. Appl. Phys. **83**(5), 2377–2383 (1998).

73. R. J. Holloway and P. H. Lissberger, "The Design and Preparation of Induced Transmission Filters," Appl. Opt. **8**(3), 653 (1969).

74. L. Li and J. A. Dobrowolski, "Optical coatings with an integral FTIR air layer," Opt. Express **18**(4), 3784 (2010).

75. H. A. Macleod, "A new approach to the design of metal–dielectric thin-film optical coatings," Opt. Acta (Lond). **25**(2), 93–106 (1978).

76. S. Brand, R. A. Abram, and M. A. Kaliteevski, "Evanescently coupled interface states in the gap between two Bragg reflectors," Opt. Lett. **35**(12), 2085 (2010).

77. G. H. Cross and S. Brand, "Wavelength-dependent frustrated internal reflection via photonic interface states," Appl. Phys. Lett. **99**(19), (2011).

78. P. Yeh, A. Yariv, and C.-S. Hong, "Electromagnetic propagation in periodic stratified media I General theory*," J. Opt. Soc. Am. **67**(4), 423 (1977).

79. T. R. Harrison, G. J. Hornig, C. Huang, L. Bu, T. Haluza-Delay, K. Scheuer, and R. G.

DeCorby, "Widely tunable bandpass filter based on resonant optical tunneling," Opt. Express **27**(16), 23633 (2019).

80. "Tunable filters, (EXFO Inc., 2019)," https://www.exfo.com/en/products/lab-manufacturing-testing/tunable-filters/.

81. C. J. van der Laan and H. J. Frankena, "Equivalent layers: another way to look at them," Appl. Opt. **34**(4), 681 (1995).

82. D. F. P. Pile, "Gap modes of one-dimensional photonic crystal surface waves," Appl. Opt. **44**(20), 4398–4401 (2005).

83. S. Al-Sumaidae, M. H. Bitarafan, C. A. Potts, J. P. Davis, and R. G. DeCorby, "Cooperativity enhancement in buckled-dome microcavities with omnidirectional claddings," Opt. Express **26**(9), 11201 (2018).

84. G. Cocorullo, F. G. Della Corte, I. Rendina, C. Minarini, A. Rubino, and E. Terzini, "Amorphous silicon waveguides and light modulators for integrated photonics realized by low-temperature plasma-enhanced chemical-vapor deposition," Opt. Lett. **21**(24), 2002 (1996).

85. I. J. Arnold, H. Moosmüller, N. Sharma, and C. Mazzoleni, "Beam characteristics of fiber-based supercontinuum light sources with mirror- and lens-based beam collimators," Opt. Express **22**(11), 13860 (2014).

86. M. Paillet, F. Meunier, M. Verhaegen, Ś. Blais-Ouellette, and R. Martel, "High performance resonance Raman spectroscopy using volume Bragg gratings as tunable light filters," Rev. Sci. Instrum. **81**(5), (2010).

87. "Piezoelectric Tutorial," https://www.thorlabs.com/newgrouppage9.cfm?objectgroup_id=5030.

88. A. Q. Jian and X. M. Zhang, "Resonant optical tunneling effect: Recent progress in modeling and applications," IEEE J. Sel. Top. Quantum Electron. **19**(3), (2013).

89. C. Poudel and C. F. Kaminski, "Supercontinuum radiation in fluorescence microscopy and biomedical imaging applications," J. Opt. Soc. Am. B **36**(2), A139 (2019).

90. J. T. Woodward, A. W. Smith, C. A. Jenkins, C. Lin, S. W. Brown, and K. R. Lykke, "Supercontinuum sources for metrology," Metrologia **46**(4), (2009).

91. M. Manley, "Near-infrared spectroscopy and hyperspectral imaging: Non-destructive analysis of biological materials," Chem. Soc. Rev. **43**(24), 8200–8214 (2014).

92. B. Boldrini, W. Kessler, K. Rebner, and R. Kessler, "Hyperspectral imaging: a review of best practice, performance and pitfalls for inline and online applications," J. Near Infrared Spectrosc. **20**(5), 438 (2012).

93. G. Lu and B. Fei, "Medical hyperspectral imaging: a review," J. Biomed. Opt. **19**(1), 010901 (2014).

94. J. Shiefman, "Insertion loss comparison of microcollimators used to propagate light in and out of single-mode fibers," Opt. Eng. **43**(8), 1927 (2004).

95. S. D. Alaruri, "Single-mode fiber-to-single-mode fiber coupling efficiency and tolerance analysis: Comparative study for ball, conic and GRIN rod lens coupling schemes using Zemax Huygen's integration and physical optics calculations," Optik (Stuttg). **126**(24), 5923–5927 (2015).

96. R. A. Crocombe, "Portable Spectroscopy," Appl. Spectrosc. **72**(12), 1701–1751 (2018).

97. M. S. Faraji-Dana, E. Arbabi, A. Arbabi, S. M. Kamali, H. Kwon, and A. Faraon, "Compact folded metasurface spectrometer," Nat. Commun. **9**(1), (2018).

98. E. Ye, A. H. Atabaki, N. Han, and R. J. Ram, "Miniature, sub-nanometer resolution Talbot spectrometer," Opt. Lett. **41**(11), 2434 (2016).

99. H. A. Elagha, "Ray tracing in monocentric and ball lenses by a general exact formula," J. Opt. Soc. Am. A **36**(7), 1117 (2019).

100. O. S. Cossairt, D. Miau, and S. K. Nayar, "Scaling law for computational imaging using spherical optics," J. Opt. Soc. Am. A **28**(12), 2540 (2011).

101. W. Pang and D. J. Brady, "Field of view in monocentric multiscale cameras," Appl. Opt. **57**(24), 6999 (2018).

102. J. Ai, J. Popelek, Y. Li, and R. T. Chen, "Beam-splitting ball lens:?a new integrated optical component," Opt. Lett. **24**(21), 1478 (1999).

103. M. Strauch, I. L. Livshits, F. Bociort, and H. P. Urbach, "Wide-angle spectral imaging using a Fabry-Pérot interferometer," J. Eur. Opt. Soc. **10**, 1–7 (2015).

104. D. H. Jones, P. L. Shopbell, and J. Bland-Hawthorn, "Detection and measurement from narrow-band tunable filter scans," Mon. Not. R. Astron. Soc. **329**(4), 759–774 (2002).

105. T. Goossens, B. Geelen, J. Pichette, A. Lambrechts, and C. Van Hoof, "Finite aperture correction for spectral cameras with integrated thin-film Fabry–Perot filters," Appl. Opt.

57(26), 7539 (2018).

106. I. G. E. Renhorn and L. Axelsson, "High spatial resolution hyperspectral camera based on exponentially variable filter," Opt. Eng. **58**(10), 1 (2019).

107. E. Hecht, *Optics*, 4th ed. (Addison-Wesley, 2002).

108. A. Rissanen, B. Guo, H. Saari, A. Näsilä, R. Mannila, A. Akujärvi, and H. Ojanen, "VTT's Fabry-Perot interferometer technologies for hyperspectral imaging and mobile sensing applications," MOEMS Miniaturized Syst. XVI **10116**(May), 101160I (2017).

109. P. Palittapongarnpim, A. MacRae, and A. I. Lvovsky, "Note: A monolithic filter cavity for experiments in quantum optics," Rev. Sci. Instrum. **83**(6), 2010–2013 (2012).

110. A. Ahlrichs, C. Berkemeier, B. Sprenger, and O. Benson, "A monolithic polarization-independent frequency-filter system for filtering of photon pairs," Appl. Phys. Lett. **103**(24), (2013).

111. M. Gross, S. Dligatch, and A. Chtanov, "Optimization of coating uniformity in an ion beam sputtering system using a modified planetary rotation method," Opt. InfoBase Conf. Pap. 5–9 (2010).

112. C. Fu, C. Yang, L. Han, and H. Chen, "The thickness uniformity of films deposited by magnetron sputtering with rotation and revolution," Surf. Coatings Technol. **200**(12–13), 3687–3689 (2006).

113. J. Kuske, U. Stephan, W. Nowak, S. Roehlecke, and A. Kottwitz, "Deposition conditions for large area PECVD of amorphous silicon," Mater. Res. Soc. Symp. - Proc. **467**(May), 591–595 (1997).

114. J. P. Spallas, C. S. Silver, L. P. Muray, T. Wells, and M. El-Gomati, "A manufacturable miniature electron beam column," Microelectron. Eng. **83**(4-9 SPEC. ISS.), 984–989 (2006).

Appendix A: Fabrication parameters and deposition jig drawings

This appendix contains information on the fabrication of the cylindrical and spherical filter systems, including technical drawings for the requisite deposition and clamping jigs. Fabrication of the above devices was done by depositing thin films directly onto the flat surfaces of hemi-cylindrical and later hemi-spherical lenses (using the custom jigs described below) in the nanoFAB's Doug Sputtering System #2. Metal surfaces that would touch the lenses were coated with Kapton tape prior to loading the lenses to prevent scratches. Additionally, all lenses were cleaned using Piranha prior to deposition. The deposition jigs were designed to be modular utilizing the base from the fiber holder designed by Graham Hornig (included below), and both cylindrical and spherical lenses used the same "housing". Only clamping plates and lens holding pucks differed between cylindrical and spherical lenses. All deposition jig parts were made out of 6061 aluminum. Deposition parameters for the three film types used are included in the table below.

Material	Gun	Temp (°C)	Power (W)	Off-time (µs)	Freq. (kHz)	Gas flow (sccm) (Ar/O_2)	Dep Pressure[1] (mTorr)	Ramp (s)	Burn-in (s)	Ramp/burn pressure (mTorr)
a-Si	1	150	200	0.5	150	50	3.0	600	60	10
SiO_2	2	150	200	0.8	150	50/3.2	4.0	600	120	10
Ta_2O_5	1	150	200	5	60	40/20	4.0	60	120	7

[1] Circa February 20, 2020, DeCorby group Doug deposition recipes were adjusted to pressures 0.3 mTorr below these stated values to compensate for the relocation of the gas flow inlet in the sputtering chamber.

Fiber holder base

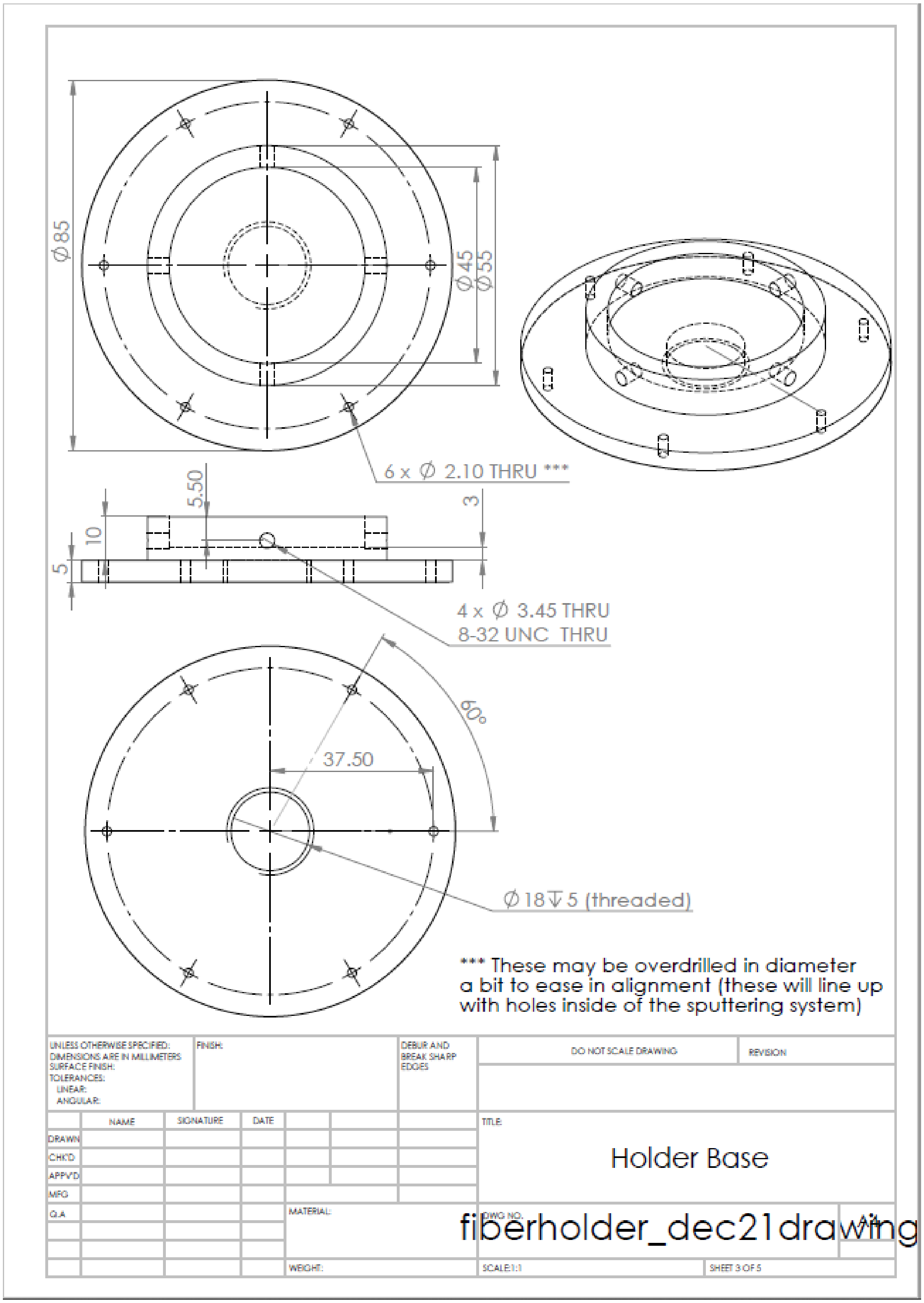

*** These may be overdrilled in diameter a bit to ease in alignment (these will line up with holes inside of the sputtering system)

Hemi-cylindrical deposition jig

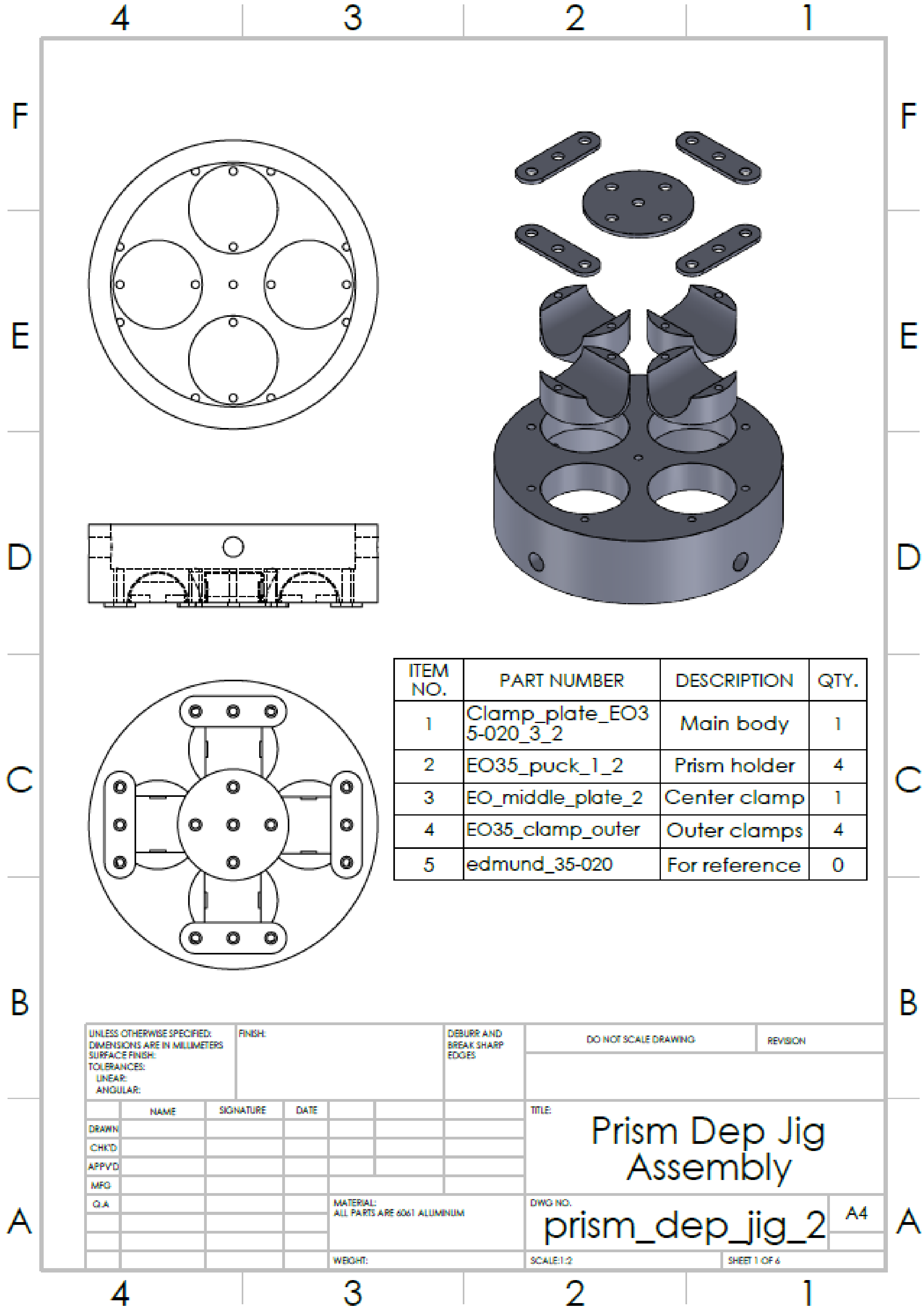

ITEM NO.	PART NUMBER	DESCRIPTION	QTY.
1	Clamp_plate_EO35-020_3_2	Main body	1
2	EO35_puck_1_2	Prism holder	4
3	EO_middle_plate_2	Center clamp	1
4	EO35_clamp_outer	Outer clamps	4
5	edmund_35-020	For reference	0

UNLESS OTHERWISE SPECIFIED:
DIMENSIONS ARE IN MILLIMETERS
SURFACE FINISH:
TOLERANCES:
LINEAR:
ANGULAR:

FINISH:

DEBURR AND
BREAK SHARP
EDGES

DO NOT SCALE DRAWING

REVISION

	NAME	SIGNATURE	DATE
DRAWN			
CHK'D			
APPV'D			
MFG			
Q.A			

TITLE:
Prism Dep Jig
Assembly

MATERIAL:
ALL PARTS ARE 6061 ALUMINUM

DWG NO.
prism_dep_jig_2

A4

WEIGHT:

SCALE:1:2

SHEET 1 OF 6

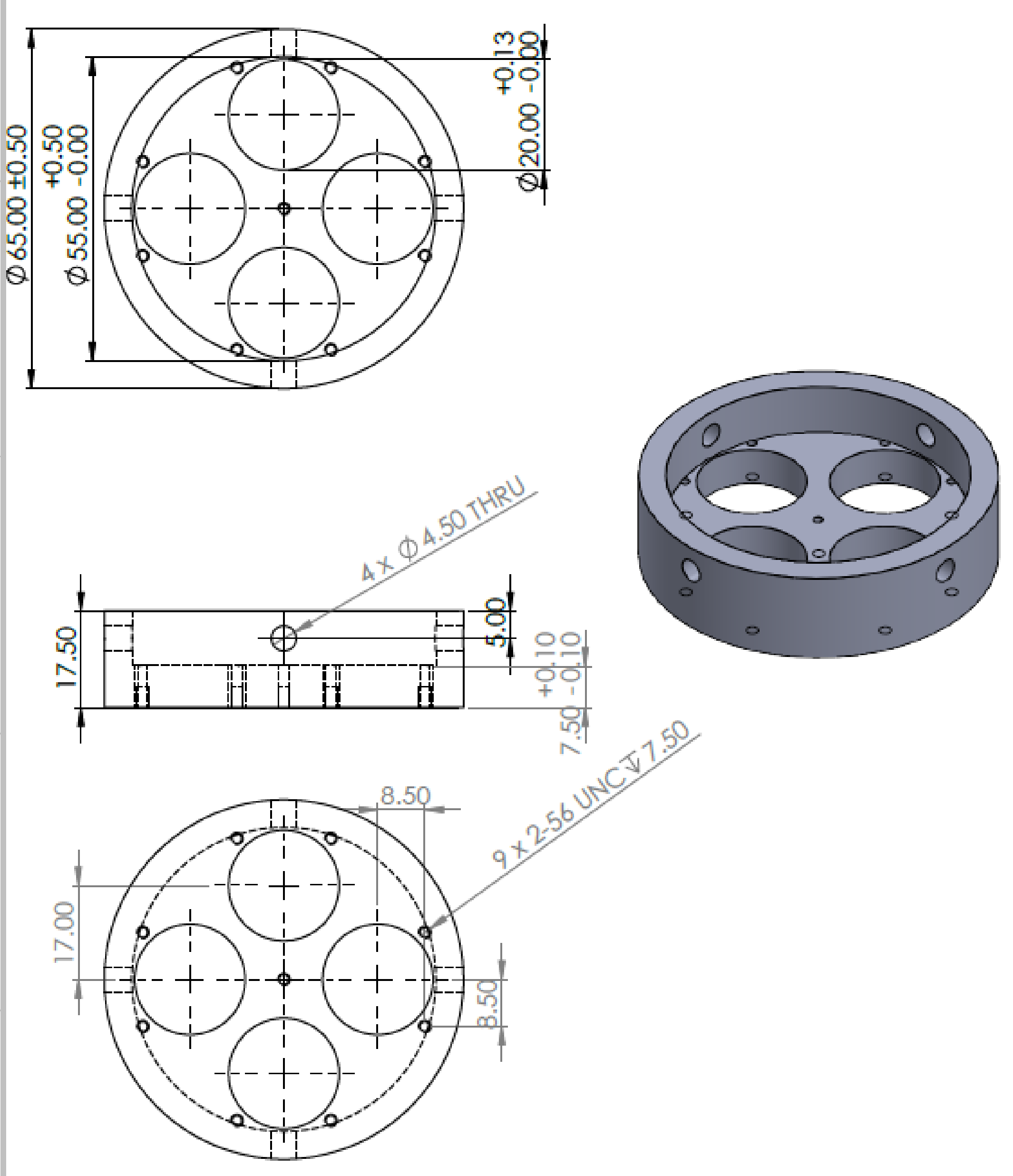

UNLESS OTHERWISE SPECIFIED: DIMENSIONS ARE IN MILLIMETERS SURFACE FINISH: TOLERANCES: LINEAR: ANGULAR:	FINISH:	DEBURR AND BREAK SHARP EDGES	DO NOT SCALE DRAWING	REVISION

	NAME	SIGNATURE	DATE
DRAWN			
CHK'D			
APPV'D			
MFG			
Q.A			

TITLE:
1 - Clamp_plate_EO35-020_3_2

MATERIAL:

DWG NO.
prism_dep_jig_2

A4

WEIGHT:

SCALE:1:2

SHEET 2 OF 6

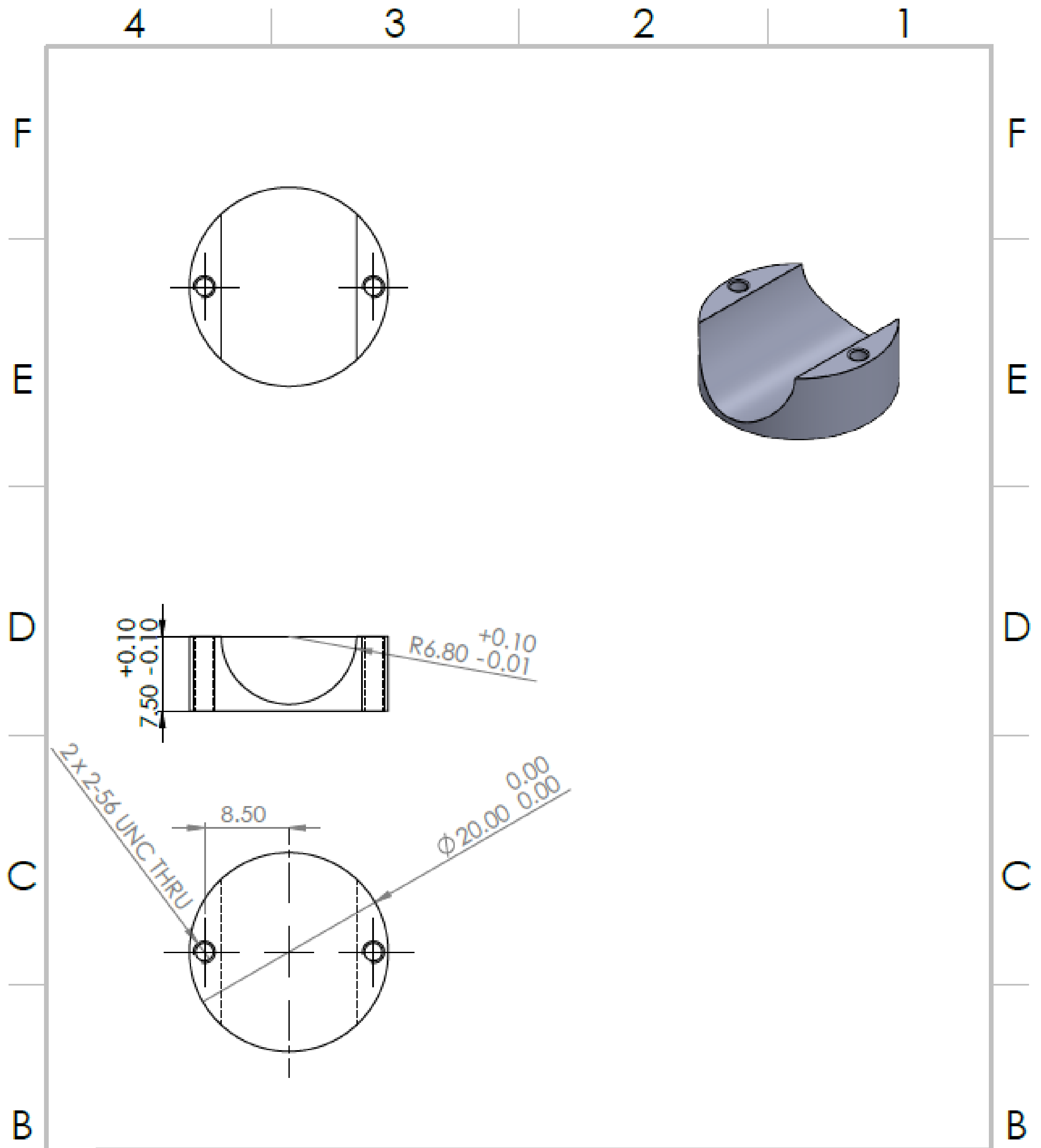

UNLESS OTHERWISE SPECIFIED:
DIMENSIONS ARE IN MILLIMETERS
SURFACE FINISH:
TOLERANCES:
LINEAR:
ANGULAR:

FINISH:

DEBURR AND BREAK SHARP EDGES

DO NOT SCALE DRAWING

REVISION

	NAME	SIGNATURE	DATE
DRAWN			
CHK'D			
APPV'D			
MFG			
Q.A			

MATERIAL:

WEIGHT:

TITLE:

2 - EO_35_puck_1_2

DWG NO.

prism_dep_jig_2

A4

SCALE:2:1

SHEET 3 OF 6

A

4 3 2 1

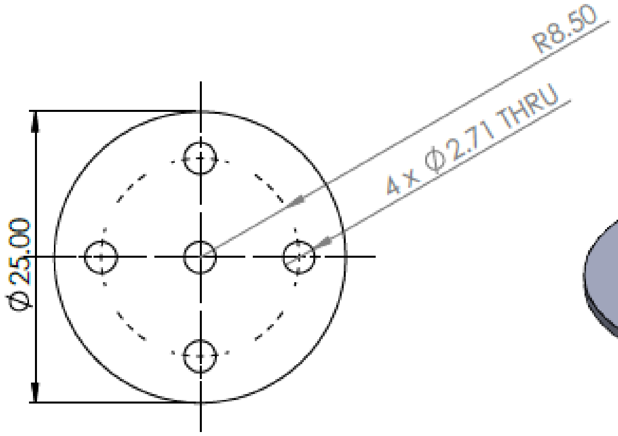

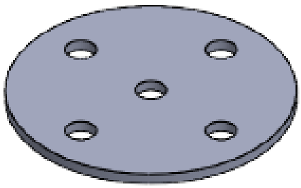

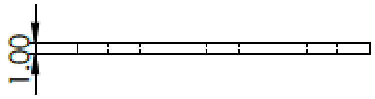

UNLESS OTHERWISE SPECIFIED:
DIMENSIONS ARE IN MILLIMETERS
SURFACE FINISH:
TOLERANCES:
LINEAR:
ANGULAR:

FINISH:

DEBURR AND
BREAK SHARP
EDGES

DO NOT SCALE DRAWING

REVISION

	NAME	SIGNATURE	DATE
DRAWN			
CHK'D			
APPV'D			
MFG			
Q.A			

MATERIAL:

WEIGHT:

TITLE:

3 - EO_middle_plate_2

DWG NO.

prism_dep_jig_2

A4

SCALE:2:1

SHEET 4 OF 6

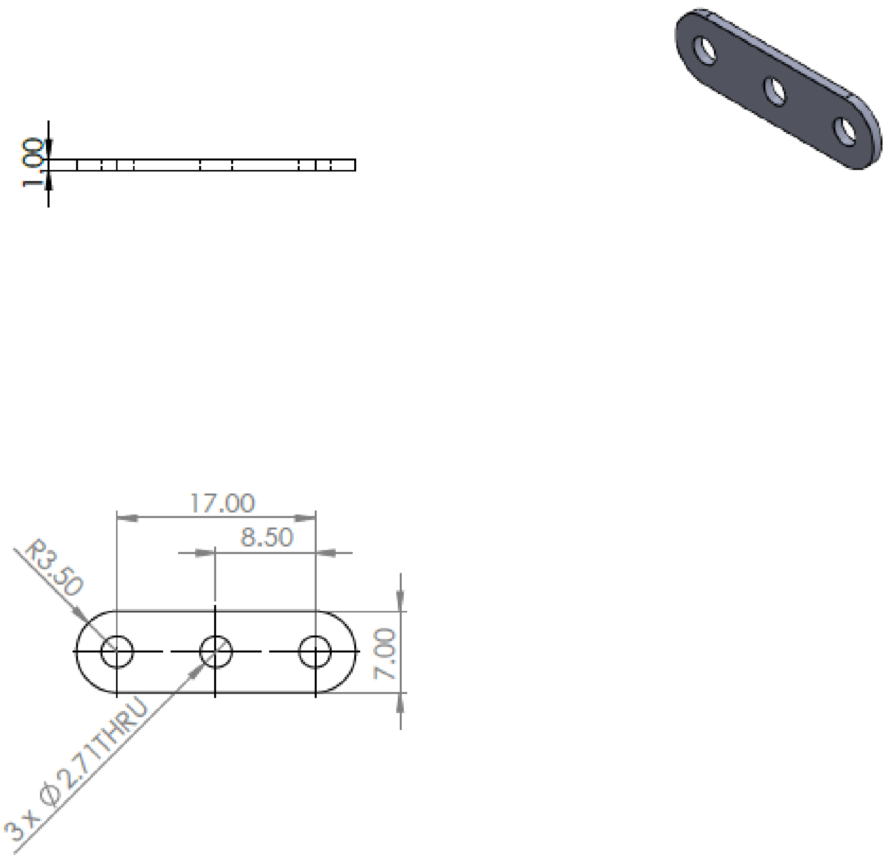

UNLESS OTHERWISE SPECIFIED:
DIMENSIONS ARE IN MILLIMETERS
SURFACE FINISH:
TOLERANCES:
LINEAR:
ANGULAR:

FINISH:

DEBURR AND
BREAK SHARP
EDGES

DO NOT SCALE DRAWING

REVISION

	NAME	SIGNATURE	DATE
DRAWN			
CHK'D			
APPV'D			
MFG			
Q.A			

TITLE:
4 - EO35_clamp_outer

MATERIAL:

DWG NO.
prism_dep_jig_2

A4

WEIGHT:

SCALE:2:1

SHEET 5 OF 6

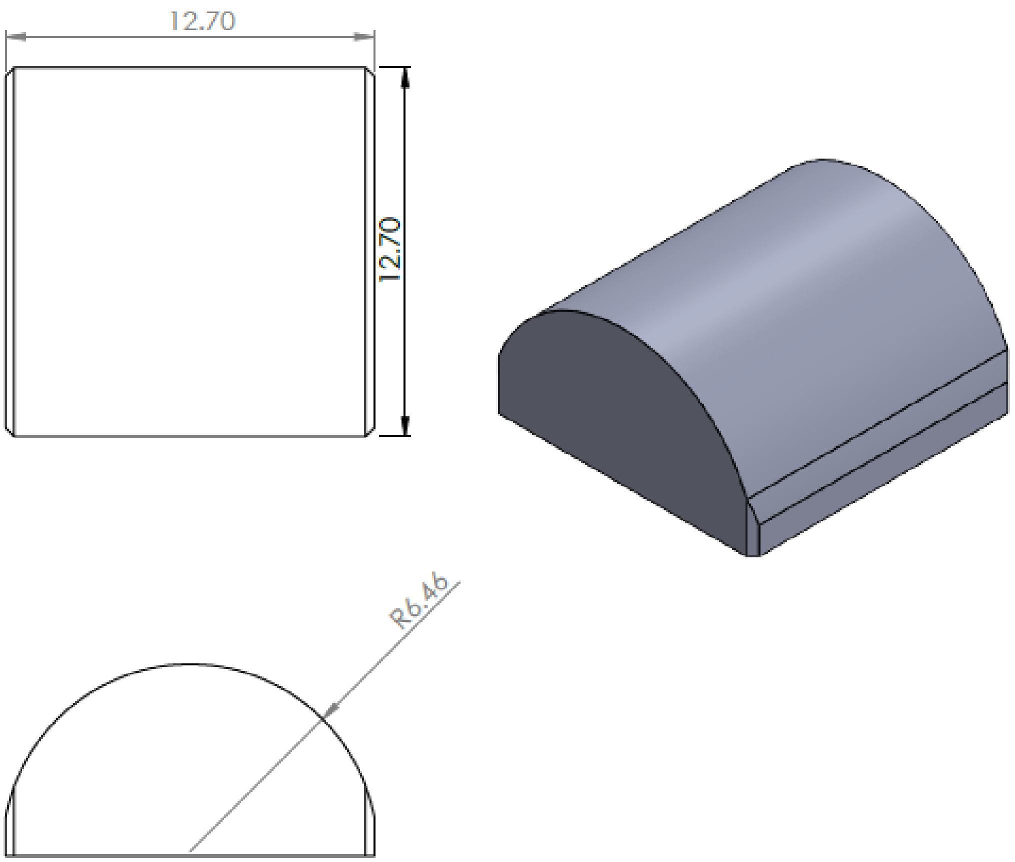

UNLESS OTHERWISE SPECIFIED:
DIMENSIONS ARE IN MILLIMETERS
SURFACE FINISH:
TOLERANCES:
LINEAR:
ANGULAR:

FINISH:

DEBURR AND
BREAK SHARP
EDGES

DO NOT SCALE DRAWING

REVISION

	NAME	SIGNATURE	DATE
DRAWN			
CHK'D			
APPV'D			
MFG			
Q.A			

MATERIAL:

WEIGHT:

TITLE:
5 - edmund_35-
020

DWG NO.
prism_dep_jig_2

A4

SCALE:2:1

SHEET 6 OF 6

Hemi-spherical deposition jig

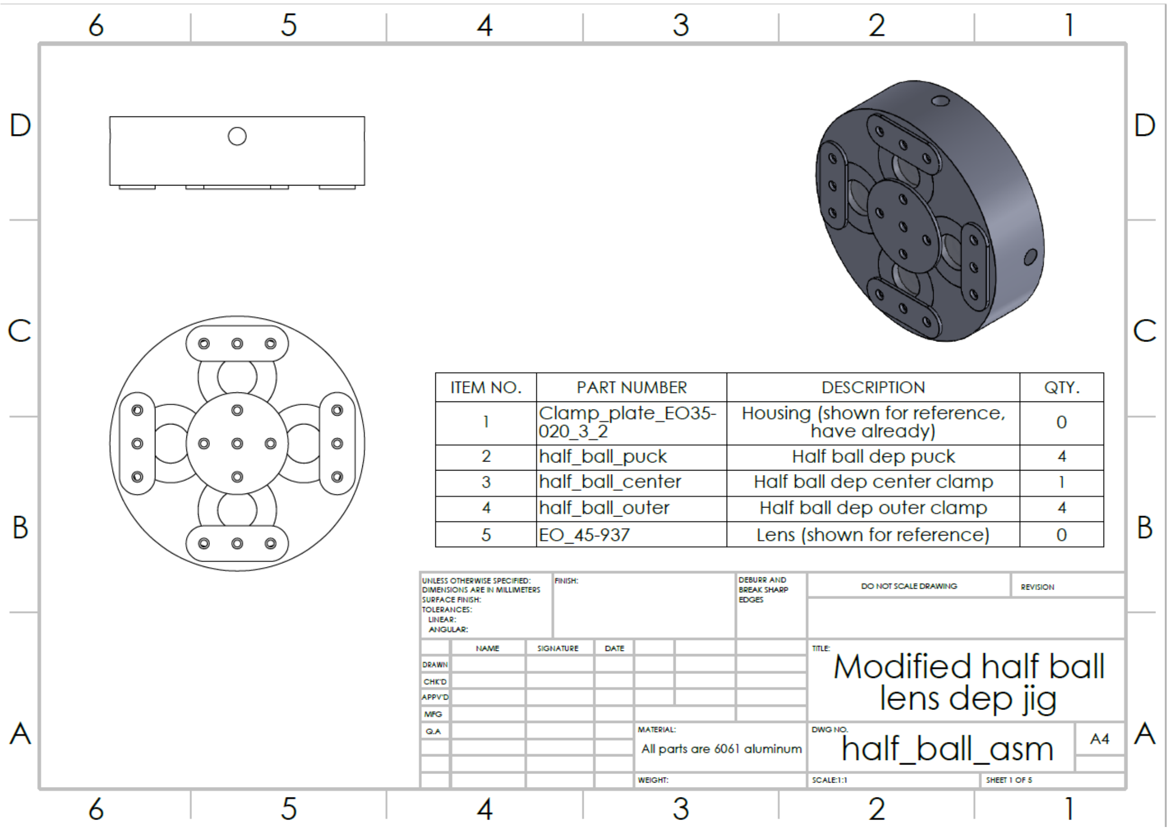

ITEM NO.	PART NUMBER	DESCRIPTION	QTY.
1	Clamp_plate_EO35-020_3_2	Housing (shown for reference, have already)	0
2	half_ball_puck	Half ball dep puck	4
3	half_ball_center	Half ball dep center clamp	1
4	half_ball_outer	Half ball dep outer clamp	4
5	EO_45-937	Lens (shown for reference)	0

UNLESS OTHERWISE SPECIFIED:
DIMENSIONS ARE IN MILLIMETERS
SURFACE FINISH:
TOLERANCES:
LINEAR:
ANGULAR:

FINISH:

DEBURR AND BREAK SHARP EDGES

DO NOT SCALE DRAWING

REVISION

	NAME	SIGNATURE	DATE
DRAWN			
CHK'D			
APPV'D			
MFG			
Q.A			

TITLE: Modified half ball lens dep jig

MATERIAL: All parts are 6061 aluminum

DWG NO. half_ball_asm

A4

WEIGHT:

SCALE:1:1

SHEET 1 OF 5

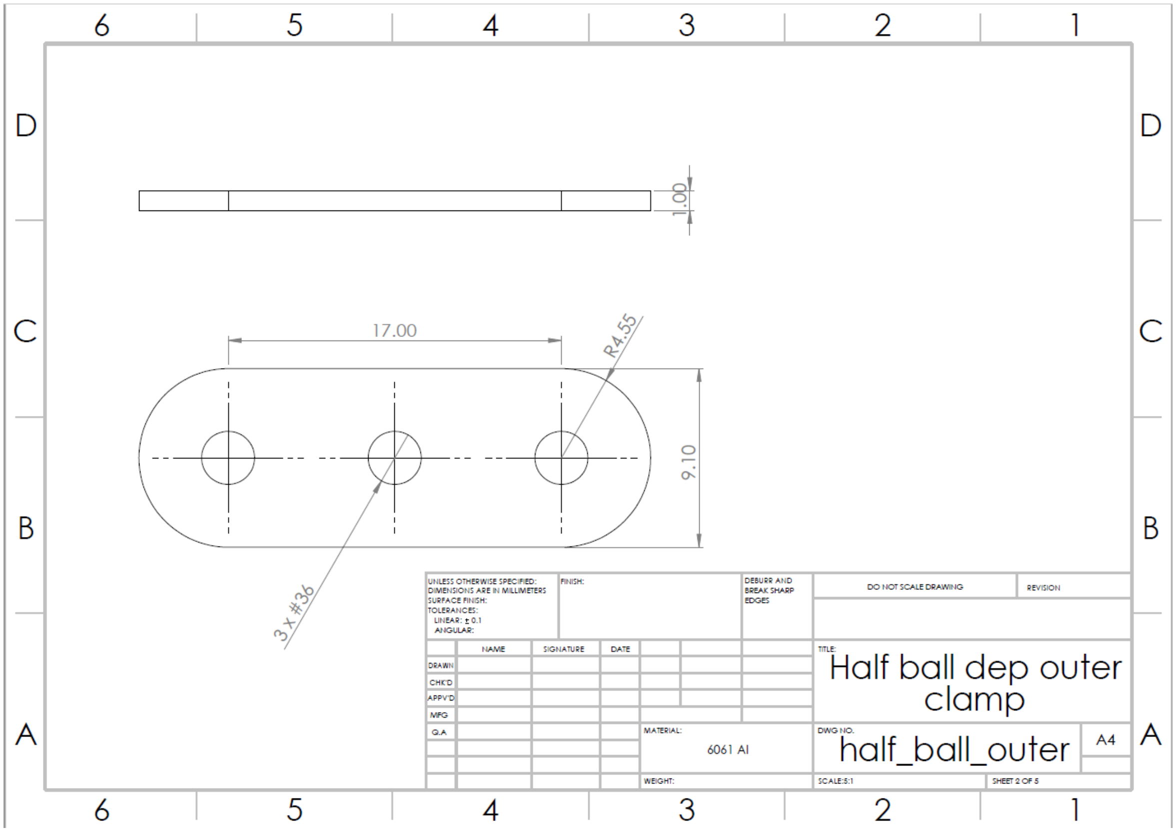

UNLESS OTHERWISE SPECIFIED:
DIMENSIONS ARE IN MILLIMETERS
SURFACE FINISH:
TOLERANCES:
LINEAR: ± 0.1
ANGULAR:

FINISH:

DEBURR AND BREAK SHARP EDGES

DO NOT SCALE DRAWING

REVISION

	NAME	SIGNATURE	DATE
DRAWN			
CHK'D			
APPV'D			
MFG			
Q.A			

TITLE: Half ball dep outer clamp

MATERIAL: 6061 Al

DWG NO. half_ball_outer

A4

WEIGHT:

SCALE:5:1

SHEET 2 OF 5

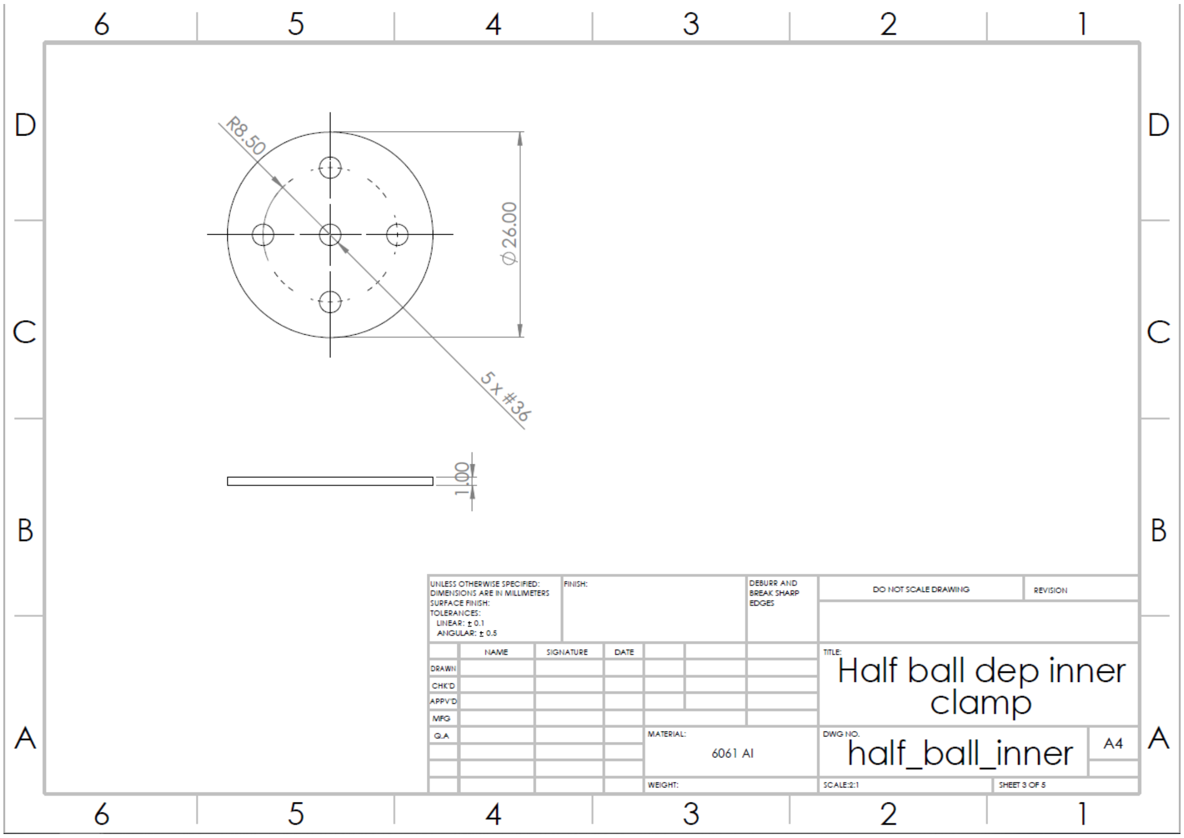
R8.50
Ø26.00
5 x #36
1.00
UNLESS OTHERWISE SPECIFIED:
DIMENSIONS ARE IN MILLIMETERS
SURFACE FINISH:
TOLERANCES:
LINEAR: ± 0.1
ANGULAR: ± 0.5
FINISH:
DEBURR AND BREAK SHARP EDGES
DO NOT SCALE DRAWING
REVISION
NAME
SIGNATURE
DATE
DRAWN
CHK'D
APPV'D
MFG
Q.A
TITLE:
Half ball dep inner clamp
MATERIAL:
6061 Al
DWG NO.
half_ball_inner
A4
WEIGHT:
SCALE:2:1
SHEET 3 OF 5

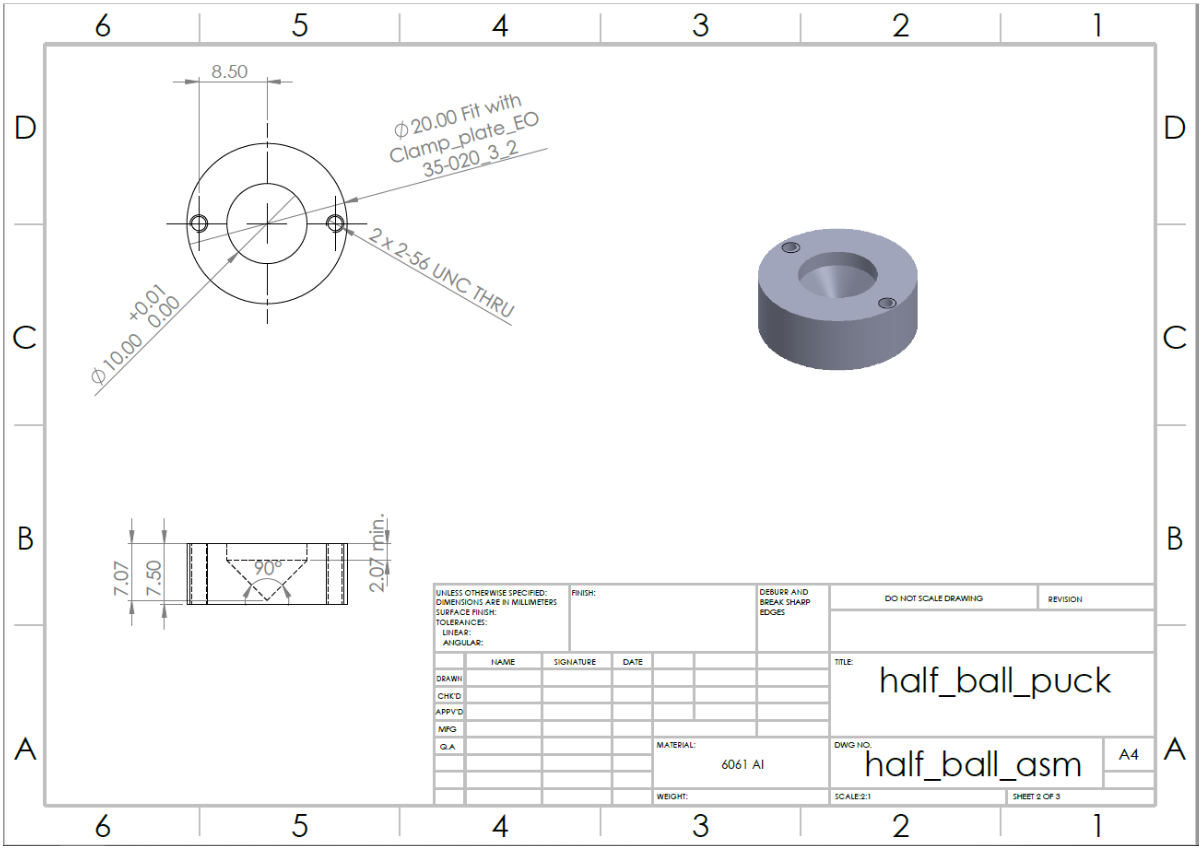
8.50
Ø20.00 Fit with Clamp_plate_EO 35-020_3_2
2 x 2-56 UNC THRU
Ø10.00 +0.01 0.00
7.07
7.50
90°
2.07 min.
UNLESS OTHERWISE SPECIFIED:
DIMENSIONS ARE IN MILLIMETERS
SURFACE FINISH:
TOLERANCES:
LINEAR:
ANGULAR:
FINISH:
DEBURR AND BREAK SHARP EDGES
DO NOT SCALE DRAWING
REVISION
NAME
SIGNATURE
DATE
DRAWN
CHK'D
APPV'D
MFG
Q.A
TITLE:
half_ball_puck
MATERIAL:
6061 Al
DWG NO.
half_ball_asm
A4
WEIGHT:
SCALE:2:1
SHEET 2 OF 3

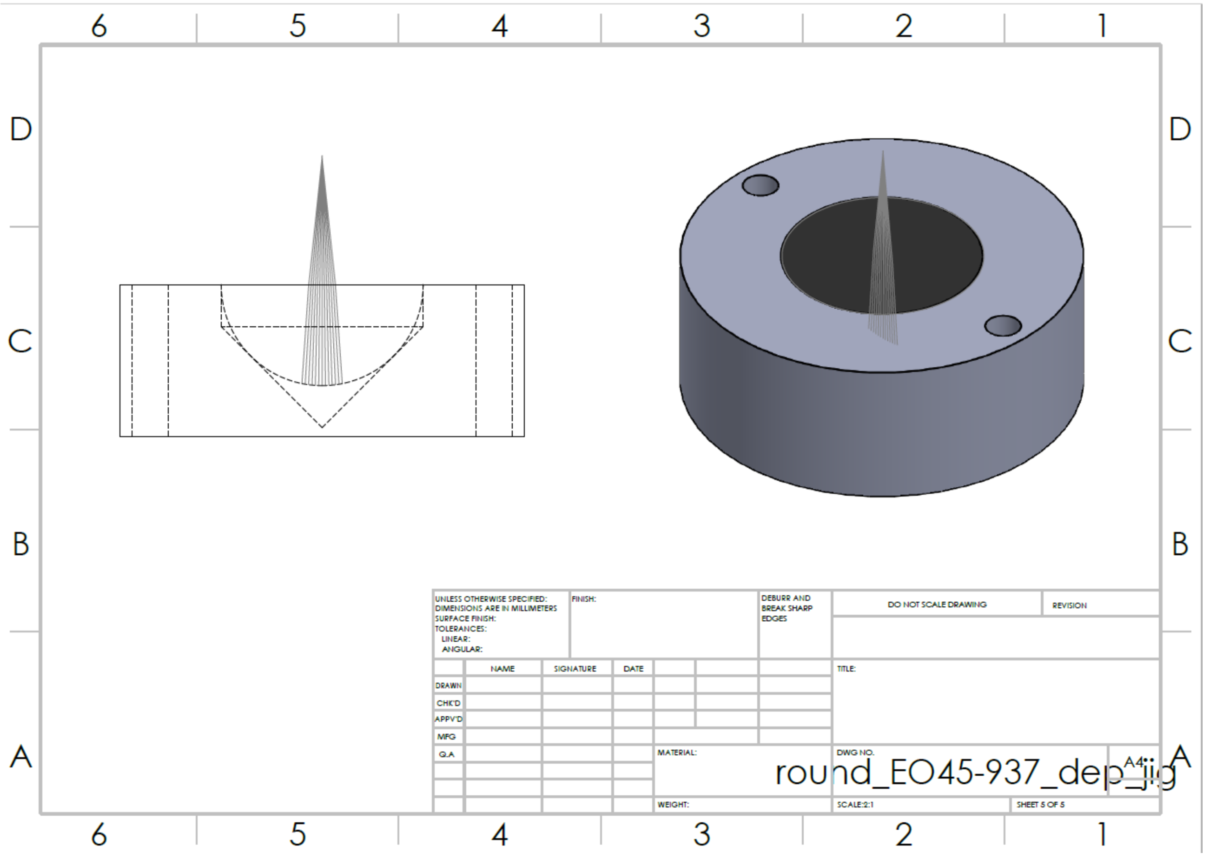
UNLESS OTHERWISE SPECIFIED:
DIMENSIONS ARE IN MILLIMETERS
SURFACE FINISH:
TOLERANCES:
LINEAR:
ANGULAR:
FINISH:
DEBURR AND BREAK SHARP EDGES
DO NOT SCALE DRAWING
REVISION
NAME
SIGNATURE
DATE
DRAWN
CHK'D
APPV'D
MFG
Q.A
TITLE:
MATERIAL:
DWG NO.
round_EO45-937_dep_jig
A4
WEIGHT:
SCALE:2:1
SHEET 5 OF 5

Appendix B: Assembly jig drawings

All lenses were cleaned with isopropanol and water, and then dried prior to assembly. In all cases, prior to being clamped together, assembly was performed in the class-10 cleanroom in the nanoFAB. Hemi-cylindrical lenses were clamped in place using adjustable clamps and then the piezoelectric stacks were glued in place with Norland Optical Adhesive NOA-68T, which was cured using a UV curing lamp. For the hemi-spherical lenses, a custom jig was machined according to the drawings included below. The spherical lens halves were loaded into the appropriate holders, which were held in proper registration using dowel pins. The two holders were then clamped together, and the piezo stacks affixed again using NOA-68 and cured. At that point, the assembly was removed from the clamps and the lenses were glued (and cured) to the lens holders using NOA-68T. Only after all curing was complete were the dowel pins removed. Best results were obtained when two dowel pins, in opposite corners, were used for registration. Originally, all parts were machined in 6061 aluminum. However, after some assemblies had minimum resting air gaps greater than 3 μm, the lens holders A & B were machined in 316 stainless steel for improved rigidity.

Also included below are drawings for the stand and baseplate necessary to hold these lenses on rotational stages ELL8 and CR1 from Thorlabs.

Spherical lens assembly jig

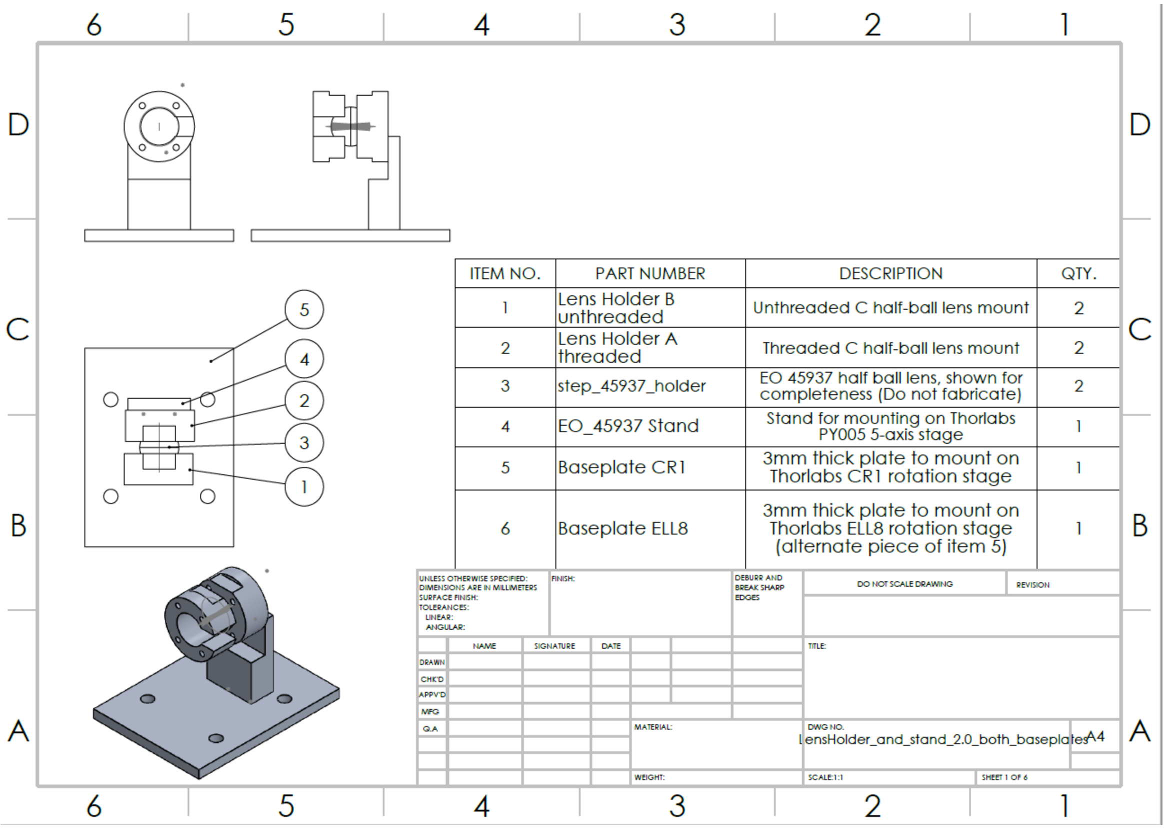

ITEM NO.	PART NUMBER	DESCRIPTION	QTY.
1	Lens Holder B unthreaded	Unthreaded C half-ball lens mount	2
2	Lens Holder A threaded	Threaded C half-ball lens mount	2
3	step_45937_holder	EO 45937 half ball lens, shown for completeness (Do not fabricate)	2
4	EO_45937 Stand	Stand for mounting on Thorlabs PY005 5-axis stage	1
5	Baseplate CR1	3mm thick plate to mount on Thorlabs CR1 rotation stage	1
6	Baseplate ELL8	3mm thick plate to mount on Thorlabs ELL8 rotation stage (alternate piece of item 5)	1

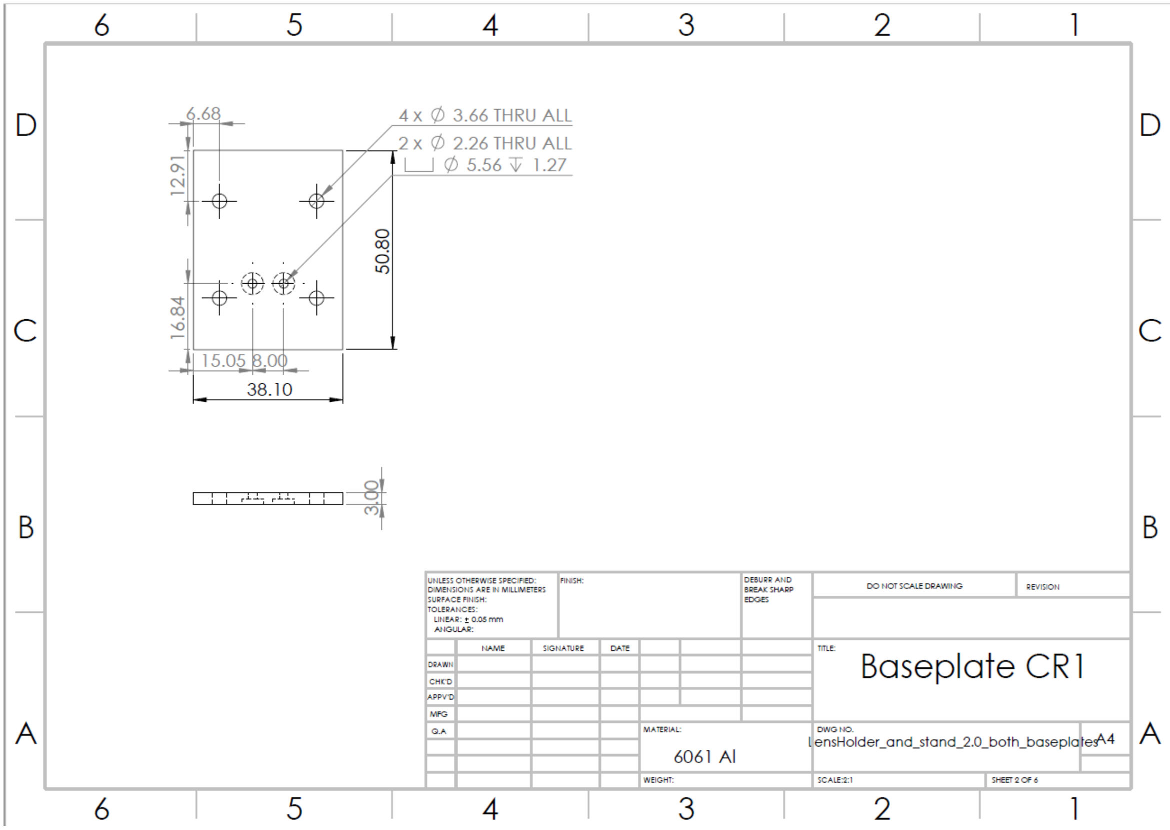

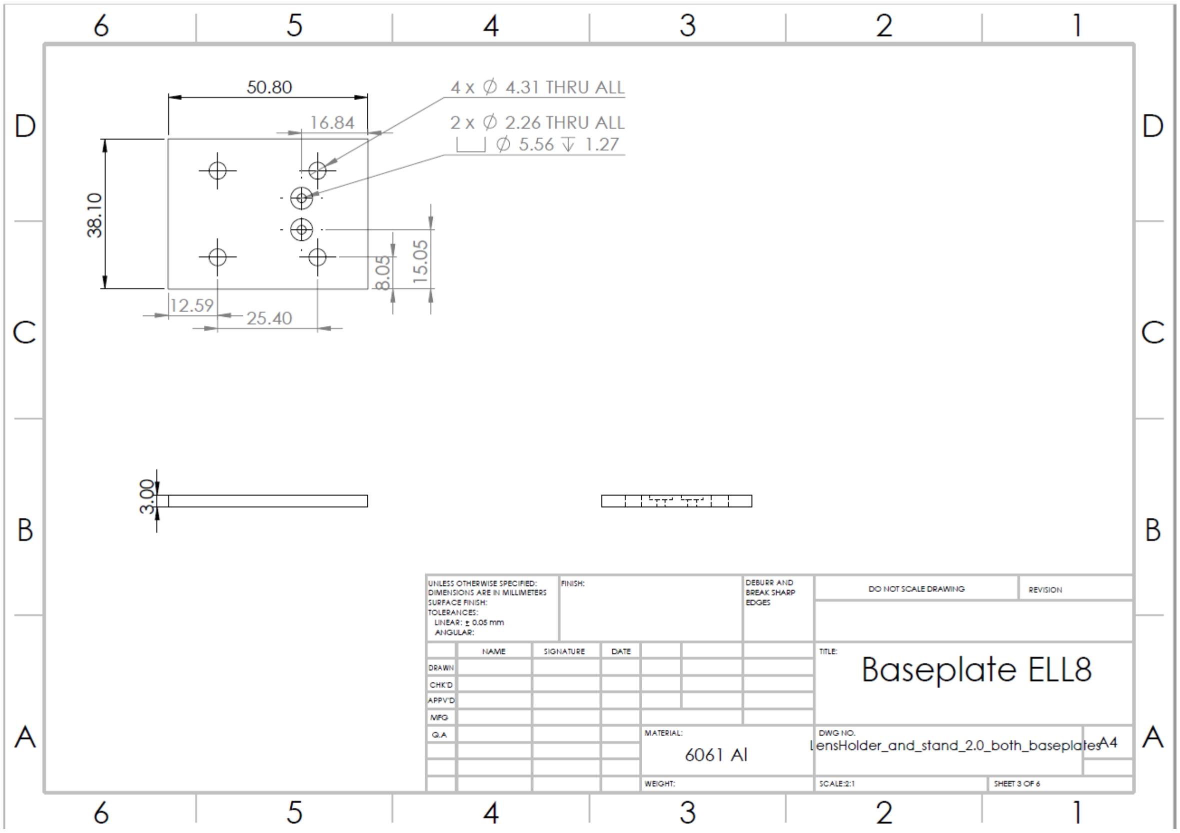

6
5
4
3
2
1
D
C
B
A
50.80
16.84
4 x ∅ 4.31 THRU ALL
2 x ∅ 2.26 THRU ALL
⌴ ∅ 5.56 ↧ 1.27
38.10
8.05
15.05
12.59
25.40
3.00
UNLESS OTHERWISE SPECIFIED:
DIMENSIONS ARE IN MILLIMETERS
SURFACE FINISH:
TOLERANCES:
LINEAR: ± 0.05 mm
ANGULAR:
FINISH:
DEBURR AND BREAK SHARP EDGES
DO NOT SCALE DRAWING
REVISION
NAME
SIGNATURE
DATE
DRAWN
CHK'D
APPV'D
MFG
Q.A
TITLE:
Baseplate ELL8
MATERIAL:
6061 Al
DWG NO.
LensHolder_and_stand_2.0_both_baseplates
A4
WEIGHT:
SCALE:2:1
SHEET 3 OF 6

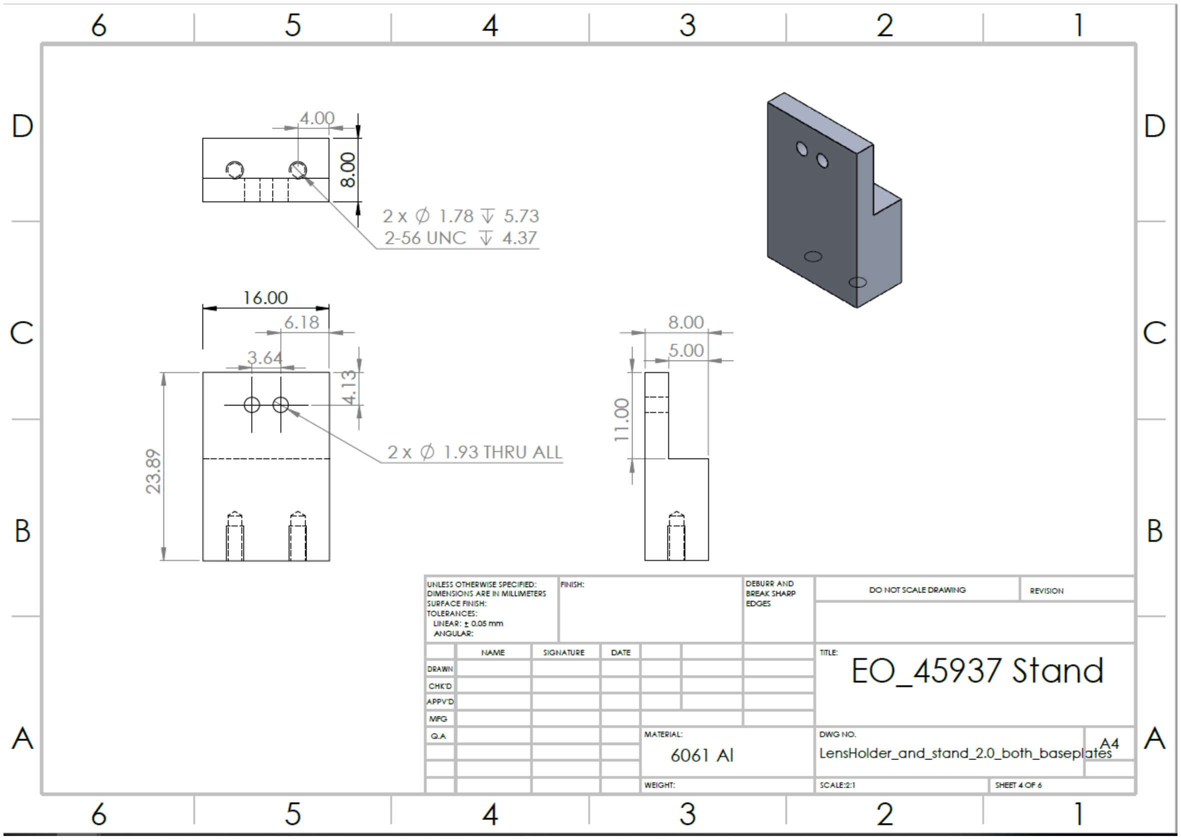

6
5
4
3
2
1
D
C
B
A
4.00
8.00
2 x ∅ 1.78 ↧ 5.73
2-56 UNC ↧ 4.37
16.00
6.18
3.64
4.13
23.89
2 x ∅ 1.93 THRU ALL
8.00
5.00
11.00
UNLESS OTHERWISE SPECIFIED:
DIMENSIONS ARE IN MILLIMETERS
SURFACE FINISH:
TOLERANCES:
LINEAR: ± 0.05 mm
ANGULAR:
FINISH:
DEBURR AND BREAK SHARP EDGES
DO NOT SCALE DRAWING
REVISION
NAME
SIGNATURE
DATE
DRAWN
CHK'D
APPV'D
MFG
Q.A
TITLE:
EO_45937 Stand
MATERIAL:
6061 Al
DWG NO.
LensHolder_and_stand_2.0_both_baseplates
A4
WEIGHT:
SCALE:2:1
SHEET 4 OF 6

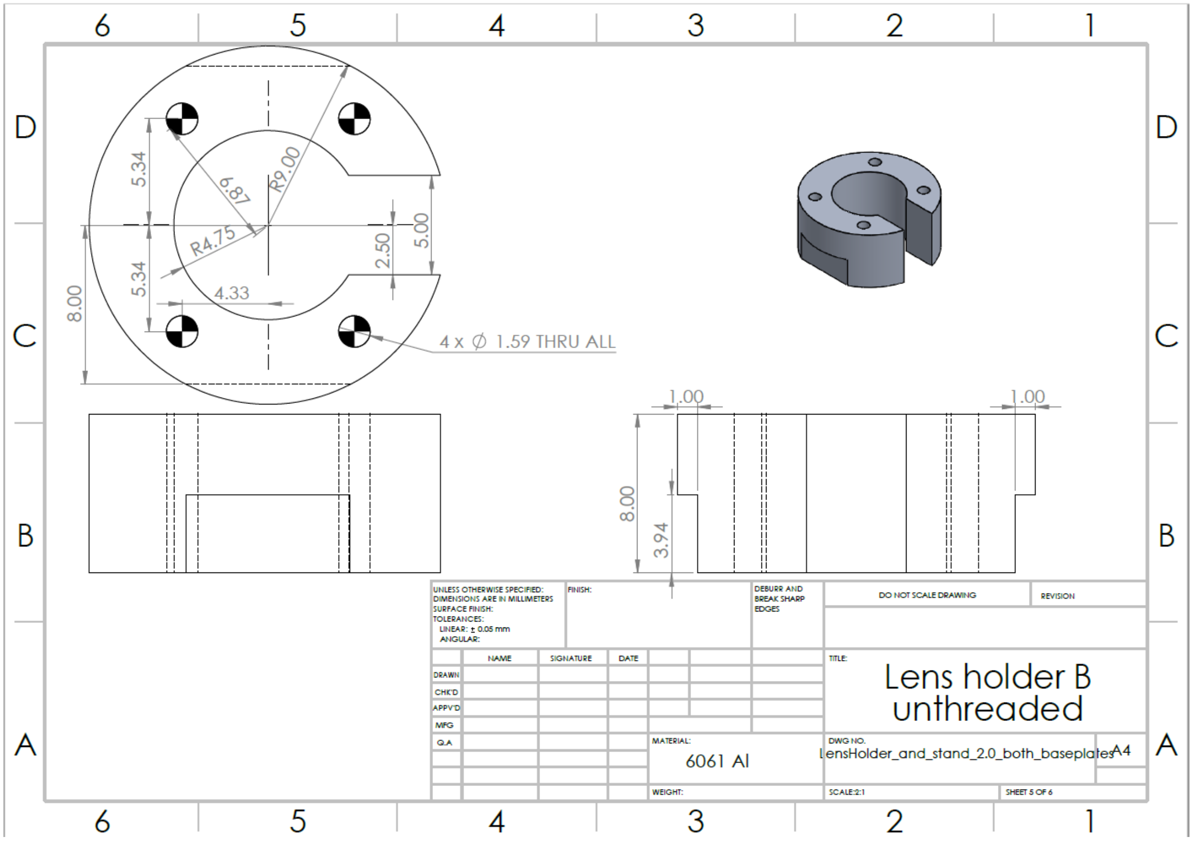
6
5
4
3
2
1
D
C
B
A
5.34
6.87
R9.00
R4.75
2.50
5.00
5.34
8.00
4.33
4 x ∅ 1.59 THRU ALL
1.00
1.00
8.00
3.94
UNLESS OTHERWISE SPECIFIED:
DIMENSIONS ARE IN MILLIMETERS
SURFACE FINISH:
TOLERANCES:
LINEAR: ± 0.05 mm
ANGULAR:
FINISH:
DEBURR AND BREAK SHARP EDGES
DO NOT SCALE DRAWING
REVISION
NAME
SIGNATURE
DATE
DRAWN
CHK'D
APPV'D
MFG
Q.A
TITLE:
Lens holder B unthreaded
MATERIAL:
6061 Al
DWG NO.
LensHolder_and_stand_2.0_both_baseplates
A4
WEIGHT:
SCALE:2:1
SHEET 5 OF 6

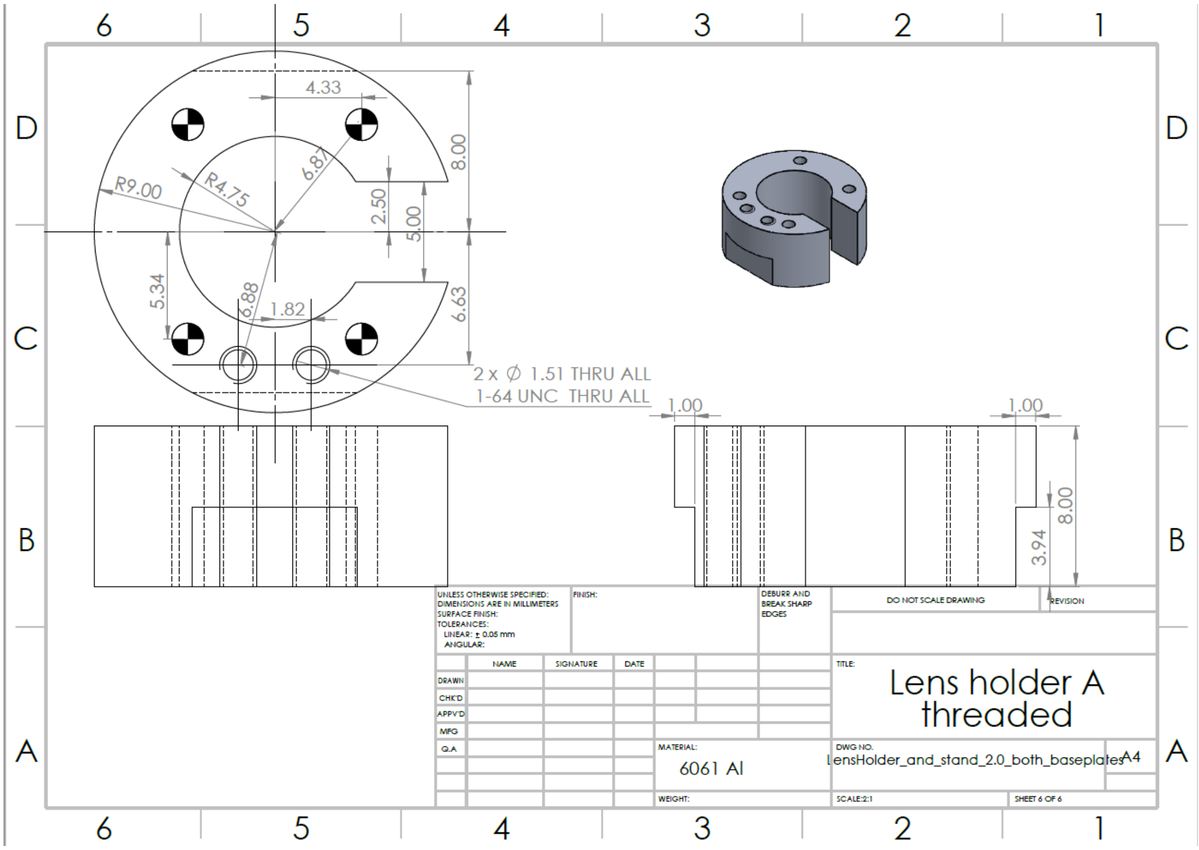
6
5
4
3
2
1
D
C
B
A
4.33
8.00
R9.00
R4.75
6.87
2.50
5.00
5.34
6.88
1.82
6.63
2 x ∅ 1.51 THRU ALL
1-64 UNC THRU ALL
1.00
1.00
8.00
3.94
UNLESS OTHERWISE SPECIFIED:
DIMENSIONS ARE IN MILLIMETERS
SURFACE FINISH:
TOLERANCES:
LINEAR: ± 0.05 mm
ANGULAR:
FINISH:
DEBURR AND BREAK SHARP EDGES
DO NOT SCALE DRAWING
REVISION
NAME
SIGNATURE
DATE
DRAWN
CHK'D
APPV'D
MFG
Q.A
TITLE:
Lens holder A threaded
MATERIAL:
6061 Al
DWG NO.
LensHolder_and_stand_2.0_both_baseplates
A4
WEIGHT:
SCALE:2:1
SHEET 6 OF 6

Appendix C: Imaging system and alignment

The hyperspectral imaging system produced in the course of Chapter 4 consisted of five main elements:

- Fiber U-bench (Thorlabs CBB1).
- 0.5” diameter, 19 mm focal length achromat lenses (Thorlabs AC127-019-C and AC127-019-A for NIR and VIS filters respectively).
- Infinity corrected 5x objective Epiplan 5x/0.13 W0.8" (Zeiss 442020-9902-000).
- 25 mm focal length TV-lens adjustable for object distances from 0.4 m to ∞ .
- Consumer grade color or monochrome USB cameras (Thorlabs DCC 1645-C or 1545-M respectively) mounted on a linear translational stage with the axis perpendicular to the optical axis.

The objective was mounted in a 30 mm cage plate (Thorlabs CP33) using an RMS – SM1 thread adapter (Thorlabs SM1A3), then mounted to the fiber U-bench at a distance ~ 1.5 cm from the input achromat. The achromat lenses were held in SM1 threading adapters (Thorlabs SM1A6T) and screwed into the SM1 threads on the U-bench. Retaining rings were not used to hold the SM1A6T adapters in the U-bench such that position adjustment could be done using the SM1 thread. The fiber U-bench was held horizontally relative to the table using a custom machined mount designed by Chenxi Huang (included below). The spherical-lens filter was then held on a custom machined mount (detailed in Appendix B) on a continuous rotational stage (Thorlabs CR1), oriented horizontally relative to the table. Finally, an adjustable aperture was placed between the objective and the input achromat, with the best results obtained with an ~ 3 mm diameter aperture.

Alignment

Alignment of the elements within the optical system was best performed in the following order:

1. Use a 1951 USAF resolution test target illuminated by a gooseneck fiber-coupled microscope illuminator.
2. Set the objective to object distance to the Zeiss specified working distance.
3. Mount the two achromat lenses in the U-bench. Ensure that the first achromat is mounted such that the full ~ 60 mm achromat to achromat distance can be accessed by the second achromat without the threaded adapter reaching the end of the internal U-bench thread.

Approximately 3-5 mm of threading adapter should be visible on the interior of the U-bench for both input and output achromats.

4. Visually center the spherical filter on the optical axis.
5. Adjust the input achromat to spherical filter spacing to the Zemax simulated spacing (~25 mm) by translating the filter along the optical axis. Use a caliper to measure the appropriate distance. Then do not touch the filter position or input achromat position along the optical axis.
6. Rotate the spherical filter such that the optical axis is at normal incidence to the air gap.
7. Mount the camera with TV-lens attached (ensure the silver CS-mount to C-mount adapter ring is used to hold the TV-lens) as close as possible to the output of the U-bench.
8. Use a caliper to attempt to align the TV-lens axis parallel to the optical (i.e. ensure the lens to U-bench distance is constant along the circumference of the lens).
9. Center the camera on the optical axis using the linear translation stage.
10. Using one tooth of an adjustable spanner wrench, adjust the output achromat to spherical filter spacing to bring the object into focus.
11. The system magnification should be F_{TV} / F_{OBJ} (~0.75 for the 5x objective, F_{OBJ} = 33 mm, F_{TV} = 25 mm). If this is not so, adjust the input achromat to spherical lens spacing (using the output achromat to focus the image), until the prescribed magnification is reached.
12. If excessive coma is noted, the TV-lens may not be oriented parallel to the optical axis, or the TV-lens may not be centered on the optical axis, or the filter may not be centered along the optical axis. Adjust these three parameters as necessary to reduce aberration.
13. Once aberrations have been reduced, switch to the desired target.
14. Focus on the target using the object to objective spacing.

Imaging setup photos

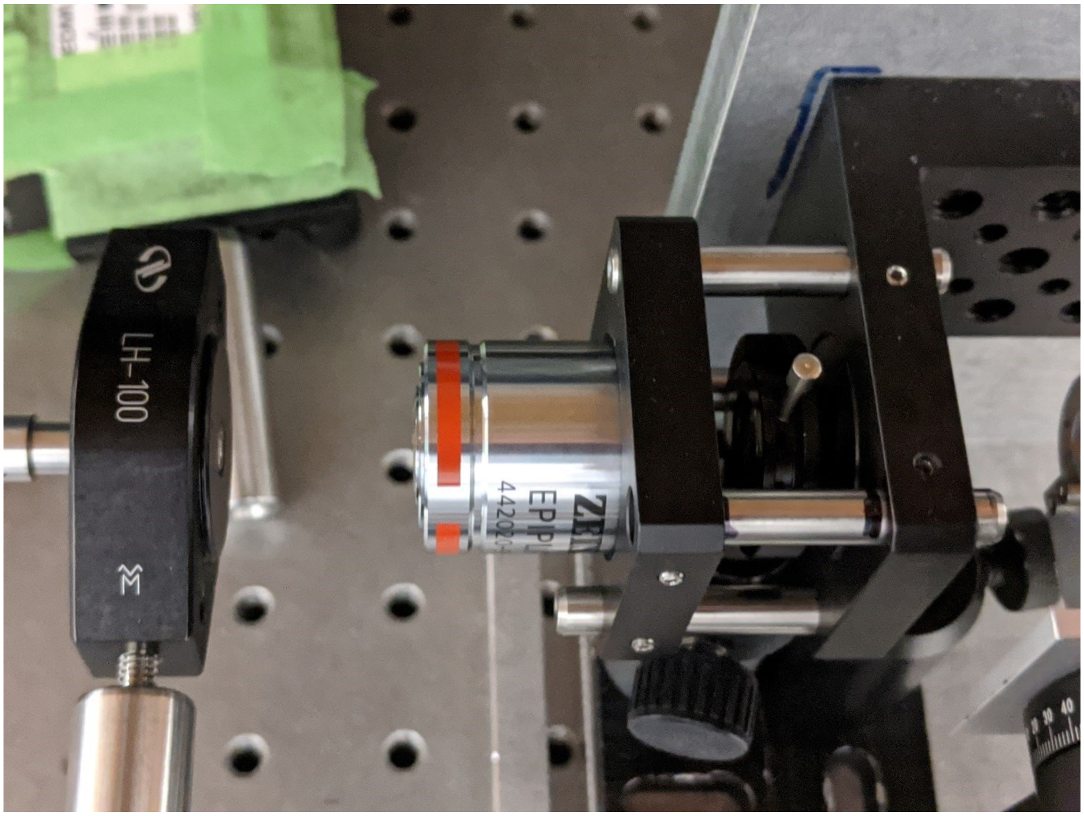

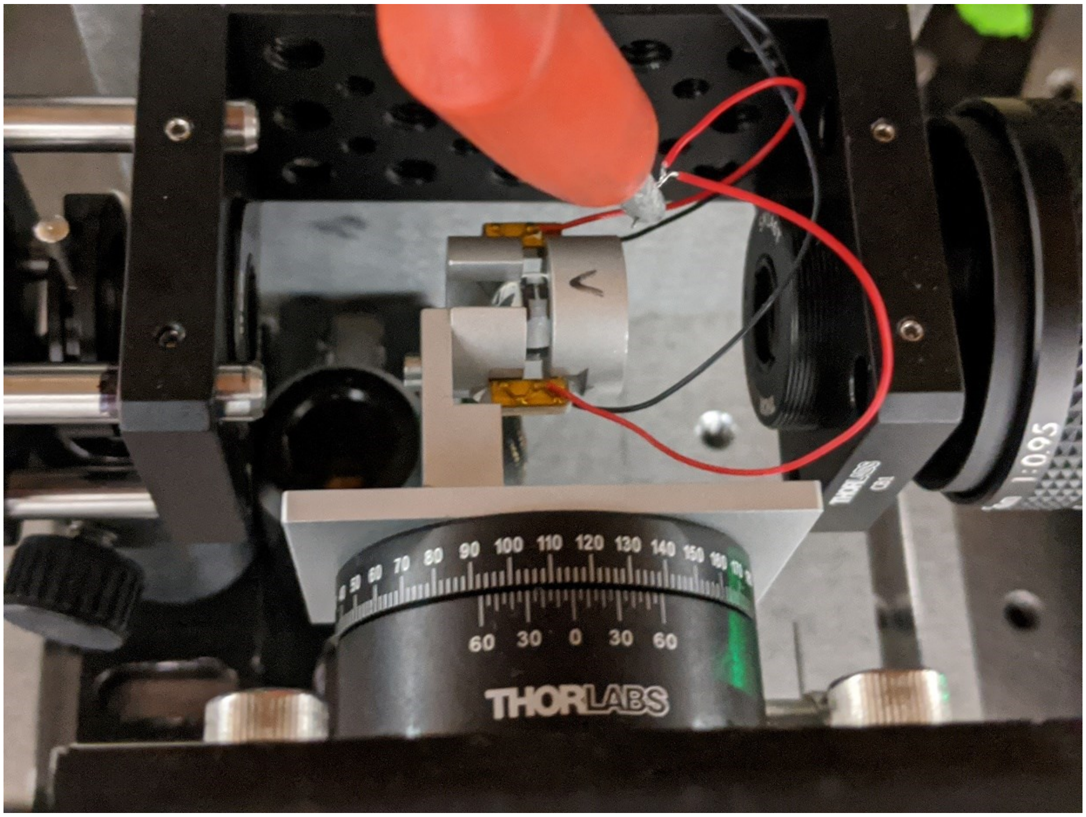

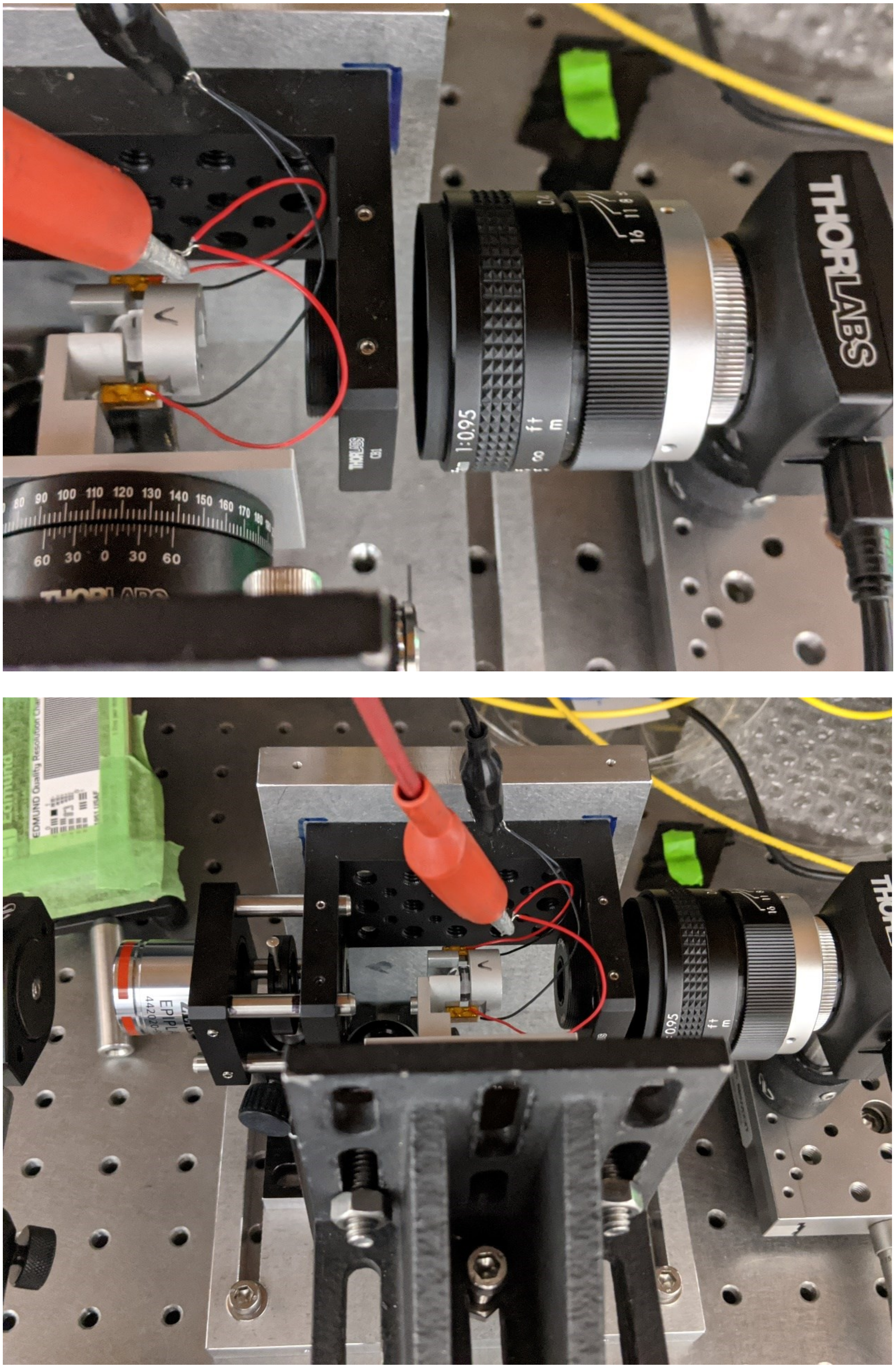

U-Bench shelf